



Universidad
del País Vasco

Euskal Herriko
Unibertsitatea

Thermal and optical characterization
of heterogeneous materials
by Infrared Lock-in Thermography

by

Raquel Fuente Dacal

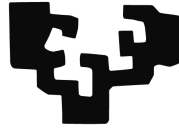
Thesis presented in partial fulfilment of the requirements for the degree of

Doctor of Philosophy

at the Department of Applied Physics I, Faculty of Engineering, UPV/EHU

Bilbao, May 2012

eman ta zabal zazu



Universidad
del País Vasco

Euskal Herriko
Unibertsitatea

Thermal and optical characterization
of heterogeneous materials
by Infrared Lock-in Thermography

by

Raquel Fuente Dacal

Supervisors: Agustín Salazar Hernández and María Aránzazu Mendioroz Astigarraga

Thesis presented in partial fulfilment of the requirements for the degree of

Doctor of Philosophy

at the Department of Applied Physics I, Faculty of Engineering, UPV/EHU

Bilbao, May 2012

Acknowledgements

Me gustaría expresar mi más sincero agradecimiento a toda la gente que de un modo u otro ha contribuido a llevar a cabo este proyecto.

A mis directores, Prof. Agustín Salazar y Prof. Arantza Mendioroz, les debo gran parte de lo que he aprendido. Su esfuerzo, dedicación y paciencia han supuesto siempre un empujoncito hacia delante, muchas gracias.

Además, agradezco al Ministerio de Economía y Competitividad la beca predoctoral FPI concedida sin la cual esta tesis no hubiera sido posible.

I would also like to express my gratitude to Prof. Christ Glorieux for giving me the opportunity to work in his group in Leuven and moreover his kindness to me. I am also very thankful to Chandra, Bert and Xiong for all the help in the lab. And of course to Pati, Cinzia and all the girls and guys for giving me the chance to share this experience with them. All in all, it was a really pleasant stay.

No me gustaría olvidarme de toda la gente del departamento. De Esti, que siempre ha estado ahí, tanto para iniciar medidas a las siete de la mañana, como para tender una mano cuando se necesitaba; de Sara, con quien más horas al día he debido pasar frente a frente en estos cuatro años, trabajando, y hablando, todo hay que decirlo...;

de Naiara, Itziar, Adrián, Santi, Ricardo, Imanol... por todos los cafés-malos de máquina compartidos... Gracias a todos!

Y cómo dejarme a las compis de la uni, con los domingos de chocochurros o helados rajando de tesis, y de lo que no son tesis... :-)

Y las de la cuadri, que se enfadan si no les pongo! Aún así, os recompensaré con algo más... promise!

Y bueno, last but not least, a la familia, sanguínea y no sanguínea, el mayor de mis agradecimientos, por todos los detalles que pasan desapercibidos, desde la útil colaboración gráfica hasta la preparación del tupper de todos los días, preocupados porque vaya a desfallecer yo por cualquier esquina... Gracias por ayudarme a recorrer este camino, que aunque no se sabe dónde va, como le decía el Gato de Cheshire a Alicia: *Siempre llegarás a alguna parte, si caminas lo bastante.*

Index

Index	V
1. Introduction	1
2. Theoretical background	7
2.1. Thermal emission	7
2.2. Heat conduction.....	13
2.3. Thermal diffusivity measurements	14
2.3.1. Semiinfinite sample	15
A. Plane illumination.....	15
B. Focused illumination.....	17
2.3.2. Sheet	22
A. Plane illumination.....	23
B. Focused illumination.....	25
2.4. Heat losses	28
2.4.1. Semiinfinite sample	30
2.4.2. Sheet	32
A. Plane illumination.....	33
B. Focused illumination.....	34
2.5. Thermal quadrupole method.....	36

3. Thin films and filaments thermal diffusivity measurements	43
3.1. Introduction.....	43
3.2. Theoretical model	45
3.2.1. Films	45
A. Isotropic film.....	45
<i>i) Thermally thin film.....</i>	<i>47</i>
<i>ii) Thermally thick film.....</i>	<i>49</i>
B. Anisotropic film.....	50
<i>i) Thermally thin film.....</i>	<i>51</i>
<i>ii) Thermally thick film.....</i>	<i>52</i>
3.2.2. Filaments.....	53
A. Monofilament.....	53
B. Two-layer filament.....	60
3.3. Experimental setup.....	62
3.4. Results and discussion	70
4. Semitransparent samples: thermal diffusivity and optical absorption coefficient simultaneous measurements	81
4.1. Introduction.....	81
4.2. Theoretical model	83
4.2.1. Homogeneous solids	83
4.2.2. Multilayered solids.....	88
4.2.3. Effects to consider.....	93
A. Heat losses	93
B. Multiple reflections of the incident light	97
C. Transparency to the infrared radiation	98
D. Lateral heat diffusion	101
4.3. Experimental setup.....	102
4.4. Results and discussion	105
4.4.1. Homogeneous solids	106
4.4.2. Multilayered solids.....	112
5. Conclusions.....	117

List of publications 121

Resumen 125

References 131

1. Introduction

No need to remind the importance of heat over history, temperature measurement has also been a great concern. Being Galileo in 1593 the first one to attempt the design of today's thermometer, it seems unlikely that the physics behind temperature was understood in those days. Neither Newton with his glass prism experiment, first one introducing the term *spectrum*, got to notice the heat beyond the red. It was not until 1800 when Herschel repeated the famous prism experiment to study the heat effects associated with different spectral ranges of the radiation from the Sun. By placing mercury thermometers along the spectrum after the prism, he unexpectedly realized that the readings of the thermometers located beyond the red end of the spectrum were higher than those of the thermometers located within the visible range. He concluded that the spectrum was wider than the visible range, and named the new discovery *invisible rays*, which were later known as *infrared rays*. Nevertheless, it was Max Planck a century later, in 1900, who quantitatively explained Herschel's experiment and described the laws of thermal radiation.

The development of thermal radiation and infrared technologies took off around World War II, due to the numerous applications on military and aeronautic fields. However, it soon passed to the civil market. Thanks to the advances in infrared detectors and semiconductors in the 50's and 60's, and what is more, the CCD in the 70's, which promoted the development of the IRFPA (*Infrared Focal Plane Array*), a

variety of technologies have emerged on the Thermography field, such as Non Destructive Testig (NDT) or characterization of thermal and optical properties of materials.

Thermography (thermal imaging) does not actually measure temperature, as it is popularly believed, but it detects radiation in the infrared range, which is indeed related to the sample temperature, but also to the surface nature. One of its main advantages is that it is a non-contact technique, what allows to measure under hostile environments, such as high pressure or temperature.[1, 2]

In addition to this, Infrared Thermography (IRT) can be passive or active. Passive stands for the simple recording of the emitted infrared radiation, without previous excitation of the object to measure. For simplicity reasons, it was the first to arise, with applications in the military field (night vision), civil engineering (building maintenance) or medicine (body temperature mapping), among others. Active Thermography, on the other hand, studies previously excited samples, to retrieve information out of the temperature changes.

Active Infrared Thermography actually belongs to the family of the so-called *Photothermal Techniques*, among which we can also find Thermorreflectance, Photodeformation, “Mirage”, Photoacoustic and Photopyroelectric. All of them are based on the photothermal effect, which consists of a sample absorbing an intensity variable light beam and a thermal wave being generated in response, which is propagated along the sample, as well as on the surroundings. As the propagation depends on the properties and internal structure of the material, the detection of the effects produced by the thermal waves will reveal the material information. In that way, Infrared Thermography measures the temperature change in the sample by recording the changes in the infrared emission from the material surface.

Besides, depending on the way of exciting the sample, Infrared Thermography may be pulsed or modulated. Pulsed Thermography consists of heating briefly the sample and then recording the temperature evolution. The main advantage is the quickness of the experiment, from a few milliseconds, enough to measure good thermal

conductors, up to no more than a few seconds, needed for low conductivity samples. Modulated Thermography (Lock-in), in its turn, excites the samples by means of an intensity modulated light beam, so that the periodic energy deposition on the material surface generates thermal waves inside the samples and the resulting oscillating temperature field is recorded. Needed time for this technique is longer, but in return, data show better quality signals and so, much more accurate results. As this thesis deals with material characterization, mainly for poor thermal conductors, and accurate results are required, Lock-in Thermography will be the selected technique.

Lock-in Thermography took its first steps as Photothermal Radiometry, where a monolithic infrared detector records the temperature over a small area in the surface. The necessity to scan each point of the sample surface made it a high time-consuming technique used only for the strictly necessary cases. However, the development of the IRPFAs promoted the current Lock-in Thermography, where a matrix of infrared detectors is able to map the surface temperature at once. Thus, IR video cameras with fast data acquisition and high lateral resolution provided the necessary tools for fast thermal characterization of materials.

Since then, Lock-in Thermography has been widely used to measure thermal properties of materials with flat and parallel surfaces, in particular thermal diffusivity (D), which is a magnitude related to the speed of propagation of heat during changes of temperature over time. The traditional method to measure the thermal diffusivity of this kind of materials is the so-called phase method, with two possibilities. On the one hand, samples of a known thickness may be studied with plane illumination. For them, the temperature of the rear surface is measured as a function of the modulation frequency, and the representations of the phase and the natural logarithm of the amplitude as a function of the square root of the frequency show a linear behaviour from whose slopes the in-depth thermal diffusivity may be retrieved. On the other hand, focused illumination may be used, for which modulation frequency is fixed and a temperature map of the front surface is recorded. In this case, amplitude and phase are represented as a function of the distance to the heating spot, and the slopes allow retrieving the in-plane thermal diffusivity.

Recently, industry interests have led to extend the methods to measure thermal diffusivity of samples with complex geometries, such as rods [3-5], tubes [6], balls [6-8], filaments [9, 10] and free standing thin films [11-13].

For these two last cases, overestimation in the retrieved diffusivity values has been observed when applying the slopes method [9-13]. *The first objective of this thesis is to clarify the mechanism responsible for the overestimation, related to the traditionally neglected contribution of heat losses by conduction to the gas, develop a complete theoretical model including all mechanisms and propose a simple and reliable method to measure accurately the thermal diffusivity.*

Moreover, some photothermal techniques (photoacoustic spectroscopy or mirage effect) have proven to be very accurate in measuring the optical absorption coefficient of gases, liquids and solids, competing with success against optical techniques in the extreme cases of weakly or highly absorbing materials [14-16]. *The second objective of this thesis is to perform a systematic study on the ability of modulated plane PTR to retrieve simultaneously and accurately both the in-depth thermal diffusivity (D) and the optical absorption coefficient (α) of homogeneous semitransparent samples, from both theoretical and experimental point of view, setting the limits of the technique.*

Further in the study, multilayered samples are considered. Since the seminal work by Mandelis and co-workers [17] modulated PTR has been used for thermal conductivity depth profile reconstruction of heterogeneous samples such as surface hardened steels [18-24], functionally graded materials [25] and partially cured dental resins [26]. In the last years, two works dealing with the application of modulated PTR to the simultaneous reconstruction of the in-depth varying absorption coefficient and thermal diffusivity of semitransparent heterogeneous samples have been published [27, 28]. Now in this thesis, the modulated PTR capability to obtain simultaneously α and D in multilayered semitransparent materials by applying the thermal quadrupole method is studied. The thermal quadrupole method, has been applied in the framework of heat conductive transfer to calculate the surface

temperature of opaque multilayered samples [29] and to calculate the combined radiative and conductive heat transfer in semitransparent bulk materials [30]. Here, *the objective is to extend the method to calculate the surface temperature of multilayered semitransparent samples in a compact way and to show two of its potential applications, one of them showing the effect of paint layers on the PTR measurements and the other one allowing the determination of thermal contact resistances between layers.*

This thesis is composed of five Chapters, including this introductory chapter.

Chapter 2 reviews the principles of infrared radiation and summarizes relevant studies in Infrared Thermography applied to thermal diffusivity measurements.

Chapter 3 develops the theoretical model to deal with thin films and filaments of low conductivity, considering heat losses effects and introducing the traditionally neglected heat losses by conduction to the gas. The experimental setup required to perform accurate measurements is also designed. Last, reliable results on thin films and filaments are presented, confirming the theoretical model and establishing the conditions and limits to measure thermal diffusivity of thin films and filaments by Lock-in Thermography.

Chapter 4 focuses on semitransparent samples, in particular, on the simultaneous measurement of both thermal diffusivity and optical absorption coefficient. First, the ability of modulated plane PTR to retrieve simultaneously these properties on homogeneous samples is tested. Next, multilayered samples are considered, and the thermal quadrupole method is extended to apply it to multilayer semitransparent samples in order to retrieve both properties in a compact way. Furthermore, some disturbing effects modifying the samples surface temperature are studied, such as heat losses, multiple reflexions of the incident light, transparency of the samples to the infrared and lateral heat diffusion. Last, a large collection of homogeneous samples of all optical possibilities are characterized, and also, two applications on the multilayers are presented, showing the effect of painting the samples and retrieving thermal contact resistances between layers.

Chapter 5 summarizes the posed hypothesis and theoretical models developed, together with the experimental results obtained, and extracts conclusions leading to assessments for future research.

In addition, a list of publications resulting from this thesis is presented.

2. Theoretical background

2.1. Thermal emission

Infrared radiation (IR) is the electromagnetic radiation in the wavelength region longer than visible light wavelengths, lying from 0.75 to 1000 μm . In turn, this IR spectrum can be divided into regions. Closest to the visible, the near infrared region corresponds to wavelengths between 0.75 and 1.5 μm . Next, the range between 1.5 to 20 μm is called middle infrared. Last, the far infrared region ranges from 20 to 1000 μm .

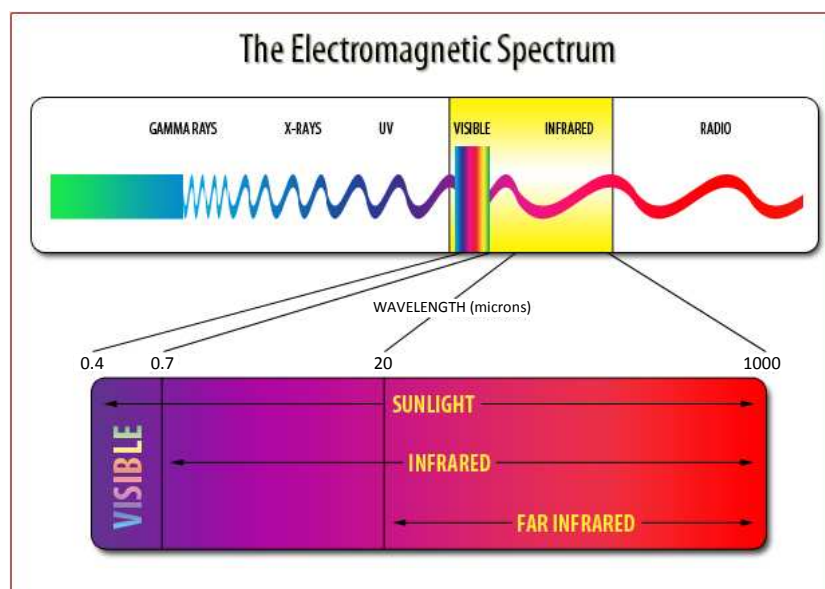


Figure 2.1: Electromagnetic spectrum showing the infrared region.

The importance of infrared radiation lays on the fact that all objects with a temperature over 0 K emit (or absorb) infrared radiation, as it corresponds to vibrational and rotational movements of particles. In case of solid bodies, infrared emission energy depends on the surface nature, the body temperature, the wavelength and the direction.

It is worth introducing the concept of black body or perfect radiator. A black body is an object which completely absorbs radiation from any direction or wavelength, and is able to emit it in the same way until reaching the thermodynamic equilibrium. Thus, the intensity of the emitted radiation depends on the black body temperature and on the wavelength, being the same for all directions.

All considered, there are some laws governing the infrared emission from a black body, explained below.

As mentioned before, the temperature dependent infrared emission is not uniformly distributed in the wavelength spectrum. Spectral radiance for a black body is given by Planck's Law:

$$M_b(\lambda, T) = \frac{2\pi hc^2}{\lambda^5 \left[e^{\left(\frac{hc}{\lambda kT}\right)} - 1 \right]} \quad (2.1)$$

where $c = 3 \cdot 10^8$ m/s is the speed of light in vacuum, $h = 6.63 \cdot 10^{-34}$ Ws² is the Planck's constant and $k = 1.38 \cdot 10^{-23}$ WsK⁻¹ is the Boltzmann constant.

Sometimes, it can be found in a compact way:

$$M_b(\lambda, T) = \frac{c_1}{\lambda^5 \left[e^{\left(\frac{c_2}{\lambda T}\right)} - 1 \right]} \quad (2.2)$$

where the so-called first radiant constant is $c_1 = 3.74 \cdot 10^{-16}$ Wm² and the second radiant constant is $c_2 = 1.44 \cdot 10^{-2}$ mK.

In Figure 2.2 the spectral radiance of a black body at different temperatures is shown. As Planck's Law states, the infrared radiation is not uniformly distributed, but it shows a maximum for a specific wavelength and then it is reduced at both sides of the wavelength spectrum.

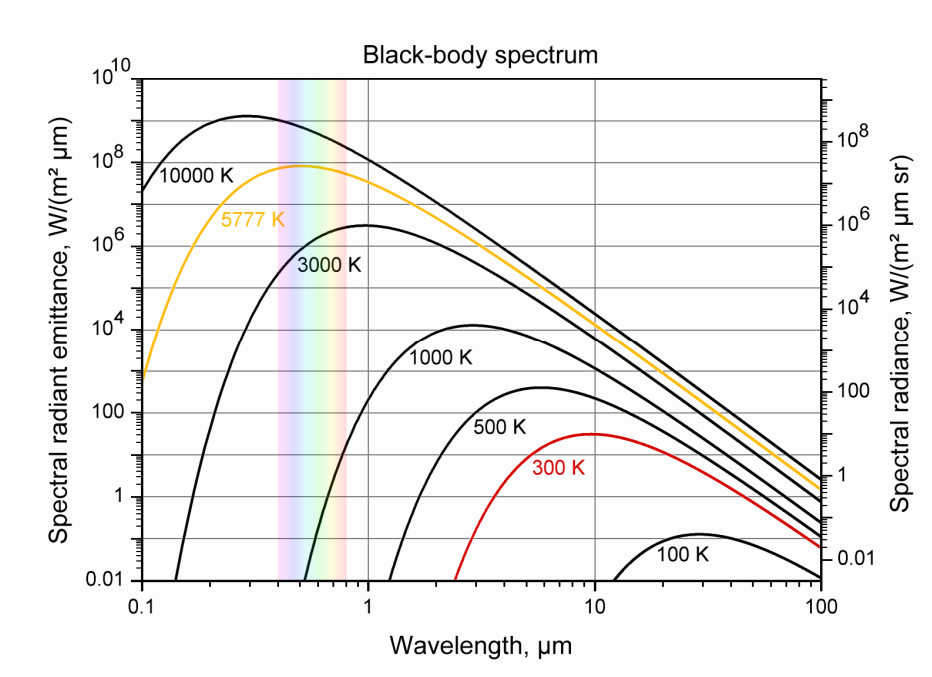


Figure 2.2: Spectral radiance of a black body for different temperatures according to Planck's Law.

In certain situations, Planck's Law can be simplified. Wien's Law is the approximation of Planck's Law for short wavelengths, $\lambda T \ll c_2$, so that the spectral radiance becomes:

$$M_b(\lambda, T) = \frac{c_1}{\lambda^5} e^{-\left(\frac{c_2}{\lambda T}\right)} \quad (2.3)$$

For long wavelengths, $\lambda T \gg c_2$, Rayleigh-Jeans Law takes place and the spectral radiance can be expressed:

$$M_b(\lambda, T) = \frac{c_1}{c_2} \frac{T}{\lambda^4} \quad (2.4)$$

showing a linear dependence of the radiance with temperature for this range.

It becomes useful determining the λ_{max} , for which the radiance of a black body at a temperature T reaches a maximum. Maximizing Planck's Law with respect to the wavelength, Wien's Displacement Law is obtained:

$$\lambda_{max} = \frac{2898}{T} \text{ } \mu\text{m} \quad (2.5)$$

Moreover, if the total radiance of a black body for all wavelengths is required, Planck's Law must be integrated from $\lambda = 0$ to $\lambda = \infty$. Thus, Stefan-Boltzmann's Law is obtained:

$$M_b(T) = k_B T^4 \quad (2.6)$$

where $k_B = 5.67 \cdot 10^{-8} \text{ W/m}^2\text{K}^4$ is the Stefan-Boltzmann constant.

Concerning the fact mentioned before that infrared emission depends on the object surface nature, we note that for a black body, laws of infrared emission do not include any parameter on it, as it is a kind of ideal surface absorbing and emitting all possible radiation according to its temperature and wavelength. So as to account for a real surface, we introduce a parameter determining the absorbing capacity of a body surface, the emissivity:

$$\varepsilon(T) = \frac{M(T)}{M_b(T)} \quad (2.7)$$

As it is observed, the emissivity of a body is the ratio of the total radiance of that body to the total radiance of a black body at that temperature. Emissivity depends on the wavelength, temperature and direction of the emitted radiation, and can vary from $\varepsilon = 0$ to $\varepsilon = 1$, which would be the case of a black body.

This considered, a correction should be included to the laws of infrared emission explained above, as they were for black bodies. Hence, Planck's Law for a real surface states:

$$M_b(\lambda, T) = \varepsilon(\lambda, T) \frac{2\pi hc^2}{\lambda^5 \left[e^{\left(\frac{hc}{\lambda kT}\right)} - 1 \right]} \quad (2.8)$$

while Stefan-Boltzmann's Law results:

$$M_b(T) = \varepsilon(T) k_B T^4 \quad (2.9)$$

As we may note, in Infrared Thermography, where a detector records the radiance emitted by the sample surface to obtain the temperature field of the sample, the uncertainty about the emissivity of the sample becomes a major problem.

However, in modulated IRT, only the changes of temperature are significant to retrieve information, regardless of the absolute temperature values. Besides, for small changes of temperature, just what we often need in a IRT experiment, the emissivity value can be considered constant.

In addition to this, it is worth noting that Infrared Thermography is a non-contact technique. In that sense, one should consider that infrared radiation emitted from the sample surface must travel to the detector through the atmosphere, and in that way, a part of the radiation could be absorbed by the atmosphere. Even more, thermal radiation from objects in the room could contribute to the radiation reaching the detector, causing the detector to observe an apparent temperature of the sample different from the real one.

It is true that the remote sensing devices are equipped with detector materials coincident with the so-called "atmospheric windows". Remembering infrared radiation corresponds to vibrational and rotational energy of molecules, the ones composing the atmosphere are able to absorb part of the infrared radiation from the sample in the way to the detector. But as it is shown in Figure 2.3, the absorption

diagram of the atmosphere reveals two areas, from 3 to 5 μm and from 8 to 12 μm , where a low absorption occurs, what means that a better transmission of the infrared radiation would take place.

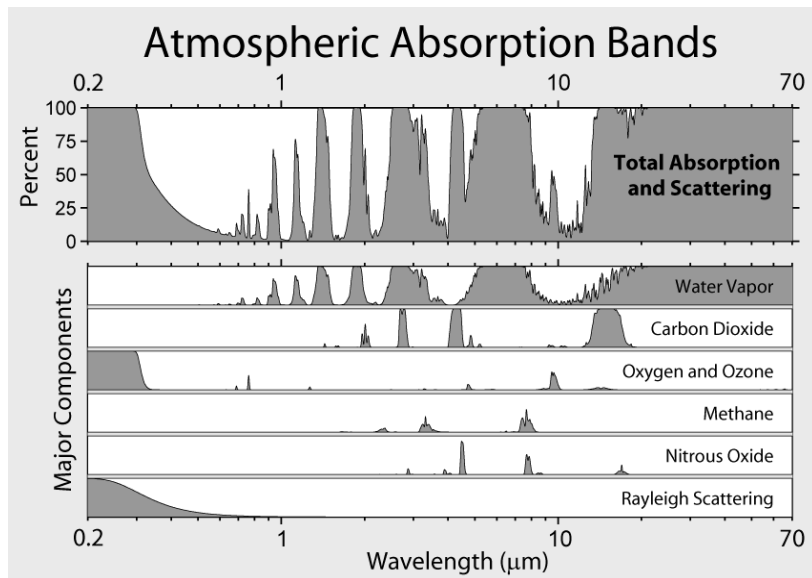


Figure 2.3: Wavelength spectrum of the atmospheric and its major components absorption.

In spite of this good transmission in the detection wavelength, it is worth remembering that absolute temperatures were not needed, but only changes of temperatures. Hence, it is not a problem that the atmosphere absorbs some of the radiation or even the room emits infrared reaching the detector, as none of them are modulated infrared radiation, and in consequence, will not affect the experiments.

Back to the aim of the thesis, infrared radiation reviewed so far is a product of the light absorption of the sample, transformation into heat, propagation through the material, and lastly emission as infrared, revealing information on the sample characteristics. Therefore, let us study the heat conduction through the material ending in infrared emission from the sample surface.

2.2. Heat conduction

As it is the purpose of this thesis to study the thermal and optical properties of materials by means of infrared lock-in thermography, based on the photothermal effect, it becomes useful reviewing how the heat generated by absorption of light is propagated around the material.

The heat conduction equation for homogeneous and isotropic samples is [31]:

$$\nabla^2 T(\vec{r}, t) - \frac{1}{D} \frac{\partial T(\vec{r}, t)}{\partial t} = -\frac{Q(\vec{r}, t)}{K} \quad (2.10)$$

where $Q(\vec{r}, t)$ is the absorbed energy per unit time and unit volume, D is the thermal diffusivity and K the thermal conductivity of the material.

Being the source for the heating an intensity periodically modulated (frequency $f = \omega/2\pi$) light beam, so that $Q(\vec{r}, t) = Q_0(\vec{r})(1 + e^{i\omega t})$, we are interested in resolving the temperature field in the sample. This will be of the form $T(\vec{r}, t) = T_{Ambient} + T_{dc}(\vec{r}) + T_{ac}(\vec{r}, t)$. We can observe the total temperature is the result of the contributions of the ambient temperature, a stationary heating of the sample and a periodically varying component, which will show the same time dependence as the light source, $T_{ac}(\vec{r}, t) = T_{ac}(\vec{r})e^{i\omega t}$.

By substituting the temperature field in terms of each contribution into the heat conduction equation (2.10), the following separate equations are obtained:

$$\begin{aligned} \nabla^2 T_{dc}(\vec{r}) &= -\frac{Q_0(\vec{r})}{K} \\ \nabla^2 T_{ac}(\vec{r}, t) - \frac{1}{D} \frac{\partial T_{ac}(\vec{r}, t)}{\partial t} &= -\frac{Q(\vec{r}, t)}{K} \rightarrow \nabla^2 T_{ac}(\vec{r}) - \sigma^2 T_{ac}(\vec{r}) = -\frac{Q_0(\vec{r})}{K} \end{aligned} \quad (2.11)$$

where $\sigma = \sqrt{i\omega/D}$.

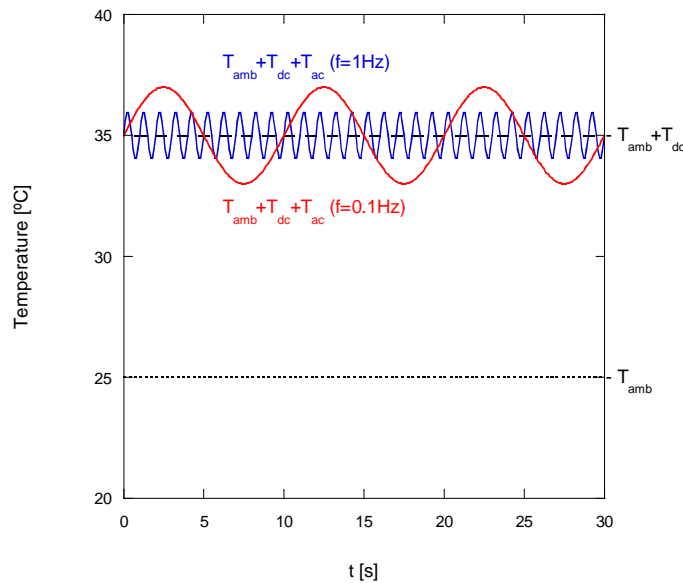


Figure 2.4: Scheme showing the ambient, stationary and periodic contributions to the temperature field in a sample.

Infrared lock-in thermography deals with the detection and study of the periodic component of the temperature, T_{ac} . Therefore, the knowledge of how heat propagates along a material lies in the solution and analysis of the Helmholtz equation (2.11).

As we may note, the temperature field in the sample depends on the shape of the excitation as well as on the thermal properties of the material.

2.3. Thermal diffusivity measurements

Both Photothermal Radiometry (PTR) and Infrared Thermography (IRT) are techniques we can obtain thermal properties with. Thus, thermal diffusivity, D , becomes available from surface temperature measurements through the heat conduction equation. In addition to homogeneity and isotropy conditions for the materials, we focus the study on opaque and semiinfinite samples. Opacity means all the energy is absorbed and transformed into heat at the surface, and being semiinfinite refers to the absence of lateral borders. Besides, we consider, as a first

approach, no heat losses to the surroundings of the samples neither by conduction, convection nor radiation.

The following sections deal with the solution of equation (2.11) for particular cases and the methods to retrieve thermal diffusivity.

2.3.1. Semiinfinite sample

A. Plane illumination

We consider an also in-depth semiinfinite sample as it is shown in Figure 2.5, where a modulated plane light beam incises.

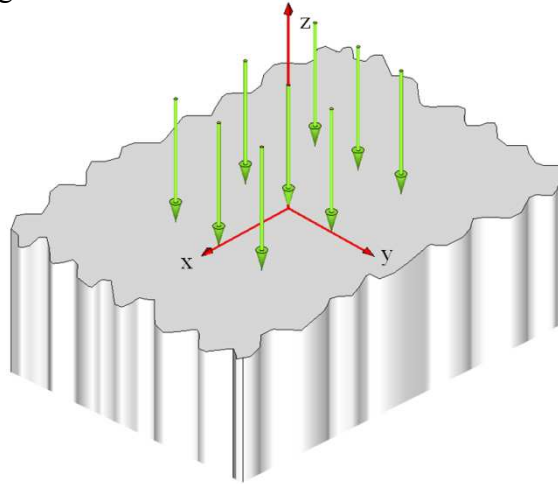


Figure 2.5: Semiinfinite sample illuminated by a plane light beam.

Being the intensity of the plane beam I_0 (W/m²) and assuming it is all absorbed, nothing reflected, the homogeneous Helmholtz equation is solved

$$\frac{d^2 T_{ac}(z)}{dz^2} - \sigma^2 T_{ac}(z) = 0 \rightarrow T_{ac}(z) = Ae^{\sigma z} + Be^{-\sigma z} \quad (2.12)$$

where A and B are constants. The temperature is represented by plane thermal waves travelling along $z > 0$ and $z < 0$. In order to determine the constants, we apply the boundary condition of heat flux continuity at the sample surface ($z=0$),

$$K \left. \frac{dT_{ac}(z)}{dz} \right|_{z=0} = \frac{I_0}{2} \quad (2.13)$$

and, as the sample is semiinfinite in z , we note that the second contribution to the temperature has no physical meaning, so that $B=0$. Therefore, the field of temperature results

$$\begin{aligned} T_{ac}(z) &= \frac{I_0}{2K\sigma} e^{\sigma z} = \\ &= \frac{I_0\mu}{2K\sqrt{2}} e^{\frac{1}{\mu}z} e^{i\left(\frac{1}{\mu}z - \frac{\pi}{4}\right)} = \frac{I_0\sqrt{D}}{2K\sqrt{2\pi f}} e^{\sqrt{\frac{\pi f}{D}}z} e^{i\left(\sqrt{\frac{\pi f}{D}}z - \frac{\pi}{4}\right)} = \frac{I_0}{2\varepsilon\sqrt{2\pi f}} e^{\sqrt{\frac{\pi f}{D}}z} e^{i\left(\sqrt{\frac{\pi f}{D}}z - \frac{\pi}{4}\right)} \end{aligned} \quad (2.14)$$

where $\mu = \sqrt{D/\pi f}$ is the thermal diffusion length, a parameter that measures the depth penetration of a thermal wave in a material, and $\varepsilon = K/\sqrt{D}$ is the thermal effusivity, which measures the ability of the material to exchange heat with the environment.

Equation (2.14) shows that in this case of plane illumination of a semiinfinite sample, the thermal wave generated spreads out as a damped plane wave. As the measurement available with IRT is the temperature of the front ($z=0$) surface of the sample,

$$T_{ac}(z=0) = \frac{I_0}{2\sqrt{2\pi f}} \frac{1}{\varepsilon} e^{-i\frac{\pi}{4}}$$

In Figure 2.6 the natural logarithm of the amplitude and the phase of that surface temperature are depicted separately as a function of the modulation frequency (in logarithmic scale). The natural logarithm of the amplitude shows a linear behaviour whose slope is $m = -0.5$, whereas the phase remains constant for every frequency at -45° . In this case, the thermal diffusivity cannot be retrieved.

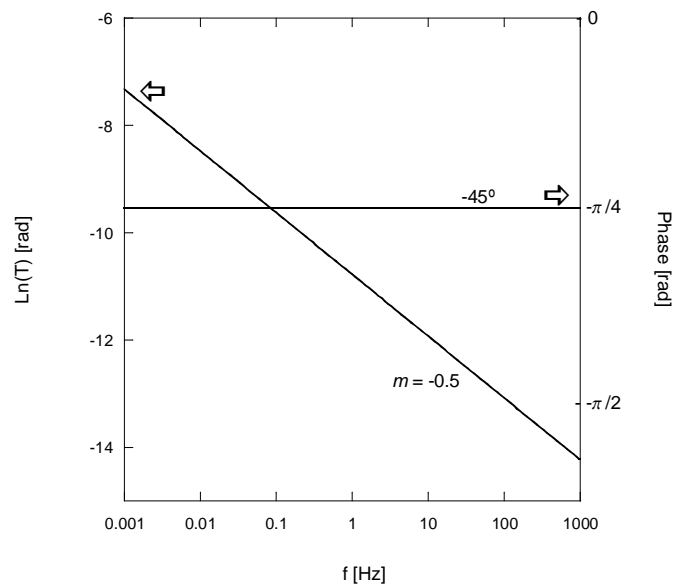


Figure 2.6: Phase and natural logarithm of the amplitude of the surface ($z=0$) temperature of a semiinfinite sample ($D=0.10 \cdot 10^{-6} \text{ m}^2/\text{s}$, $K=0.3 \text{ W/mK}$) illuminated by a plane light beam as a function of the modulation frequency.

B. Focused illumination

Now, the same previous sample is illuminated, this time by a focused light beam, as Figure 2.7 shows.

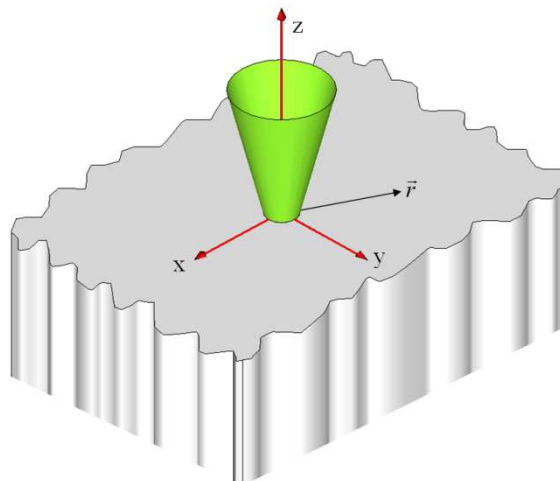


Figure 2.7: Semiinfinite sample illuminated by a focused light beam.

This beam, whose power is P_0 (W) with a Gaussian profile of radius a (at $1/e^2$), produces at the sample's surface ($z=0$) an incoming flux

$$\Phi(r) = \frac{P_0}{\pi a^2} e^{-2r^2/a^2} \quad (2.15)$$

The symmetry of the problem suggests working with cylindrical coordinates, r and z (there is no dependence on the angle), so that the homogeneous Helmholtz equation is

$$\nabla^2 T_{ac}(r, z) - \sigma^2 T_{ac}(r, z) = 0 \quad (2.16)$$

In order to solve the temperature field we work in the Hankel space. Thus, the Hankel transform of equation (2.16) is

$$\int_0^\infty [\nabla^2 T_{ac}(r, z) - \sigma^2 T_{ac}(r, z)] J_0(\delta r) r dr = 0$$

where δ is the Hankel variable and J_0 is the Bessel function of zeroth order.

Now we develop this equation by applying the Hankel transform properties [32]

$$\begin{aligned} \int_0^\infty [\nabla^2 T_{ac}(r, z)] J_0(\delta r) r dr - \sigma^2 \int_0^\infty [T_{ac}(r, z)] J_0(\delta r) r dr = 0 \\ \int_0^\infty \left[\frac{\partial^2 T_{ac}(r, z)}{\partial r^2} + \frac{1}{r} \frac{\partial T_{ac}(r, z)}{\partial r} \right] J_0(\delta r) r dr + \int_0^\infty \left[\frac{\partial^2 T_{ac}(r, z)}{\partial z^2} \right] J_0(\delta r) r dr - \\ - \sigma^2 \int_0^\infty [T_{ac}(r, z)] J_0(\delta r) r dr = 0 \end{aligned}$$

Considering $\bar{T}_{ac}(\delta, z) = \int_0^\infty [T_{ac}(r, z)] J_0(\delta r) r dr$ is the Hankel transform of the temperature, we obtain

$$-\delta^2 \bar{T}_{ac}(\delta, z) + \frac{\partial^2 \bar{T}_{ac}(\delta, z)}{\partial z^2} - \sigma^2 \bar{T}_{ac}(\delta, z) = 0 \rightarrow \frac{\partial^2 \bar{T}_{ac}(\delta, z)}{\partial z^2} - (\sigma^2 + \delta^2) \bar{T}_{ac}(\delta, z) = 0$$

If we call $\beta^2 = \delta^2 + \sigma^2$, then we find that the Hankel transform of equation (2.16) is

$$\frac{\partial^2 \bar{T}_{ac}(\delta, z)}{\partial z^2} - \beta^2 \bar{T}_{ac}(\delta, z) = 0 \quad (2.17)$$

We may note then, that the Hankel transform of the homogeneous Helmholtz equation for focused illumination (2.17) looks the same as the homogeneous Helmholtz equation for plane illumination (2.12), just exchanging $\sigma \leftrightarrow \beta$.

Therefore, we have found a method to easily solve the temperature field for focused illumination: working in the Hankel space. Thus, the Hankel transform of the temperature for focused illumination is the same as the temperature for plane illumination, changing $\sigma \rightarrow \beta$.

Regarding the boundary conditions, note that they must be also worked in the Hankel space. This way, the transform of the incoming flux produced by a focused beam (2.15) is

$$\bar{\Phi}(\delta) = \frac{P_0}{4\pi} e^{-\delta^2/8} \quad (2.18)$$

In order to summarize the procedure to obtain the temperature for the focused case out of the temperature for the plane one (or vice versa), the changes are exposed below:

Plane beam		Focused beam
$T_{ac}(z)$	\rightarrow	$\bar{T}_{ac}(\delta, z)$
σ	\rightarrow	β
$\frac{I_0}{2}$	\rightarrow	$\frac{P_0}{4\pi} e^{-\delta^2/8}$

Table 2.1: Table of elements to replace so as to change from plane to focused illumination.

Once we get the Hankel transform of the temperature for the focused case, the temperature will be obtained applying the inverse transform

$$T_{ac}(r, z) = \int_0^\infty \bar{T}_{ac}(\delta, z) J_0(\delta r) \delta d\delta \quad (2.19)$$

Returning to the purpose of getting the field of temperature of an in-depth semiinfinite sample illuminated by a focused light beam, we apply the procedure summarized in Table 2.1 by making a comparison with the equation (2.14) for the plane beam case. Hence,

$$T_{ac}(z) = \frac{I_0}{2K\sigma} e^{\alpha z} \rightarrow \bar{T}_{ac}(\delta, z) = \frac{P_0}{4\pi K} \frac{e^{\beta z}}{\beta} e^{-(\delta a)^2/8} \quad (2.20)$$

And so, we perform the inverse transform to obtain the temperature

$$T_{ac}(r, z) = \frac{P_0}{4\pi K} \int_0^\infty \frac{e^{\beta z}}{\beta} e^{-(\delta a)^2/8} J_0(\delta r) \delta d\delta \quad (2.21)$$

It is still possible to get an analytical solution to this equation if we consider an ideal focusing of the laser beam ($a = 0$)

$$T_{ac}(r, z, a = 0) = \frac{P_0}{4\pi K} \int_0^\infty \frac{e^{\beta z}}{\beta} J_0(\delta r) \delta d\delta \longrightarrow T_{ac}(R, a = 0) = \frac{P_0}{4\pi K} \frac{1}{R} e^{-\sigma R} \quad (2.22)$$

[33]where we use the new coordinate $R = \sqrt{r^2 + z^2}$, appropriate for the spherical thermal wave spreading in this case. Besides, we may expand this solution (2.22) to clarify the properties of this thermal wave

$$T_{ac}(R, a = 0) = \frac{P_0}{4\pi K} \frac{1}{R} e^{-\frac{1}{\mu} R} e^{-i\frac{1}{\mu} R} = \frac{P_0}{4\pi K} \frac{1}{R} e^{-\sqrt{\frac{\mu}{D}} R} e^{-i\sqrt{\frac{\mu}{D}} R} \quad (2.23)$$

As we may see, both the phase, Ψ , and the natural logarithm of the amplitude multiplied by the distance, $Ln(TR)$, exhibit a linear dependence on the distance R ,

whose slope [11, 34], the same for both, lets us obtain the thermal diffusivity D according to

$$m_\psi = -1/\mu = -\sqrt{\pi f / D} = m_{\ln(TR)} \quad (2.24)$$

Figure 2.8 shows the temperature of the front surface ($z=0$) of this semiinfinite sample, the measurement available from IRT measurements, where the phase and the natural logarithm of the amplitude multiplied by the distance are depicted separately as a function of the distance to the heating spot. Black lines correspond to the temperature for an ideal focusing of the light beam (2.23), and as (2.24) states, the amplitude and phase contributions are represented by parallel straight lines. On the other hand, green lines account for equation (2.21), where the effect of a real beam focusing of radius $a = 500 \mu\text{m}$ has been considered. In spite of the large size of this radius, we observe the effect is only noticeable at close distances to the spot. Thus, at large distances the slopes preserve the same value as for the ideal case, allowing us then to work with the simpler ideal case, provided the data are taken sufficiently far away from the excitation point.

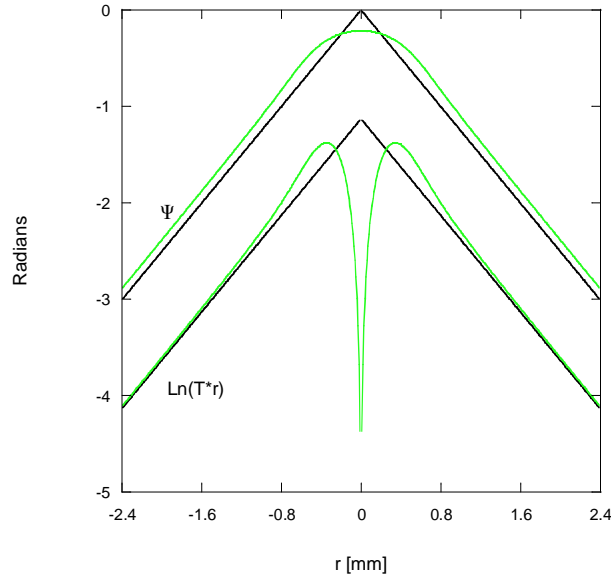


Figure 2.8: Phase and natural logarithm of the amplitude multiplied by the distance of the surface ($z=0$) temperature of a semiinfinite sample ($D=0.10 \cdot 10^{-6} \text{ m}^2/\text{s}$, $K=0.3 \text{ W/mK}$) illuminated by a modulated focused light beam ($f=0.05 \text{ Hz}$) as a function of the distance to the heating spot. Black lines represent an ideal focusing ($a=0$) of the light beam, while green ones account for the effect of a real beam focusing of radius $a=500 \mu\text{m}$.

2.3.2. Sheet

We work now with a sheet of thickness ℓ heated again by a plane or focused laser beam, as Figure 2.9 shows.

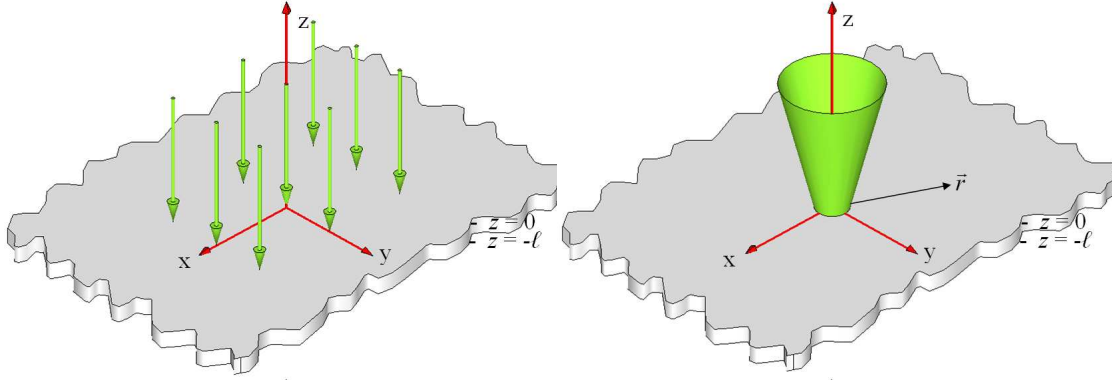


Figure 2.9: Sheet of thickness ℓ illuminated by a plane (left) or a focused (right) light beam.

We have to solve once more the Helmholtz equation (2.12), but this time with boundary conditions of heat flux continuity for both surfaces, $z=0$ and $z=-\ell$. We obtain first the temperature for plane illumination, and then we apply the procedure summarized in Table 2.1 together with the equation (2.19) to find the temperature for the focused case. The results are shown below.

Plane beam	Focused beam
$T_{ac}(z) = Ae^{\alpha z} + Be^{-\alpha z}$	$\bar{T}_{ac}(\delta, z) = Ce^{\beta z} + De^{-\beta z}$
$K \frac{dT_{ac}}{dz} \Big _{z=0} = \frac{I_0}{2}$	$K \frac{\partial \bar{T}_{ac}}{\partial z} \Big _{z=0} = \frac{P_0}{4\pi} e^{-(\delta a)^2/8}$
$K \frac{\partial T_{ac}}{\partial z} \Big _{z=-\ell} = 0$	$K \frac{\partial \bar{T}_{ac}}{\partial z} \Big _{z=-\ell} = 0$

Solution plane	Solution focused
$T_{ac}(z) = \frac{I_0}{2K\sigma} \left[\frac{e^{\sigma z} e^{\sigma \ell} + e^{-\sigma z} e^{-\sigma \ell}}{e^{\sigma \ell} - e^{-\sigma \ell}} \right]$ <p style="text-align: center;">(2.25)</p>	$\bar{T}_{ac}(\delta, z) = \frac{P_0}{4\pi K} \frac{e^{-(\delta a)^2/8}}{\beta} \left[\frac{e^{\beta z} e^{\beta \ell} + e^{-\beta z} e^{-\beta \ell}}{e^{\beta \ell} - e^{-\beta \ell}} \right]$ $T_{ac}(r, z) = \frac{P_0}{4\pi K} \int_0^\infty \frac{e^{-(\delta a)^2/8}}{\beta} \left[\frac{e^{\beta z} e^{\beta \ell} + e^{-\beta z} e^{-\beta \ell}}{e^{\beta \ell} - e^{-\beta \ell}} \right] J_0(\delta r) \delta d \delta$ <p style="text-align: center;">(2.26)</p>

It becomes interesting to study two special situations for these temperature fields, the extreme cases of a thermally thin or a thermally thick sheet. Thermal thickness refers to the thickness of the sample in comparison with the thermal diffusion length, μ . This way, a sample may be considered thermally thin when $\ell \ll \mu = \sqrt{D/\pi f}$, and so, the approximations

$$e^{\pm\sigma\ell} \approx 1 \pm \sigma\ell \text{ or } e^{\pm\beta\ell} \approx 1 \pm \beta\ell \quad (2.27)$$

may be applied. On the other hand, we call it thermally thick when $\ell \gg \mu = \sqrt{D/\pi f}$ what makes it possible to approximate

$$e^{-\beta\ell} \approx 0 \quad (2.28)$$

We show below the fields of temperature for these extreme cases.

A. Plane illumination

The temperature field of a sheet illuminated by a plane light beam is described in general terms by the equation (2.25). However, if we consider the special situations described above, the approximations (2.27) and (2.28) lead to the following simple equations

$$T_{ac}(z)_{thin} \approx \frac{I_0}{2K\sigma^2\ell} = \frac{I_0 D}{4\pi K \ell f} e^{-i\frac{\pi}{2}} \quad (2.29)$$

$$T_{ac}(z)_{thick} \approx \frac{I_0}{2K\sigma} e^{\alpha z} = \frac{I_0 \sqrt{D}}{2K \sqrt{2\pi f}} e^{\sqrt{\frac{\pi f}{D}} z} e^{i(\sqrt{\frac{\pi f}{D}} z - \frac{\pi}{4})} \quad (2.30)$$

which it becomes easier to obtain the diffusivity from. It is worth noting that in the case of a thermally thin sample the temperature does not depend on z , and in the case of a thermally thick one we find it is the same as for the semiinfinite sample (2.14).

In Figure 2.10 we find the temperatures of the front (left) and rear (right) surfaces as a function of the frequency, where we note that the thermal thickness depends on the modulation frequency. For the front temperature (left) we show separately the phase and the natural logarithm of the amplitude as a function of the frequency. The two extreme cases are clearly differentiated: thermally thick for high frequencies, where the slope of the amplitude $m=-0.5$ and the constant phase of -45° are characteristic of the semiinfinite sample; and thermally thin for low frequencies, where from equation (2.29) we observe a still linear behaviour of the amplitude but of slope $m=-1$ and a still constant phase but with a turn to -90° . In neither of these extreme cases of the front surface temperature is it possible to obtain the diffusivity value. On the other hand, for a sheet, measurements of the rear surface temperature (right) are available. We observe from equation (2.30) for the thick case that the phase and the natural logarithm of the amplitude multiplied by the square root of the frequency exhibit a linear behaviour with the square root of the frequency, whose slopes are

$$m_\psi = -\ell \sqrt{\pi/D} = m_{\ln(T\sqrt{f})} \quad (2.31)$$

and so let us obtain the thermal diffusivity. The slopes values are the same for both amplitude and phase, as we may check in Figure 2.10 (right) by looking at the parallelism in the thick range. The thin one, however, does not let us obtain information in a simple way.

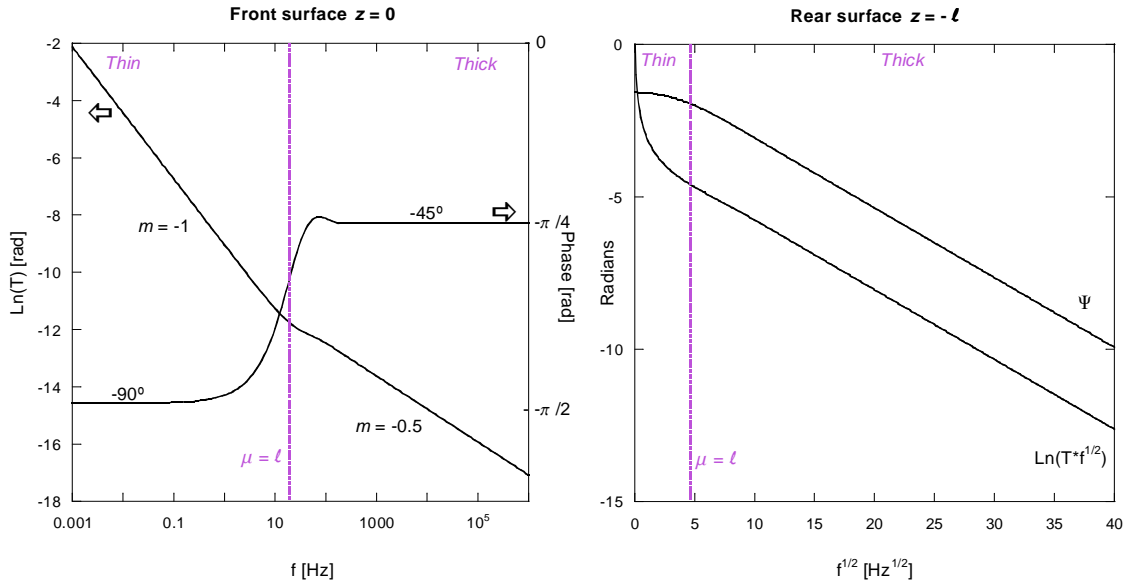


Figure 2.10: Sheet ($D=0.15 \cdot 10^{-6}$ m²/s, $K=0.2$ W/mK, $\ell=50 \cdot 10^{-6}$ m) illuminated by a plane light beam. Left: Phase and natural logarithm of the amplitude of the front surface ($z=0$) temperature as a function of the modulation frequency. Right: Phase and natural logarithm of the amplitude multiplied by the square root of the frequency of the rear surface ($z=-\ell$) temperature as a function of the square root of the frequency.

B. Focused illumination

The same way as for plane illumination, the general equation describing the field of temperature of a sheet illuminated by a focused light beam is (2.26), but the approximations above, (2.27) and (2.28), for special cases simplify the analysis to obtain the thermal diffusivity. Hence, for the thin case

$$T_{ac}(r, z)_{thin} \approx \frac{P_0}{4\pi K \ell} \int_0^\infty \frac{e^{-(\delta a)^2/8}}{\beta^2} J_0(\delta r) \delta d \delta \quad (2.32)$$

As for the semiinfinite sample, we consider an ideal focusing of the laser beam ($a=0$)

$$T_{ac}(r, z, a=0)_{thin} \approx \frac{P_0}{4\pi K \ell} K_0(\sigma r) \quad (2.33)$$

where K_0 is the Kelvin function of zeroth order. Then, we apply the asymptotic approach [33] of this function, as we analyse points far from the heating spot

$$T_{ac}(r \rightarrow \infty, z, a = 0)_{thin} \approx \frac{P_0}{4\pi K \ell} \sqrt{\frac{\pi}{2\sigma}} \frac{e^{-\sigma r}}{\sqrt{r}} = \frac{P_0}{4\pi K \ell} \sqrt{\frac{\pi}{2\sigma}} \frac{e^{-\sqrt{\frac{\pi f}{D}} r}}{\sqrt{r}} e^{-i\sqrt{\frac{\pi f}{D}} r} \quad (2.34)$$

It is worth noting that this wave is spreading as a cylindrical wave, which does not depend on the coordinate z . As we may observe (Figure 2.11), both the phase and the natural logarithm of the amplitude multiplied by the square root of the distance show a linear behaviour with the distance to the heating spot, whose slopes are

$$m_\psi = -\sqrt{\pi f / D} = m_{\ln(T\sqrt{r})} \quad (2.35)$$

from which it becomes easy to obtain the thermal diffusivity. Again both slopes present the same value, what we can check from the parallelism of them in the graphics.

Regarding the ideal focusing approximation, we show here, as in the semiinfinite sample, that, but for the points close to the heating spot, the effect of the approximation is negligible. Far away from the heating spot, the graph shows that the slopes of the real focusing (green lines) are the same as the ones of the ideal focusing (black lines). Thus, it lets us consider the ideal focusing in order to simplify the analysis. Anyway, it is worth noting that in this case, even for the ideal case, the singularity in $r=0$ makes it impossible to use points close to the heating spot by means of the slopes method.

For the thick case, by applying the approximation (2.28) we get

$$T_{ac}(r, z)_{thick} \approx \frac{P_0}{4\pi K} \int_0^\infty \frac{e^{-(\delta a)^2/8}}{\beta} e^{\beta z} J_0(\delta r) \delta d\delta \quad (2.36)$$

which is the same temperature as for the semiinfinite case (2.21). Thus, the results are depicted in Figure 2.8.

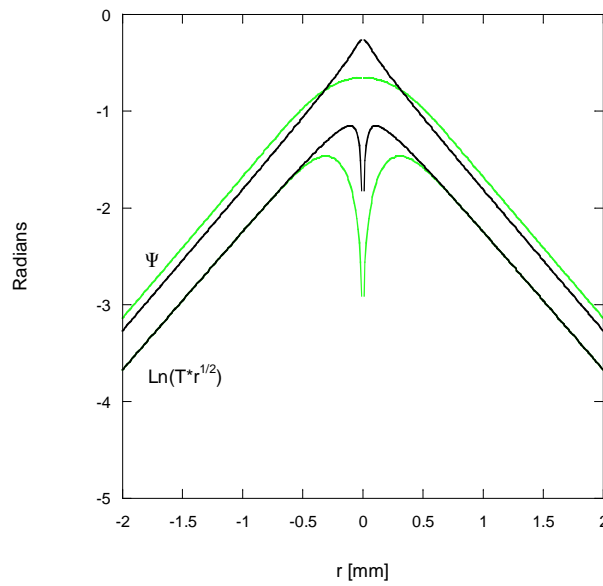


Figure 2.11: Phase and natural logarithm of the amplitude multiplied by the square root of the distance of the surface ($z=0$) temperature of a thermally thin sheet ($D=0.15 \cdot 10^{-6} \text{ m}^2/\text{s}$, $K=0.2 \text{ W/mK}$, $\ell=50 \cdot 10^{-6} \text{ m}$) illuminated by a modulated focused light beam ($f=0.1 \text{ Hz}$) as a function of the distance to the heating spot. Black lines represent an ideal focusing ($a=0$) of the light beam, while green ones account for the effect of a real beam focusing of radius $a=500 \text{ }\mu\text{m}$.

In general, IRT measurements allow the thermal diffusivity retrieval both for semiinfinite samples and sheets in case of focused illumination, by means of the slopes method. However, if plane illumination is applied, only thermally thick sheets from the rear surface will provide useful results.

Besides, it is worth noting that the effect of an ideal approximation for the focusing of the illumination has no influence on the retrieved diffusivity values, as long as the measurements are performed far enough from the heating spot.

2.4. Heat losses

In the previous section heat conduction through the materials was reviewed, assuming there was no heat losses to the surroundings. Now, a more realistic model is considered including heat losses, so that the heat propagation would be as it is schemed below in terms of fluxes:

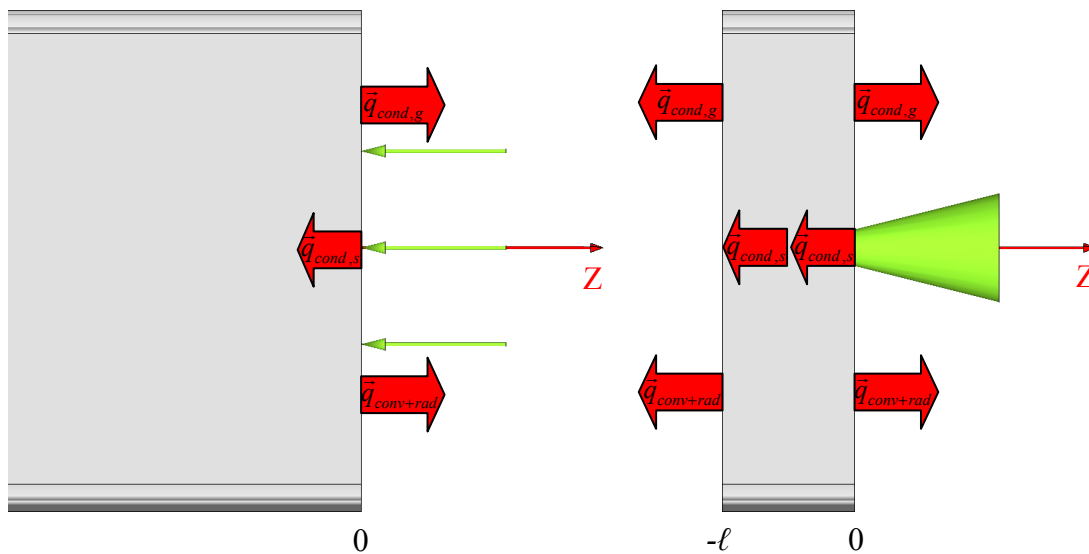


Figure 2.12: Heat fluxes diagram for a semiinfinite sample (left) and a sheet (right). The illumination is either plane or focused.

As we may see, convection is one of the contributions to the heat losses. This heat transfer happens when a fluid (air) is in contact with a solid surface at a higher temperature, what originates a circulation of the fluid. The convection flux in our case, being the temperature rise small, behaves linearly with the surface temperature, as the Newton's Law of Cooling states, $q_{cv} = h_{cv} (T_s - T_\infty)$, where T_s is the surface temperature, T_∞ is the temperature of the fluid far away from the surface, and h_{cv} is the convection coefficient. This coefficient depends on the properties of the fluid as well as on the kind of air movement and the size and orientation of the surface. An estimation for a vertical slab would be $h_{cv} \approx 1.5 (\Delta T / height)^{0.25}$, as a function of the temperature difference between the surface and the fluid and the height of the sample [35]. For instance, a vertical slab at about 30° C surrounded by air at 20° C would

have convection losses with a coefficient $h_{cv} = 8.5 \text{ W/m}^2\text{K}$ (height of the sample: 1cm) or $h_{cv} = 4.8 \text{ W/m}^2\text{K}$ (height 10 cm).

Another contribution to the heat losses is the thermal radiation. This heat transfer takes place between two surfaces at different temperatures by means of electromagnetic waves, which implies there is no need of matter to be propagated. The radiation behaviour is described by the Stefan-Boltzmann's Law, $q_{emitted} = \varepsilon k_B T_s^4$, where ε is the emissivity of the sample surface, k_B is the Stefan-Boltzmann's constant and T_s is the surface temperature. Thus, the net radiated flux of the sample, considering it interacts with the surroundings, is $q_{rad} = q_{emitted} - q_{absorbed} = \varepsilon k_B T_{surface}^4 - \alpha k_B T_{surroundings}^4$, where α is the absorptivity of the sample surface. In order to balance the radiation exchange between the sample and the surroundings, the Kirchoff's Identity ($\varepsilon=\alpha$) is applied, so that it results $q_{rad} = \varepsilon k_B (T_{surface}^4 - T_{surroundings}^4)$.

If the surface temperature is taken as $T_{surface} = T_{surround} + \Delta T$, and remembering the temperature rise in our case will be small, which means $\Delta T \ll T_{surround}$, the following approximation can be applied:

$$q_{rad} = \varepsilon k_B ((T_{surround} + \Delta T)^4 - T_{surround}^4) \approx 4\varepsilon k_B T_{surround}^3 \Delta T = 4\varepsilon k_B T_{surround}^3 (T_{surface} - T_{surround})$$

This way we obtain that the radiative coefficient is $h_{rad} \approx 4\varepsilon k_B T_{surround}^3$ [36], so we can estimate its maximum ($\varepsilon=1$) value at room temperature, resulting $h_{rad} \approx 6 \text{ W/m}^2\text{K}$.

Considering both convection and radiation contributions all together, we may establish a combined coefficient $h = h_{cv} + h_{rad}$, which would result, with the previous estimations, in a maximum value at room temperature of about $h \approx 15 \text{ W/m}^2\text{K}$.

Regarding the contribution of the heat conduction to the gas, which transfers the heat by interaction among the molecules without a net flux of matter, it is described by

the Fourier's Law, $q_{conduction} = -K_g \nabla T$, where K_g is the conductivity of the gas, but it is usually neglected due to the gas low conductivity value, $K_{air}=0.026$ W/mK.

Proceeding the same way as in the previous section to solve the field of temperature in the samples, we add now the heat losses by convection and radiation to the boundary conditions.

2.4.1. Semiinfinite sample

For a semiinfinite sample, the equations, boundary conditions and solutions are exposed below:

Plane beam	Focused beam
$T_{ac}(z) = Ae^{\alpha z}$	$\bar{T}_{ac}(\delta, z) = Ce^{\beta z}$
$K \frac{dT_{ac}}{dz} \Big _{z=0} = \frac{I_0}{2} - hT_{ac} \Big _{z=0}$	$K \frac{\partial \bar{T}_{ac}}{\partial z} \Big _{z=0} = \frac{P_0}{4\pi} e^{-(\delta a)^2/8} - h\bar{T}_{ac} \Big _{z=0}$
Solution plane	Solution focused
$T_{ac}(z) = \frac{I_0}{2K\sigma} \left[\frac{e^{\alpha z}}{1 + H_p} \right]$	$\bar{T}_{ac}(\delta, z) = \frac{P_0}{4\pi K} \frac{e^{-(\delta a)^2/8}}{\beta} \left[\frac{e^{\beta z}}{1 + H_f} \right]$
(2.37)	$T_{ac}(r, z) = \frac{P_0}{4\pi K} \int_0^\infty \frac{e^{-(\delta a)^2/8}}{\beta} \left[\frac{e^{\beta z}}{1 + H_f} \right] J_0(\delta r) \delta d\delta$
	(2.38)

where h is the combined coefficient for convection and radiation losses, and so $H_p = h/K\sigma$ and $H_f = h/K\beta$ are the terms accounting for the heat losses by these mechanisms for plane and focused illumination, respectively.

The effect of heat losses on the front surface temperature is shown in Figure 2.13.

For plane illumination (left) heat losses show little effect on the amplitude and phase of the surface temperature, even at the extreme situation depicted with heat losses of a much higher value, $h=50 \text{ W/m}^2\text{K}$, than the maximum estimated at room temperature, $h=15 \text{ W/m}^2\text{K}$. It is only at low frequencies when we observe a slight deviation from the straight lines representative of the adiabatic case. Concerning the focused illumination (right), we realise there is no analytical solution for the equation (2.38) as we found for the adiabatic case (2.23) which led to the slopes calculation (2.24). Observing the graphics, both effects, $h=15 \text{ W/m}^2\text{K}$ (purple) and $h=50 \text{ W/m}^2\text{K}$ (red), are plotted in order to check that even at this low diffusivity and low frequency example, the maximum estimated effect has scarce influence on the parallel slopes of the adiabatic case. Only for an excessive coefficient $h=50 \text{ W/m}^2\text{K}$, the curves are deviated. As we may observe, the phase turns upwards, decreasing the slopes absolute value, whereas the amplitude turns downwards, causing the opposite effect. Besides, it is worth noting that the change is not the same for both, but the amplitude experiments a higher effect.

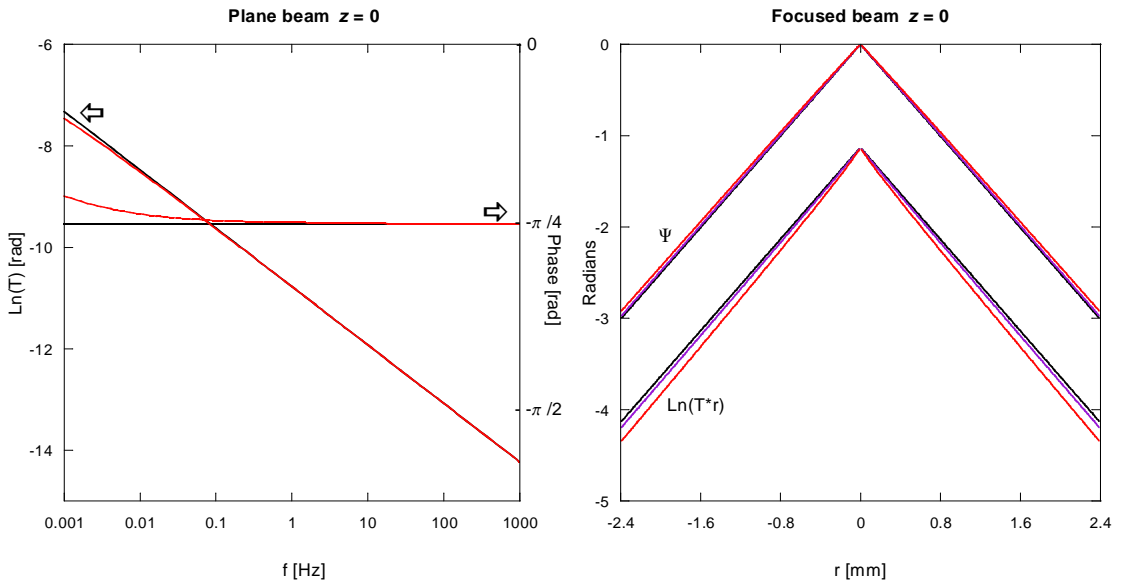


Figure 2.13: Front surface ($z=0$) temperature of a semiinfinite sample ($D=0.10 \cdot 10^{-6} \text{ m}^2/\text{s}$, $K=0.3 \text{ W/mK}$) illuminated by a plane light beam (left, as a function of the modulation frequency) and a focused ($f=0.05 \text{ Hz}$) light beam (right, as a function of the distance to the heating spot). Black lines represent the temperature without heat losses to the surroundings of the sample whereas red lines account for the effect of heat losses by convection and radiation ($h=50 \text{ W/m}^2\text{K}$). Purple lines in the focused case represent the same effect of heat losses with $h=15 \text{ W/m}^2\text{K}$.

Generalizing, heat losses by convection and radiation have scarce influence on diffusivity measurements by IRT on bulk materials at room temperature.

2.4.2. Sheet

Regarding a sheet, the same procedure is considered, and so the results are:

Plane beam	Focused beam
$T_{ac}(z) = Ae^{\sigma z} + Be^{-\sigma z}$	$\bar{T}_{ac}(\delta, z) = Ce^{\beta z} + De^{-\beta z}$
$K \frac{dT_{ac}}{dz} \Big _{z=0} = \frac{I_0}{2} - hT_{ac} \Big _{z=0}$	$K \frac{\partial \bar{T}_{ac}}{\partial z} \Big _{z=0} = \frac{P_0}{4\pi} e^{-(\delta a)^2/8} - h\bar{T}_{ac} \Big _{z=0}$
$K \frac{\partial T_{ac}}{\partial z} \Big _{z=-\ell} = hT_{ac} \Big _{z=-\ell}$	$K \frac{\partial \bar{T}_{ac}}{\partial z} \Big _{z=-\ell} = h\bar{T}_{ac} \Big _{z=-\ell}$
Solution plane	Solution focused
$T_{ac}(z) = \frac{I_0}{2K\sigma} \cdot \left[\frac{e^{\sigma z} e^{\sigma \ell} (1+H_p) + e^{-\sigma z} e^{-\sigma \ell} (1-H_p)}{e^{\sigma \ell} (1+H_p)^2 - e^{-\sigma \ell} (1-H_p)^2} \right]$	$\bar{T}_{ac}(\delta, z) = \frac{P_0}{4\pi K} \frac{e^{-(\delta a)^2/8}}{\beta} \cdot \left[\frac{e^{\beta z} e^{\beta \ell} (1+H_f) + e^{-\beta z} e^{-\beta \ell} (1-H_f)}{e^{\beta \ell} (1+H_f)^2 - e^{-\beta \ell} (1-H_f)^2} \right]$
<p style="text-align: center;">(2.39)</p>	$T_{ac}(r, z) = \frac{P_0}{4\pi K} \cdot \int_0^\infty \frac{e^{-(\delta a)^2/8}}{\beta} \left[\frac{e^{\beta z} e^{\beta \ell} (1+H_f) + e^{-\beta z} e^{-\beta \ell} (1-H_f)}{e^{\beta \ell} (1+H_f)^2 - e^{-\beta \ell} (1-H_f)^2} \right] J_0(\delta r) \delta l \delta$ <p style="text-align: center;">(2.40)</p>

In order to show the effect of these heat losses, we study again the extreme cases of thermally thin and thermally thick sheets, as they lead to simple equations.

A. Plane illumination

The field of temperature of a sheet illuminated by a plane light beam with heat losses to the surroundings of the sample is described by equation (2.39). However, approximations (2.27) and (2.28) simplify it:

$$T_{ac}(z)_{thin} \approx \frac{I_0}{2K\sigma} \frac{1}{2H_p + \sigma\ell} = \frac{I_0}{2K\sigma'^2 \ell} \quad (2.41)$$

where we change the coordinates to $\sigma'^2 = \sigma^2 + \frac{2h}{K\ell}$.

Regarding the thick case we find

$$T_{ac}(z)_{thick} \approx \frac{I_0}{2K\sigma} \left[\frac{e^{\sigma z}}{1 + H_p} \right] \quad (2.42)$$

which is the same as (2.37) for the semiinfinite sample.

In Figure 2.14 we see the temperatures of the front (left) and rear (right) surfaces of a sheet illuminated by a plane beam. Black lines represent the adiabatic case while red ones account for the heat losses. As we may observe for both surfaces, heat losses only affect the thin region, at low frequencies, whereas the thick range remains unchanged. Thus, we may obtain the thermal diffusivity from the thick range at the rear surface temperature through the equations (2.31). Besides, let us point out that for the thin range, the thinner the sheet, the higher the effect of the heat losses.

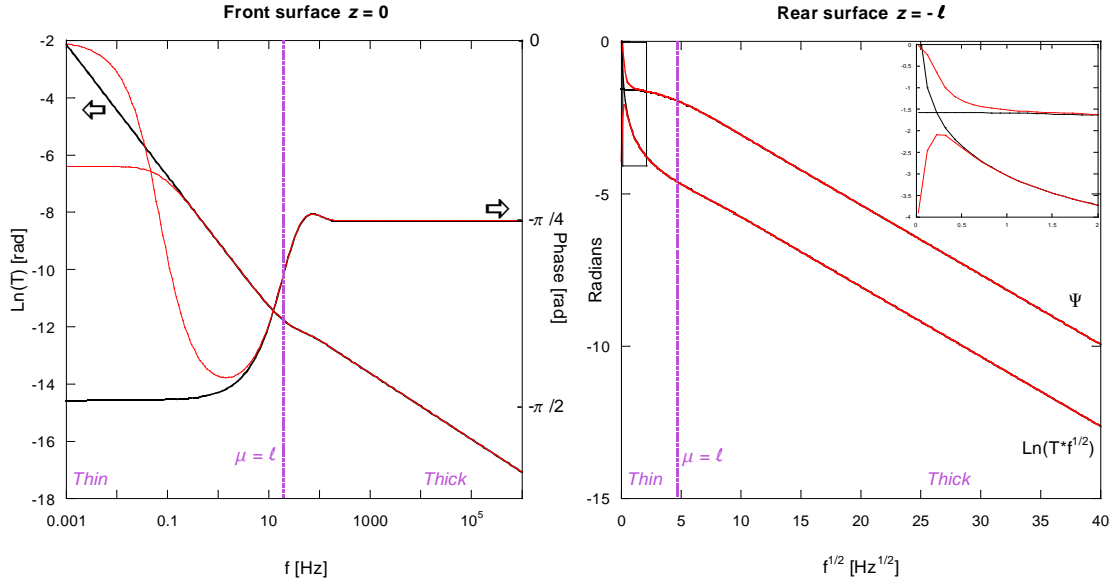


Figure 2.14: Front surface ($z=0$), on the left, and rear surface ($z=-\ell$), on the right, temperature of a sheet ($D=0.15 \cdot 10^{-6} \text{ m}^2/\text{s}$, $K=0.2 \text{ W/mK}$, $\ell=50 \cdot 10^{-6} \text{ m}$) illuminated by a plane light beam. Black lines represent the temperature without heat losses to the surroundings of the sample whereas red lines account for the effect of heat losses by convection and radiation ($h=15 \text{ W/m}^2\text{K}$).

B. Focused illumination

Now we study the field of temperature with heat losses of a sheet illuminated by a focused light beam (2.40) for the special cases of thermally thin and thick so as to simplify the analysis.

For the thermally thin approximation the temperature writes

$$T_{ac}(r)_{thin} \approx \frac{P_0}{4\pi K} \int_0^\infty \frac{e^{-(\delta a)^2/8}}{\beta} \left[\frac{1}{2H_f + \beta\ell} \right] J_0(\delta r) \delta d\delta = \frac{P_0}{4\pi K \ell} \int_0^\infty \frac{e^{-(\delta a)^2/8}}{\beta^2} J_0(\delta r) \delta d\delta \quad (2.43)$$

with the previous change of coordinates $\sigma^2 = \sigma^2 + \frac{2h}{K\ell}$ and so, $\beta^2 = \delta^2 + \sigma^2$. This equation is the same as (2.32) with the new variable. Then, performing the same way, which is considering ideal focusing of the laser beam and applying the asymptotic approach, we get

$$T_{ac}(r, a=0)_{thin} \approx \frac{P_0}{4\pi K \ell} K_o(\sigma' r) \rightarrow T_{ac}(r \rightarrow \infty, a=0)_{thin} \approx \frac{P_0}{4\pi K \ell} \sqrt{\frac{\pi}{2\sigma'}} \frac{e^{-\sigma' r}}{\sqrt{r}} \quad (2.44)$$

As we may observe from the equation (2.44) and the graphics in Figure 2.15, here again the phase and the natural logarithm of the amplitude multiplied by the square root of the distance show a linear behaviour with the distance to the heating spot, but this time the slopes are affected by the heat losses in such a way that the parallelism is lost, as the phase turns upwards whereas the amplitude does it downwards.

$$\left. \begin{aligned} m_\psi &= -\text{Re}[\sigma'] \\ m_{\ln(T\sqrt{r})} &= -\text{Im}[\sigma'] \end{aligned} \right\} \quad (2.45)$$

However, it is still possible to obtain the thermal diffusivity value, due to the fact that the product of the slopes is independent of heat losses [9, 12, 13]:

$$m_{\ln(\sqrt{r}T)} \times m_\psi = -\pi f/D \quad (2.46)$$

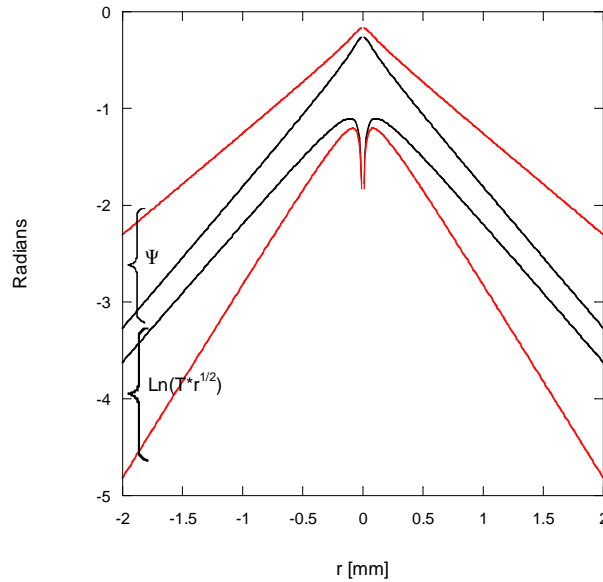


Figure 2.15: Front surface ($z=0$) temperature of a sheet ($D=0.15 \cdot 10^{-6} \text{ m}^2/\text{s}$, $K=0.2 \text{ W/mK}$, $\ell=50 \cdot 10^{-6} \text{ m}$) illuminated by a focused ($f=0.1 \text{ Hz}$) light beam as a function of the distance to the heating spot. Black lines represent the temperature without heat losses to the surroundings of the sample whereas red lines account for the effect of heat losses by convection and radiation ($h=15 \text{ W/m}^2\text{K}$).

For the thermally thick approximation the result is

$$T_{ac}(r, z)_{thick} \approx \frac{P_o}{4\pi K} \int_0^\infty \frac{e^{-(\delta i)^2/8}}{\beta} \left[\frac{e^{\beta z}}{1 + H_f} \right] J_o(\delta r) \delta l \delta \quad (2.47)$$

the same as for the semiinfinite sample. Thus, the effect is shown in Figure 2.13 (right).

In conclusion, heat losses by convection and radiation (conduction to the gas is usually neglected due to the low thermal conductivity of the air) hardly affect semiinfinite samples. For sheets, however, in spite of thermally thick samples, which behave as the semiinfinite ones, the effect on thermally thin samples is well noticeable. Concerning focused illumination, which it was possible to retrieve diffusivity values with, the effect of heat losses modifies the slopes of the temperature representations, but in such a way, that the product of the slopes corresponding to amplitude and phase cancels the effects and allows retrieving accurate diffusivity values.

2.5. Thermal quadrupole method

In previous sections we solved the full temperature field of samples and then we used the solution at front and rear surfaces to obtain the thermal diffusivity of the materials. Indeed, the only measurements available from Infrared Thermography experiments in IR opaque materials are the temperature fields of surfaces. In that sense, there is no need to analytically solve the full temperature field of a sample. The thermal quadrupole method [29], reviewed below, is a matrix method that provides a quick way to solve surface temperatures.

Let us consider a sheet of thickness ℓ illuminated by a plane light beam (Figure 2.9, left). For convenience, we express the temperature and heat flux in terms of hyperbolic functions, instead of the ordinary exponential functions:

$$\begin{cases} T_{ac}(z) = A \sinh(\sigma z) + B \cosh(\sigma z) \\ \Phi_{ac}(z) = -K \frac{dT_{ac}}{dz} = -K\sigma[A \cosh(\sigma z) + B \sinh(\sigma z)] \end{cases} \quad (2.48)$$

where A and B are constants. If we evaluate the equations at both surfaces, $z=0$ and $z=-\ell$, we get

$$\begin{cases} T_{ac}(0) = B \\ \Phi_{ac}(0) = -K\sigma A \\ T_{ac}(-\ell) = -A \sinh(\sigma \ell) + B \cosh(\sigma \ell) \\ \Phi_{ac}(-\ell) = -K\sigma[A \cosh(\sigma \ell) - B \sinh(\sigma \ell)] \end{cases}$$

It is possible to write the relation between T and Φ at the front and rear surfaces in a matrix way, so that we obtain

$$\begin{pmatrix} T(0) \\ \Phi(0) \end{pmatrix} = \begin{pmatrix} \cosh(\sigma \ell) & -\frac{\sinh(\sigma \ell)}{K\sigma} \\ -K\sigma \sinh(\sigma \ell) & \cosh(\sigma \ell) \end{pmatrix} \begin{pmatrix} T(-\ell) \\ \Phi(-\ell) \end{pmatrix} \Leftrightarrow \begin{pmatrix} T(0) \\ \Phi(0) \end{pmatrix} = \begin{pmatrix} a & b \\ c & d \end{pmatrix} \begin{pmatrix} T(-\ell) \\ \Phi(-\ell) \end{pmatrix} \quad (2.49)$$

Thus, we have a matrix that represents the sheet, and moreover, given the incoming and outgoing fluxes (neglecting heat losses), the temperatures at the front and rear surfaces may be solved. For instance,

$$\left. \begin{matrix} \Phi(0) = -\frac{I_0}{2} \\ \Phi(-\ell) = 0 \end{matrix} \right\} \Rightarrow \begin{cases} T(0) = -\frac{I_0}{2} \frac{a}{c} = \frac{I_0}{2} \frac{\cosh(\sigma \ell)}{K\sigma \sinh(\sigma \ell)} \\ T(-\ell) = -\frac{I_0}{2} \frac{1}{c} = \frac{I_0}{2} \frac{1}{K\sigma \sinh(\sigma \ell)} \end{cases}$$

which agree with equation (2.25) for $z=0$ and $z=-\ell$, respectively.

Furthermore, it is also possible to consider heat losses by convection and radiation with this method in a simple way. As we did before for the sheet (Figure 2.12, right), we add the heat losses to the boundary conditions, this is, to the fluxes:

$$\begin{cases} \Phi(0) = -\frac{I_0}{2} + h_1 T(0) \\ \Phi(-\ell) = -h_2 T(-\ell) \end{cases}$$

where h_1 and h_2 stand for the combined coefficient for convection and radiation losses h , considering different possible values at the front or the rear surface, respectively. Hence, the matrix system results

$$\begin{pmatrix} T(0) \\ -\frac{I_0}{2} \end{pmatrix} = \begin{pmatrix} 1 & 0 \\ -h_1 & 1 \end{pmatrix} \begin{pmatrix} a & b \\ c & d \end{pmatrix} \begin{pmatrix} 1 & 0 \\ -h_2 & 1 \end{pmatrix} \begin{pmatrix} T(-\ell) \\ 0 \end{pmatrix} \quad (2.50)$$

from which front and rear surface temperatures may be easily solved. It is worth noting that the effect of heat losses is incorporated in a compact way as extra matrixes added on the left (right) of the main matrix representing the sheet for front (rear) surface heat losses.

In addition to this, the thermal quadrupole method is a powerful tool to consider also other effects, such as thermal resistance between layers, which accounts for the lack of adherence between consecutive sheets, in an easy way.

Let us consider a system of two layers, of diffusivities D_1 , D_2 and conductivities K_1 , K_2 , as it is schemed in Figure 2.16.

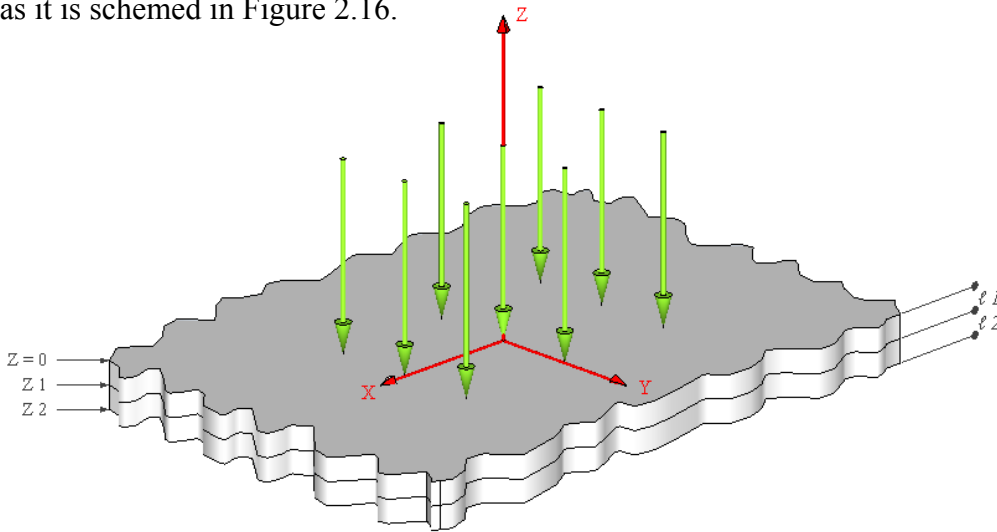


Figure 2.16: System of two layers of thickness ℓ_1 and ℓ_2 , illuminated by a plane light beam.

From equation (2.49) we know the model of each separate sheet is:

$$\begin{aligned} \begin{pmatrix} T_1(0) \\ \Phi_1(0) \end{pmatrix} &= \begin{pmatrix} a_1 & b_1 \\ c_1 & d_1 \end{pmatrix} \begin{pmatrix} T_1(-z_1) \\ \Phi_1(-z_1) \end{pmatrix} \\ &\vdots \\ \begin{pmatrix} T_2(-z_1) \\ \Phi_2(-z_1) \end{pmatrix} &= \begin{pmatrix} a_2 & b_2 \\ c_2 & d_2 \end{pmatrix} \begin{pmatrix} T_2(-z_2) \\ \Phi_2(-z_2) \end{pmatrix} \end{aligned} \quad (2.51)$$

If the system exhibits a perfect adherence between the layers, then we have temperature and flux continuity at the contact surface z_1

$$\begin{pmatrix} T_1(-z_1) \\ \Phi_1(-z_1) \end{pmatrix} = \begin{pmatrix} T_2(-z_1) \\ \Phi_2(-z_1) \end{pmatrix}$$

so from (2.51) we conclude the model for the system of two layers results

$$\begin{pmatrix} T_1(0) \\ \Phi_1(0) \end{pmatrix} = \begin{pmatrix} a_1 & b_1 \\ c_1 & d_1 \end{pmatrix} \begin{pmatrix} a_2 & b_2 \\ c_2 & d_2 \end{pmatrix} \begin{pmatrix} T_2(-z_2) \\ \Phi_2(-z_2) \end{pmatrix} \quad (2.52)$$

On the other hand, if there is a thermal resistance (R) at the contact surface, the system will show a discontinuity in the temperature:

$$T_1(-z_1) - T_2(-z_1) = -R\Phi_2(-z_1)$$

so that

$$\begin{pmatrix} T_1(-z_1) \\ \Phi_1(-z_1) \end{pmatrix} = \begin{pmatrix} 1 & -R \\ 0 & 1 \end{pmatrix} \begin{pmatrix} T_2(-z_1) \\ \Phi_2(-z_1) \end{pmatrix}$$

Thus, the system (2.51) will become

$$\begin{pmatrix} T_1(0) \\ \Phi_1(0) \end{pmatrix} = \begin{pmatrix} a_1 & b_1 \\ c_1 & d_1 \end{pmatrix} \begin{pmatrix} 1 & -R \\ 0 & 1 \end{pmatrix} \begin{pmatrix} a_2 & b_2 \\ c_2 & d_2 \end{pmatrix} \begin{pmatrix} T_2(-z_2) \\ \Phi_2(-z_2) \end{pmatrix} \quad (2.53)$$

where again the contribution of the thermal resistance is easily incorporated as an extra matrix between the two matrixes representing the layers in contact.

As we may see, in the thermal quadrupole method, each contribution is represented by an independent matrix added or not to the basic system for a single adiabatic sheet. As an example, the model for a system consisting of two layers with a thermal resistance in between and with heat losses at both front and rear surfaces will be

$$\begin{pmatrix} T_1(0) \\ -\frac{I_0}{2} \end{pmatrix} = \begin{pmatrix} 1 & 0 \\ -h_1 & 1 \end{pmatrix} \begin{pmatrix} a_1 & b_1 \\ c_1 & d_1 \end{pmatrix} \begin{pmatrix} 1 & -R \\ 0 & 1 \end{pmatrix} \begin{pmatrix} a_2 & b_2 \\ c_2 & d_2 \end{pmatrix} \begin{pmatrix} 1 & 0 \\ -h_2 & 1 \end{pmatrix} \begin{pmatrix} T_2(-z_2) \\ 0 \end{pmatrix}$$

where the temperatures of the front and rear surfaces are easily solved.

Generalizing the method for a system of N layers of thickness ℓ_i (Figure 2.17), with neither heat losses nor thermal resistances we obtain

$$\begin{pmatrix} T(0) \\ \Phi(0) \end{pmatrix} = \begin{pmatrix} a_1 & b_1 \\ c_1 & d_1 \end{pmatrix} \begin{pmatrix} T(-z_1) \\ \Phi(-z_1) \end{pmatrix}$$

$$\vdots$$

$$\begin{pmatrix} T(-z_1) \\ \Phi(-z_1) \end{pmatrix} = \begin{pmatrix} a_2 & b_2 \\ c_2 & d_2 \end{pmatrix} \begin{pmatrix} T(-z_2) \\ \Phi(-z_2) \end{pmatrix}$$

$$\vdots \dots\dots\dots$$

$$\vdots$$

$$\begin{pmatrix} T(-z_{N-1}) \\ \Phi(-z_{N-1}) \end{pmatrix} = \begin{pmatrix} a_N & b_N \\ c_N & d_N \end{pmatrix} \begin{pmatrix} T(-z_N) \\ \Phi(-z_N) \end{pmatrix}$$

which expressed in a compact way is

$$\begin{pmatrix} T(0) \\ \Phi(0) \end{pmatrix} = \begin{pmatrix} A & B \\ C & D \end{pmatrix} \begin{pmatrix} T(-z_N) \\ \Phi(-z_N) \end{pmatrix} \tag{2.54}$$

where $\begin{pmatrix} A & B \\ C & D \end{pmatrix} = \prod_{i=1}^{i=N} \begin{pmatrix} a_i & b_i \\ c_i & d_i \end{pmatrix}$ with $\begin{pmatrix} a_i & b_i \\ c_i & d_i \end{pmatrix} = \begin{pmatrix} \cosh(\sigma_i \ell_i) & -\frac{\sinh(\sigma_i \ell_i)}{K_i \sigma_i} \\ -K_i \sigma_i \sinh(\sigma_i \ell_i) & \cosh(\sigma_i \ell_i) \end{pmatrix}$

the matrix for each layer.

In case of extra contributions to this system, the corresponding matrices should be added in the correct place following the procedure explained above.

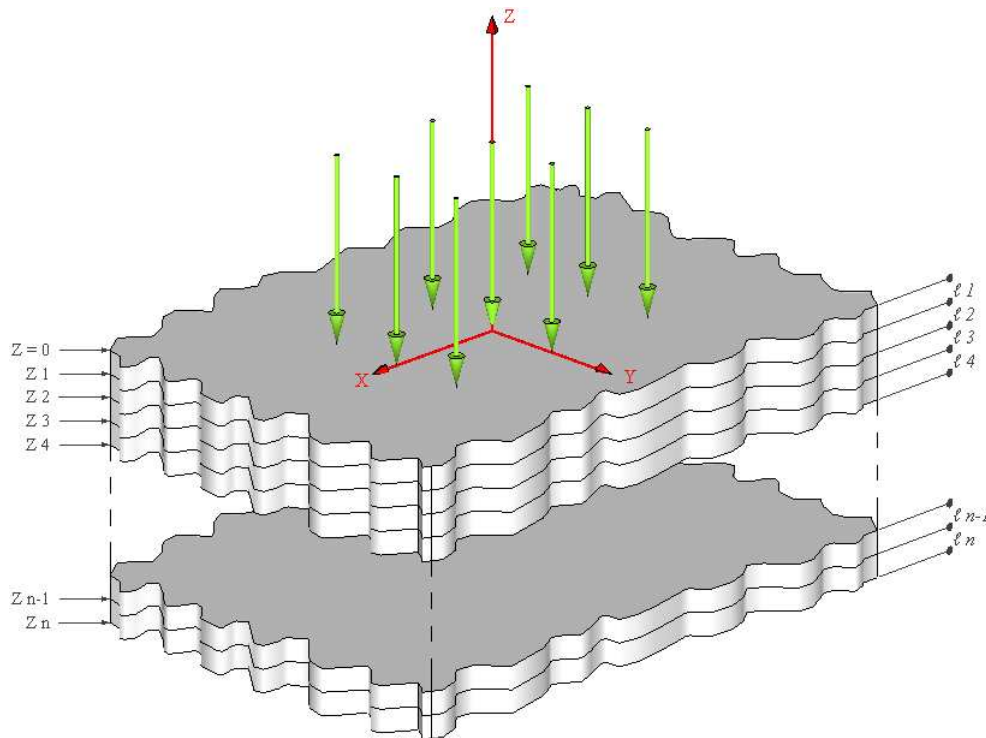


Figure 2.17: System of N layers of thickness ℓ_i , illuminated by a plane light beam.

This matrix method reviewed for plane illumination works also for a focused beam, applying the changes summarized in Table 2.1. Hence, the model for a sheet is

$$\begin{pmatrix} \bar{T}(\delta, 0) \\ \bar{\Phi}(\delta, 0) \end{pmatrix} = \begin{pmatrix} \cosh(\beta \ell) & -\frac{\sinh(\beta \ell)}{K\beta} \\ -K\beta \sinh(\beta \ell) & \cosh(\beta \ell) \end{pmatrix} \begin{pmatrix} \bar{T}(\delta, -\ell) \\ \bar{\Phi}(\delta, -\ell) \end{pmatrix} \quad (2.55)$$

where temperatures and fluxes are worked in the Hankel space. Once one solves the Hankel transform of the temperatures for the front and rear surfaces, the temperatures are obtained by applying the inverse transform, as equation (2.19) states. Regarding extra effects, the matrixes are added in the same way as for plane illumination.

3. Thin films and filaments thermal diffusivity measurements

3.1. Introduction

Now, the method reviewed in Chapter 2 to measure thermal properties by infrared lock-in thermography is applied to the extreme case of thin films and filaments. Point-like illumination is used to study, through the surface temperature map, the heat propagation along the surface, and therefore, the in-plane thermal properties, with special attention paid to thermal diffusivity.

Infrared Thermography (IRT) requires dealing with several issues concerning the data taking. It is well known that diffraction effects of the infrared radiation when it passes through the lens of the recording camera affect the readings of the surface temperature. At high frequencies this affects the measurements increasing the slopes, and so the resulting diffusivity becomes overestimated [37-41]. At low frequencies, however, there is no evidence of such effect on the slopes, but one has to deal with heat losses in return. Figure 3.1 shows experimental diffusivity values for a 150 μm diameter PEEK (polyeter-eter-ketone) filament in air as a function of the modulation frequency. The diffusivity values are obtained from the slopes of the surface temperature amplitude (squares) and phase (circles), and from the product of both

(solid symbols) in order to cancel the heat losses effect. As expected, we observe increasing diffusivity values above 10 Hz, due to diffraction. Below, but for amplitude and phase deviations at low frequencies accounting for heat losses, the diffusivity value out of the product of both remains constant at $0.80 \text{ mm}^2/\text{s}$. Nevertheless, this obtained value is significantly higher than the expected value found in literature, $0.19 \text{ mm}^2/\text{s}$ [42] (plotted in red), which is indeed the typical diffusivity of polymers.

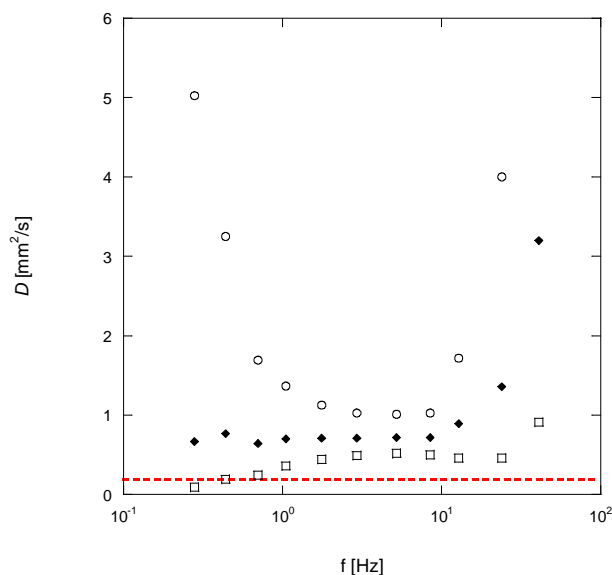


Figure 3.1: Diffusivity values for a $150 \mu\text{m}$ diameter PEEK filament measured in air as a function of the modulation frequency. Diffusivities are obtained from the amplitude (squares) and phase (circles) of the surface temperature, and the product of both (solid symbols). The expected diffusivity value is shown in red.

Similarly, measurements on thinner samples of this material show higher values than expected, reaching even $1.2 \text{ mm}^2/\text{s}$ for a $34 \mu\text{m}$ filament.

Concerning the high frequency limit, it is possible to consider the diffraction effects and fit the measurements to a diffraction corrected non-linear model [37, 38, 40, 41], but our target focuses on the thermal properties retrieval only by linear methods. So as to fulfil our purpose, we avoid the problematic frequency range and limit

ourselves to the low frequency range. But, as we saw in the previous chapter, this is the range where heat losses become significant, so it forces us to work under the model reviewed in section 2.4 and apply the equation (2.46) to cancel the effect of heat losses by convection and radiation in order to retrieve the correct thermal diffusivity. However, although the model gives good results for thermal diffusivity measurements on thick and high conductivity materials [9-13], results on Figure 3.1 and some examples of thin low diffusivity samples found in literature [11, 12, 43] clearly show that the model does not explain the experimental results.

With the aim of identifying the mechanism responsible for this overestimation on thin low diffusivity samples, we introduced a traditionally neglected term, heat losses by conduction to the gas.

3.2. Theoretical model

Now a model is developed adding the contribution of the previously neglected heat conduction to the gas to the model reviewed in Chapter 2, which already considered heat losses by convection and radiation. Then, the effect of this new contribution on thin films and filaments is studied and the method to overcome the overestimation when retrieving diffusivity values of thin poor conducting materials is proposed.

3.2.1. Films

A. Isotropic film

We work now on a theoretical model for an isotropic sheet of thickness ℓ , surrounded by air, as in Figure 2.12, illuminated by a modulated focused light beam.

In order to resolve the temperature field, we proceed as in Chapter 2, by resolving the homogeneous Helmholtz equation and adding the heat losses to the boundary

conditions. However, since this time we include the contribution of heat conduction to the gas, we must consider also the equations for the gas at the front ($g1$) and back ($g2$) of the sample (s), which will correspond to outgoing thermal waves. Hence, the equations are

$$T_{g1}(r, z) = \int_0^{\infty} [Ae^{-\beta_g z}] J_o(\delta r) \delta d\delta$$

$$T_s(r, z) = \int_0^{\infty} [Be^{\beta_s z} + Ce^{-\beta_s z}] J_o(\delta r) \delta d\delta$$

$$T_{g2}(r, z) = \int_0^{\infty} [De^{\beta_g z}] J_o(\delta r) \delta d\delta$$

Concerning the boundary conditions, temperature and heat flux continuity at the sample front and back surfaces are required:

$$T_{g1}(z = 0) = T_s(z = 0)$$

$$T_{g2}(z = -\ell) = T_s(z = -\ell)$$

$$K_s \left. \frac{\partial T_s}{\partial z} \right|_{z=0} = \frac{P_o}{4\pi} \int_0^{\infty} e^{-(\delta a)^2/8} J_o(\delta r) \delta d\delta - h T_s \Big|_{z=0} - K_g \left. \frac{\partial T_{g1}}{\partial z} \right|_{z=0}$$

$$K_s \left. \frac{\partial T_s}{\partial z} \right|_{z=-\ell} = h T_s \Big|_{z=-\ell} + K_g \left. \frac{\partial T_{g2}}{\partial z} \right|_{z=-\ell}$$

By resolving the system, we obtain the temperature field for a sheet:

$$T_s(r, z) = \frac{P_o}{4\pi K_s} \int_0^{\infty} \frac{e^{-(\delta a)^2/8}}{\beta_s} \frac{(1 + G + H)e^{\beta_s \ell} e^{\beta_s z} + (1 - G - H)e^{-\beta_s \ell} e^{-\beta_s z}}{(1 + G + H)^2 e^{\beta_s \ell} - (1 - G - H)^2 e^{-\beta_s \ell}} J_o(\delta r) \delta d\delta \quad (3.1)$$

where $H = h / K_s \beta_s$ and $G = K_g \beta_g / K_s \beta_s$ are the terms accounting for heat losses by the combined convection and radiation, and conduction to the gas, respectively. It is worth noting that the effect of the different contributions to the heat losses can be easily considered or neglected, as they are independent of each other.

As it is the aim of the chapter to study thin films, we particularize, as in the previous chapter, the sheet temperature field (3.1) to the case of a thermally thin film. Next, we study a thermally thick sheet as well, in order to compare the effect of heat losses on thermal diffusivity measurements for both extreme cases.

i) Thermally thin film

Let us approximate the sheet temperature field (3.1) to a thermally thin film temperature by applying the appropriate approximation (2.27). Thus, the temperature field becomes:

$$T_{thin}(r) \approx \frac{P_o}{4\pi K_s} \int_0^\infty \frac{e^{-(\alpha x)^2/8}}{\beta_s} \frac{1}{2G + 2H + \beta_s \ell} J_o(\delta r) \delta d\delta \quad (3.2)$$

It is easy to check that if we neglect heat conduction to the gas ($G=0$), the previously reviewed equation (2.43) is obtained, as expected.

Figure 3.2 shows the surface temperature simulation for a thin film (3.2), where the different contributions to the heat losses are depicted separately. For this thin low diffusivity film, the phase and the natural logarithm of the amplitude multiplied by the square root of the distance are represented as a function of the distance to the heating spot. According to the graph, under adiabatic conditions (black lines) amplitude and phase are straight parallel lines, as expected. Besides, regarding the convection and radiation effect (red lines), although it changes the slopes, it preserves the linearity and still, it is possible to retrieve the diffusivity, as reviewed in equation (2.46). However, when dealing with heat losses by all the three mechanisms (blue lines), the conduction to the gas introduces such an effect that not only the slopes are changed, but also even the linearity is lost, preventing, then, from obtaining diffusivity values by means of linear methods.

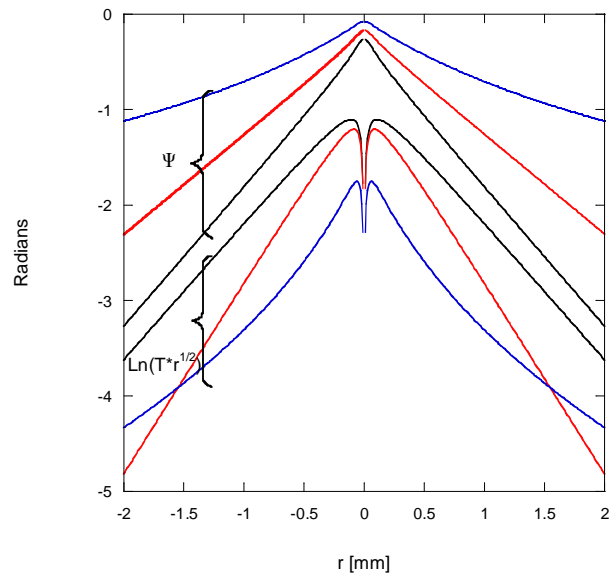


Figure 3.2: Surface temperature simulation as a function of the distance to the heating spot for a 25 μm thick film ($D = 0.15 \cdot 10^{-6} \text{ m}^2/\text{s}$, $K = 0.2 \text{ W/mK}$) at a modulation frequency $f = 0.1 \text{ Hz}$. Different situations are represented: without heat losses (black lines), with convection and radiation losses ($h = 15$) (red lines) and with heat losses by the three mechanisms (blue lines).

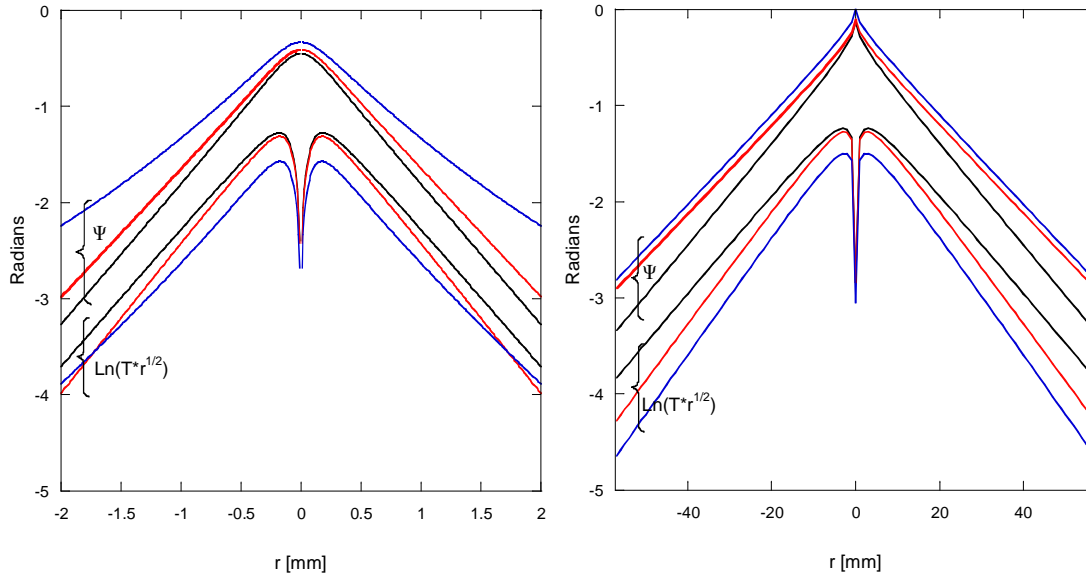


Figure 3.3: Surface temperature simulations as a function of the distance to the heating spot for: on the left, 200 μm thick film ($D = 0.15 \cdot 10^{-6} \text{ m}^2/\text{s}$, $K = 0.2 \text{ W/mK}$) at $f = 0.1 \text{ Hz}$; on the right, 25 μm thick film ($D = 116 \cdot 10^{-6} \text{ m}^2/\text{s}$, $K = 400 \text{ W/mK}$) at $f = 0.1 \text{ Hz}$. Different situations are represented: without heat losses (black lines), with convection and radiation losses ($h = 15$) (red lines) and with heat losses by the three mechanisms (blue lines).

It becomes also worth noting that, for a given h coefficient, the effect of heat losses is bigger on thin low conductivity samples. In Figure 3.3 we may observe the effect of heat losses on different sample thicknesses and conductivities. On the left, we show results for an eight times thicker sample, where we see that the effect is significantly smaller. On the right, in the same way, a much higher conductivity sample presents also a small effect of heat losses. However, it is worth mentioning that in neither of the cases the effect is fully negligible.

ii) Thermally thick film

By applying this time the thermally thick approximation (2.28), temperature for a thick sheet is obtained:

$$T_{thick}(r, z = 0) \approx \frac{P_o}{4\pi K_s} \int_0^\infty \frac{e^{-(\delta r)^2/8}}{\beta_s} \frac{1}{(1+G+H)} J_o(\delta r) \delta d\delta \quad (3.3)$$

If we represent the different contributions to the heat losses for a thick sample, Figure 3.4, we may observe that, as it was the case for convection and radiation heat losses, for conduction to the gas losses the effect is also hardly noticeable. Only for this extreme example depicted, for a very low diffusivity sample, at a very low modulation frequency and with an excessive h coefficient, we get to perceive the deviation of the curves.

Therefore, we might clearly state that the effect of heat losses by conduction to the gas is by no means negligible, as it was traditionally considered, when dealing with thin films of low diffusivity. Still, it is possible to ignore it for thick samples, where even convection and radiation losses effect is small and, anyway, non-cancellable by the slopes method.

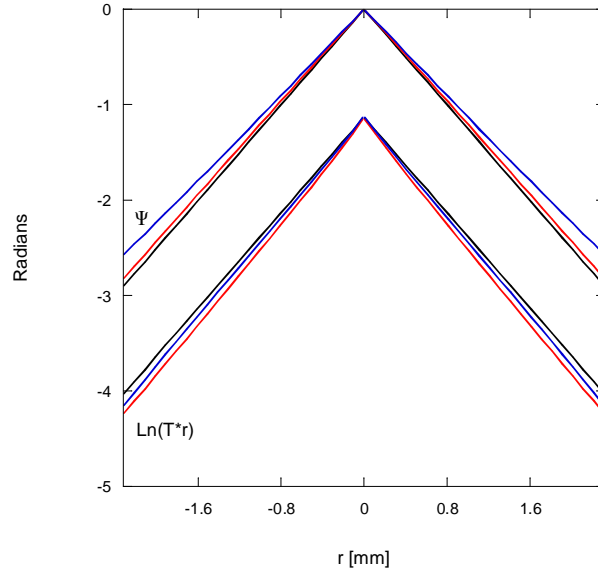


Figure 3.4: Surface ($z=0$) temperature simulation as a function of the distance to the heating spot for a thermally thick sheet ($D = 0.10 \cdot 10^{-6} \text{ m}^2/\text{s}$, $K = 0.3 \text{ W/mK}$) at a modulation frequency $f = 0.05 \text{ Hz}$, calculated without heat losses (black lines), with convection and radiation losses ($h=50$) (red lines) and with heat losses by the three mechanisms (blue lines).

B. Anisotropic film

Now we consider the same sheet as in the previous subsection, but with a thermal conductivity varying with the direction. Let the axes (x, y, z) in Figure 2.9 Right be the principal axes of the anisotropic sample with the corresponding principal thermal conductivities (K_x, K_y, K_z) and thermal diffusivities (D_x, D_y, D_z).

Due to the lack of cylindrical symmetry the ac component of the temperature can be expressed in the Fourier space as [44, 45]

$$T(x, y, z) = \int_{-\infty}^{\infty} \int_{-\infty}^{\infty} e^{-i(x\lambda + y\eta)} [A' e^{\gamma z} + B' e^{-\gamma z}] d\lambda d\eta \quad (3.4)$$

where λ and η are the Fourier variables, and $\gamma^2 = (D_x \lambda^2 + D_y \eta^2 + i\omega) / D_z$.

A' and B' are constants to be determined from the heat flux continuity at the sample surfaces:

$$K_z \frac{\partial T}{\partial z} \Big|_{z=0} + hT \Big|_{z=0} = \frac{P_o}{2\pi} \int_{-\infty}^{\infty} \int_{-\infty}^{\infty} e^{-i(x\lambda+y\eta)} e^{-(\lambda^2+\eta^2)a^2/8} d\lambda d\eta$$

$$K_z \frac{\partial T}{\partial z} \Big|_{z=-\ell} - hT \Big|_{z=-\ell} = 0$$

where the second term in the first condition is the Fourier transform of the heating power distribution. Therefore, the sample temperature is obtained

$$T(x, y, z) = \frac{P_o}{4\pi K_z} \int_{-\infty}^{\infty} \int_{-\infty}^{\infty} e^{-i(x\lambda+y\eta)} \frac{e^{-(\lambda^2+\eta^2)a^2/8}}{\gamma} \cdot \left[\frac{(1+H')e^{\gamma} e^{\gamma z} + (1-H')e^{-\gamma} e^{-\gamma z}}{(1+H')(1+H')e^{\gamma} - (1-H')(1-H')e^{-\gamma}} \right] d\lambda d\eta \quad (3.5)$$

where $H' = h / K_z \gamma$.

Now we analyze the two extreme cases of practical interest.

i) *Thermally thin film.*

If the sheet is thermally thin ($\ell \ll \mu_z = \sqrt{D_z / \pi f}$) equation (3.5) reduces to

$$T(x, y)_{thin} = \frac{P_o}{4\pi \rho c \ell} \int_{-\infty}^{\infty} \int_{-\infty}^{\infty} e^{-i(x\lambda+y\eta)} \frac{e^{-(\lambda^2+\eta^2)a^2/8}}{D_x \lambda^2 + D_y \eta^2 + i\omega + \frac{2h}{\rho c \ell}} d\lambda d\eta \quad (3.6)$$

where $\rho c = K_x/D_x = K_y/D_y = K_z/D_z$ is the heat capacity. Note that the temperature does not depend on K_z or D_z .

For a highly focused laser beam ($a = 0$) equation (3.6) has analytical solution for the temperature along the principal axes

$$T_x(x, a = 0)_{thin} = \frac{P_o}{2\rho c \ell} \frac{1}{\sqrt{D_x D_y}} K_o(\sigma'_x x)$$

$$T_y(y, a = 0)_{thin} = \frac{P_o}{2\rho c \ell} \frac{1}{\sqrt{D_x D_y}} K_o(\sigma'_y y)$$

where $\sigma'_{x,y} = \frac{i\omega}{D_{x,y}} + \frac{2h}{K_{x,y}\ell}$, and by using the asymptotic approach for large x and y values [33], they reduce to:

$$T_x(x \rightarrow \infty, a = 0)_{thin} \approx \frac{P_o}{2\rho c \ell} \frac{1}{\sqrt{D_x D_y}} \sqrt{\frac{\pi}{2\sigma'_x}} \frac{e^{-\sigma'_x x}}{\sqrt{x}} \quad (3.7a)$$

$$T_y(y \rightarrow \infty, a = 0)_{thin} \approx \frac{P_o}{2\rho c \ell} \frac{1}{\sqrt{D_x D_y}} \sqrt{\frac{\pi}{2\sigma'_y}} \frac{e^{-\sigma'_y y}}{\sqrt{y}} \quad (3.7b)$$

As it was the case with the isotropic thin sheet, the phase and the natural logarithm of the temperature amplitude multiplied by \sqrt{x} or \sqrt{y} have a linear dependence on the distance in such a way that the product of the slopes is equal to $-\pi f/D_x$ or $-\pi f/D_y$, indicating that it is independent of heat losses. Accordingly, the thermal diffusivity along the principal axes can be obtained. Note that the analytical solution has been found only for the principal axes, so that only the diffusivity along that axes can be retrieved.

ii) *Thermally thick film.*

If the material is thermally thick ($\ell \gg \mu_z = \sqrt{D_z/\pi f}$) the temperature of the illuminated surface is given by

$$T(x, y, z = 0)_{thick} = \frac{P_o}{4\pi K_z} \int_{-\infty}^{\infty} \int_{-\infty}^{\infty} e^{-i(x\lambda + y\eta)} \frac{e^{-(\lambda^2 + \eta^2)a^2/8}}{\gamma + \frac{h}{K_z}} d\lambda d\eta \quad (3.8)$$

Numerical simulations of equation (3.8) indicate that in the absence of heat losses, the natural logarithm of the temperature amplitude multiplied by x or y and the phase have a linear dependence on the distance with the same slope $-\sqrt{\pi f / D_x}$ or $-\sqrt{\pi f / D_y}$. For non-negligible heat losses, both slopes are modified in such a way that their product is not independent of heat losses. Anyway, as in the case of isotropic samples, the effect of heat losses in thick samples is almost negligible.

3.2.2. Filaments

A. Monofilament

We study now the thermal diffusivity measurement of filaments. We extend the theoretical model proposed by Barkyoub and Land [46] to include heat losses by the three mechanisms: convection, radiation and conduction to the gas.

We illuminate the samples with a modulated (frequency f) line focused beam (Figure 3.5) and, as for sheets, we consider filaments as isotropic, opaque and infinitely long samples.

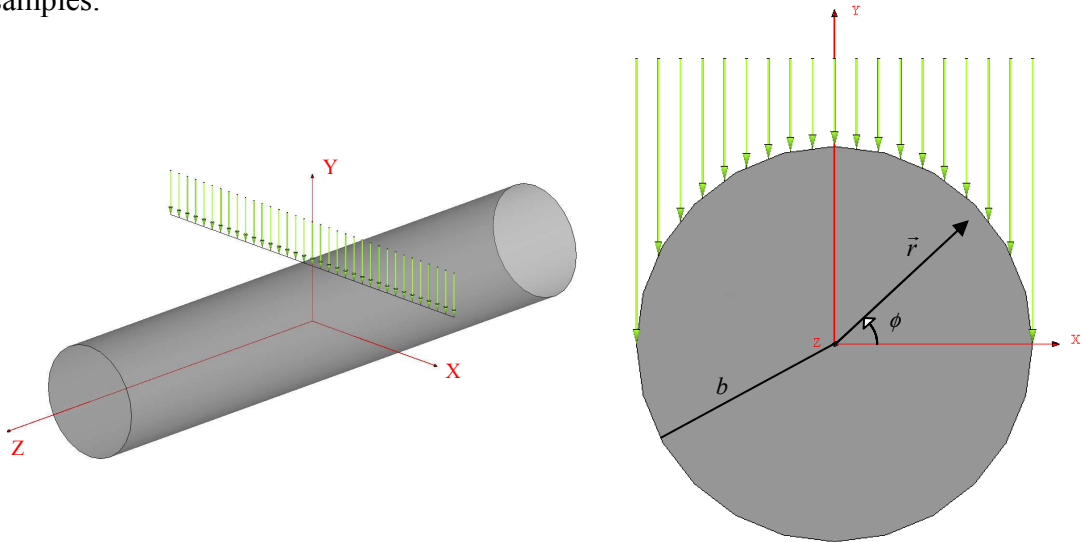


Figure 3.5: Line beam illuminating a filament (left). Cross section of the filament (right).

The laser linear power density is P_0 (W/m) with a Gaussian profile of radius a (at $1/e^2$), so that the incoming flux at the sample surface is:

$$Q(\vec{r}) = \sqrt{\frac{2}{\pi}} \frac{P_0}{2a} e^{-2z^2/a^2} \cdot \begin{cases} \sin \phi & , \phi \in [0, \pi] \\ 0 & , \phi \in [\pi, 2\pi] \end{cases} \quad (3.9)$$

In order to obtain the filament temperature field, we resolve the Helmholtz equation (2.11) in cylindrical coordinates, $T_{ac}(\vec{r}) = T_{ac}(r, z, \phi)$, for both the sample ($i=s$) and the gas ($i=g$):

$$\frac{\partial^2 T_i}{\partial r^2} + \frac{1}{r} \frac{\partial T_i}{\partial r} + \frac{1}{r^2} \frac{\partial^2 T_i}{\partial \phi^2} + \frac{\partial^2 T_i}{\partial z^2} - \sigma_i^2 T_i = 0 \quad (3.10)$$

We can solve equation (3.10) working in the Fourier space, where

$$T(r, z, \phi) = \int_{-\infty}^{\infty} e^{i\lambda z} t(r, \lambda, \phi) d\lambda \quad (3.11)$$

with λ as the Fourier variable.

Accordingly, the Helmholtz equation in terms of the temperature Fourier transform is:

$$\frac{\partial^2 t_i}{\partial r^2} + \frac{1}{r} \frac{\partial t_i}{\partial r} + \frac{1}{r^2} \frac{\partial^2 t_i}{\partial \phi^2} - \delta_i^2 t_i = 0, \text{ where } \delta_i^2 = \sigma_i^2 + \lambda^2 \quad (3.12)$$

By using the separation of variables method, i.e. $t(r, \lambda, \phi) = R(r, \lambda)\Phi(\phi)$, equation (3.12) reduces to the following two equations:

$$\begin{cases} r^2 \frac{d^2 R_i}{dr^2} + r \frac{dR_i}{dr} - (\delta_i^2 r^2 + n^2) R = 0 \\ \frac{d^2 \Phi_i}{d\phi^2} + n^2 \Phi_i = 0 \end{cases} \quad (3.13a,b)$$

Equation (3.13a) is the modified Bessel's differential equation, whose solutions are the modified Bessel functions [33] $I_n(\delta_i r)$ and $K_n(\delta_i r)$. On the other hand, the solution of equation (3.13b) is the exponential function $e^{in\phi}$, with $n \in Z$. Therefore, temperature fields for the gas and the sample are:

$$T_g(r, z, \phi) = \int_{-\infty}^{\infty} e^{i\lambda z} \left(\sum_{n=-\infty}^{\infty} A_n K_n(\delta_g r) e^{in\phi} \right) d\lambda \quad (3.14)$$

$$T_s(r, z, \phi) = \int_{-\infty}^{\infty} e^{i\lambda z} \left(\sum_{n=-\infty}^{\infty} B_n I_n(\delta_s r) e^{in\phi} \right) d\lambda \quad (3.15)$$

where only solutions with a physical meaning have been considered. A_n and B_n are again constants to be determined by the boundary conditions.

All heat losses considered, temperature and heat flux continuity at the filament surface ($r = b$) write:

$$T_g(r = b) = T_s(r = b)$$

$$K_s \frac{\partial T_s}{\partial r} \Big|_{r=b} - K_g \frac{\partial T_g}{\partial r} \Big|_{r=b} + h T_s \Big|_{r=b} = \begin{cases} \sqrt{\frac{2}{\pi}} \frac{P_o}{2a} e^{-2z^2/a^2} \sin \phi & , \phi \in [0, \pi] \\ 0 & , \phi \in [\pi, 2\pi] \end{cases}$$

So as to solve it, we apply the Fourier transform to the beam flux and the Fourier expansion to the angular component:

$$f(\phi) = \begin{cases} \sin \phi & , \phi \in [0, \pi] \\ 0 & , \phi \in [\pi, 2\pi] \end{cases} = \sum_{n=-\infty}^{\infty} \frac{(-i)^n \cos(n\pi/2)}{\pi(1-n^2)} e^{in\phi}$$

As a result, we obtain the temperature fields for the gas and the sample:

$$T_g(r, z, \phi) = \int_{-\infty}^{\infty} e^{i\lambda z} \frac{P_o}{4\pi K_s \delta_s} \cdot \left(\sum_{n=-\infty}^{\infty} \frac{\frac{(-i)^n \cos(n\pi/2)}{\pi(1-n^2)} e^{-\lambda^2 a^2/8} I_n(\delta_s b)}{K_n(\delta_g b) I'_n(\delta_s b) - G K'_n(\delta_g b) I_n(\delta_s b) + H K_n(\delta_g b) I_n(\delta_s b)} K_n(\delta_g r) e^{in\phi} \right) d\lambda \quad (3.16a)$$

$$T_s(r, z, \phi) = \int_{-\infty}^{\infty} e^{i\lambda z} \frac{P_o}{4\pi K_s \delta_s} \cdot \left(\sum_{n=-\infty}^{\infty} \frac{\frac{(-i)^n \cos(n\pi/2)}{\pi(1-n^2)} e^{-\lambda^2 a^2/8} K_n(\delta_g b)}{K_n(\delta_g b) I'_n(\delta_s b) - G K'_n(\delta_g b) I_n(\delta_s b) + H K_n(\delta_g b) I_n(\delta_s b)} I_n(\delta_s r) e^{in\phi} \right) d\lambda \quad (3.16b)$$

where I'_n and K'_n are the derivatives of the modified Bessel functions I_n and K_n , respectively. It is worth mentioning that, as we found for sheets (3.1), the heat losses different mechanisms, G and H , contribute independently to the temperature field, so that they may be considered or not according to requirements.

Since infrared thermography deals with surface temperature maps, let us particularize the filament temperature field (3.16b) to the surface ($r = b$) temperature of the filament:

$$T_s(b, z, \phi) = \int_{-\infty}^{\infty} e^{i\lambda z} \frac{P_o e^{-\lambda^2 a^2/8}}{4\pi K_s \delta_s} \left(\sum_{n=-\infty}^{\infty} \frac{\frac{(-i)^n \cos(n\pi/2)}{\pi(1-n^2)} e^{in\phi}}{\frac{I'_n(\delta_s b)}{I_n(\delta_s b)} - G \frac{K'_n(\delta_g b)}{K_n(\delta_g b)} + H} \right) d\lambda \quad (3.17)$$

Besides, being thin samples the target of the research, we focus the study on thermally thin filaments, where the radius is much smaller than the thermal diffusion length, $b \ll \mu = \sqrt{D/\pi f}$. At this extreme case, only the term $n = 0$ contributes to the temperature. Hence, the approximations [33] below for small arguments of the Bessel functions and their derivatives may be applied:

$$I_o(z) \approx 1 \quad I'_o(z) \approx z/2 \quad K_o(z) \approx -Ln(z) \quad K'_o(z) \approx -1/z$$

Hence, the resulting temperature for thin filaments is:

$$\begin{aligned} T_s(b, z)_{thin} &\approx \int_{-\infty}^{\infty} e^{i\lambda z} \frac{P_o}{4\pi^2 K_s \delta_s} \frac{e^{-\lambda^2 a^2 / 8}}{\frac{I'_o(\delta_s b)}{I_o(\delta_s b)} - G \frac{K'_o(\delta_g b)}{K_o(\delta_g b)} + H} d\lambda \approx \\ &\approx \int_{-\infty}^{\infty} e^{i\lambda z} \frac{P_o}{4\pi^2 K_s \delta_s} \frac{e^{-\lambda^2 a^2 / 8}}{\frac{\delta_s b}{2} - G \frac{1}{\delta_g b Ln(\delta_g b)} + H} d\lambda \end{aligned} \quad (3.18)$$

which becomes independent of the angle ϕ .

Let us analyze now from equation (3.18) how thermal diffusivity might be retrieved from infrared thermography measurements, and moreover, how the different contributions to the heat losses affect the measurements for these thin filaments.

Considering firstly the adiabatic case, $G=0$ and $H=0$, together with an ideal focusing ($a = 0$) of the laser beam, the surface temperature becomes

$$\begin{aligned} T_s(b, z, a = 0) &\approx \frac{P_o}{2\pi^2 K_s b} \int_{-\infty}^{\infty} e^{i\lambda z} \frac{1}{\delta_s^2} d\lambda = \frac{P_o}{2\pi^2 K_s b} \int_{-\infty}^{\infty} e^{i\lambda z} \frac{1}{(\sigma_s^2 + \lambda^2)} d\lambda = \\ &= \frac{P_o}{2\pi K_s \sigma_s b} e^{-\sigma_s |z|} = \frac{P_o \sqrt{D}}{2\pi K_s b \sqrt{2\pi f}} e^{-\frac{\sqrt{\pi f}}{D} |z|} e^{-i(\frac{\sqrt{\pi f}}{D} |z| - \frac{\pi}{4})} \end{aligned} \quad (3.19)$$

which represents a plane thermal wave propagating along the z axis. It is easy to retrieve the thermal diffusivity value by means of the slopes method, as both the phase and the natural logarithm of the amplitude show a linear behaviour as a function of the distance to the heating spot, whose slopes are

$$m_\psi = -\sqrt{\pi f / D} = m_{\ln(T)} \quad (3.20)$$

which are the same as for sheets in the adiabatic case. We may see these parallel straight lines in black in Figure 3.6.

Regarding the case of heat losses by convection and radiation, $G=0$ and $H\neq 0$, and again considering ideal focusing of the laser beam ($a = 0$), we find

$$T_s(b, z, a = 0) \approx \frac{P_o}{2\pi K_s \sigma'_s b} e^{-\sigma'_s |z|}, \text{ where } \sigma'^2_s = \sigma_s^2 + \frac{2h}{K_s b} \quad (3.21)$$

Here, the phase and the natural logarithm of the amplitude still show a linear behaviour with the distance to the heating spot, but the slopes are no longer parallel as they are affected by heat losses by convection and radiation. However, as we reviewed for sheets (2.46), the independence of the product of slopes from heat losses holds,

$$m_{\ln(T)} \times m_\psi = -\pi f/D \quad (3.22)$$

so that the thermal diffusivity value retrieval by the slopes method is still possible. Figure 3.6 shows in red the straight lines corresponding to this case, where the slopes are clearly deviated from the adiabatic case (in black).

Concerning the real case of a filament with all the heat losses considered, $G\neq 0$ and $H\neq 0$, no simple equation has been found, so equation (3.18) is depicted. Figure 3.6 shows in blue lines the surface temperature of a thin filament as a function of the distance to the heating spot, including the conduction to the gas losses in addition to convection and radiation previously represented in red. We may clearly note the effect is so huge that even linearity is lost, as it happened for films, so it is not possible to retrieve the diffusivity by linear methods.

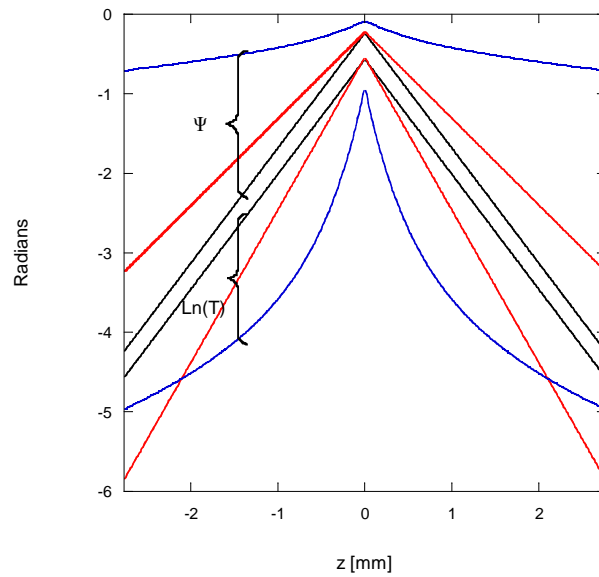


Figure 3.6: Surface temperature simulation as a function of the distance to the heating spot for a 60 μm diameter filament ($D = 0.15 \cdot 10^{-6} \text{ m}^2/\text{s}$, $K = 0.2 \text{ W/mK}$) at a modulation frequency $f = 0.1 \text{ Hz}$. Different situations are represented: without heat losses (black lines), with convection and radiation losses ($h = 15$) (red lines) and with heat losses by the three mechanisms (blue lines).

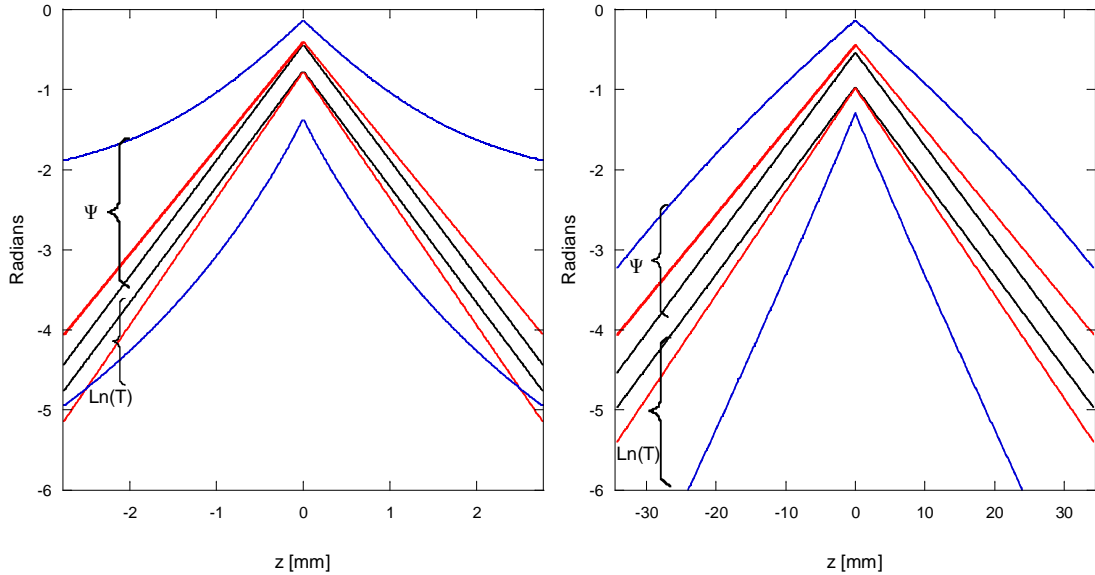


Figure 3.7: Surface temperature simulations as a function of the distance to the heating spot for: on the left, 200 μm diameter filament ($D = 0.15 \cdot 10^{-6} \text{ m}^2/\text{s}$, $K = 0.2 \text{ W/mK}$) at $f = 0.1 \text{ Hz}$; on the right, 60 μm diameter filament ($D = 23 \cdot 10^{-6} \text{ m}^2/\text{s}$, $K = 91 \text{ W/mK}$) at $f = 0.1 \text{ Hz}$. Different situations are represented: without heat losses (black lines), with convection and radiation losses ($h = 15$) (red lines) and with heat losses by the three mechanisms (blue lines).

Figure 3.7 shows, for the case of filaments, the same effect on the surface temperature of thickness and conductivity as for films in Figure 3.3. On the left, we observe the temperature for a thicker sample, where the effects are smaller but by no means negligible. On the right, a much higher conductivity filament temperature is simulated showing again a smaller effect. It is worth noting that blue lines do not seem to lose linearity in this case, but unfortunately the slopes changes do not compensate so as to cancel the heat losses effect and retrieve the right diffusivity.

B. Two-layer filament

We study now the case of a coated cylinder with an inner layer ($s1$) of radius b_1 and an outer layer ($s2$) of outer radius b_2 , as shown in Figure 3.8, surrounded by gas.

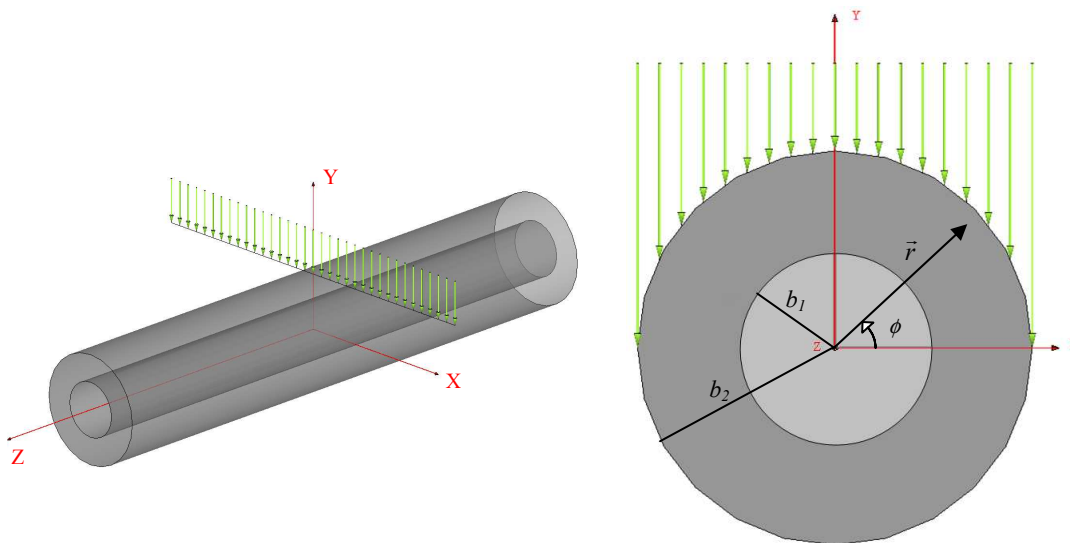


Figure 3.8: Line beam illuminating a two-layer filament (left). Cross section of the filament (right).

Temperatures in each layer and in the surrounding gas may be written as

$$T_g(r, z, \phi) = \int_{-\infty}^{\infty} e^{i\lambda z} \left(\sum_{n=-\infty}^{\infty} A_n K_n(\delta_g r) e^{in\phi} \right) d\lambda$$

$$T_2(r, z, \phi) = \int_{-\infty}^{\infty} e^{i\lambda z} \left(\sum_{n=-\infty}^{\infty} B_n I_n(\delta_2 r) e^{in\phi} + \sum_{n=-\infty}^{\infty} C_n K_n(\delta_2 r) e^{in\phi} \right) d\lambda$$

$$T_1(r, z, \phi) = \int_{-\infty}^{\infty} e^{i\lambda z} \left(\sum_{n=-\infty}^{\infty} D_n I_n(\delta_1 r) e^{in\phi} \right) d\lambda$$

where A_n , B_n , C_n and D_n are constants to be determined through the boundary conditions below:

$$T_g(r = b_2) = T_2(r = b_2)$$

$$T_1(r = b_1) = T_2(r = b_1)$$

$$K_2 \frac{\partial T_2}{\partial r} \Big|_{r=b_1} = K_1 \frac{\partial T_1}{\partial r} \Big|_{r=b_1}$$

$$K_2 \frac{\partial T_2}{\partial r} \Big|_{r=b_2} - K_g \frac{\partial T_g}{\partial r} \Big|_{r=b_2} + hT_g \Big|_{r=b_2} = \begin{cases} \sqrt{\frac{2}{\pi}} \frac{P_o}{2a} e^{-2z^2/a^2} \sin \phi & , \phi \in [0, \pi] \\ 0 & , \phi \in [\pi, 2\pi] \end{cases}$$

By tightly focusing the laser beam ($a=0$) on a thermally thin coated cylinder, and neglecting the conduction to the gas ($G=0$), the surface temperature becomes:

$$T_2(b_2, z) \approx \frac{P_o}{2\pi K_{\parallel} \sigma'_{\parallel} b_2} e^{-\sigma'_{\parallel} |z|} \quad (3.23)$$

where $\sigma'_{\parallel} = \frac{i\omega}{D_{\parallel}} + \frac{2h}{K_{\parallel} b_2}$, with $K_{\parallel} = K_1 v_1 + K_2 v_2$, $D_{\parallel} = \frac{K_{\parallel}}{(\rho c)_{eff}}$ and

$(\rho c)_{eff} = \frac{K_1}{D_1} v_1 + \frac{K_2}{D_2} v_2$. Here $v_1 = \frac{b_1^2}{b_2^2}$ and $v_2 = \frac{b_2^2 - b_1^2}{b_2^2}$ are the volume fraction of

layers 1 and 2 respectively.

By comparing equation (3.23) with equation (3.21) it can be concluded that the two-layer filament behaves as a monofilament with effective thermal conductivity ($K_{||}$) and thermal diffusivity ($D_{||}$), which follow the in-parallel thermal resistor model [47].

In the particular case of a thin tube whose inner core is empty, i.e. $K_1 = 0$, equation (3.23) reduces to

$$T_2(b_2, z) \approx \frac{P_o}{2\pi K_2 \sigma'_2 b'} e^{-\sigma'_2 |z|} \quad (3.24)$$

where $\sigma'_2 = \frac{i\omega}{D_2} + \frac{2h}{K_2 b'}$ and $b' = \frac{b_2^2 - b_1^2}{b_2}$.

If compared this expression above with equation (3.21), it can be stated that the surface temperature of a thin tube behaves as that of a solid one with the same thermal properties but an equivalent radius b' .

3.3. Experimental setup

This chapter deals with the thermal diffusivity measurement of thin films and filaments by means of point-like illumination. As the slopes method states, it is possible to retrieve lateral thermal diffusivity values from a surface temperature mapping at a fixed frequency of the modulated illumination. We have proved theoretically the dramatic influence of conductivity to the gas when working with thin low conductivity films and filaments, so that, performing the experiments in vacuum is proposed in order to avoid both conduction and convection losses. Thus, in this section our experimental set up needed for the accurate measurement of thin films and filaments thermal diffusivity is presented.

In Figure 3.9 a general scheme of the measuring set up is shown, from the thermal wave excitation in a sample, till the information recording and processing. As we may observe, the heating source is an acousto-optically modulated laser beam

focused onto the sample by a spherical or cylindrical lens. The samples are placed inside a vacuum chamber. After heating the sample, the thermal wave generated at the surface is propagated along the whole material, and infrared radiation is emitted. An infrared camera records that emitted infrared radiation, and the information, fed into a lock in module associated with the camera and connected to a PC, is demodulated to finally obtain the amplitude and phase of the oscillating component of the sample surface temperature.

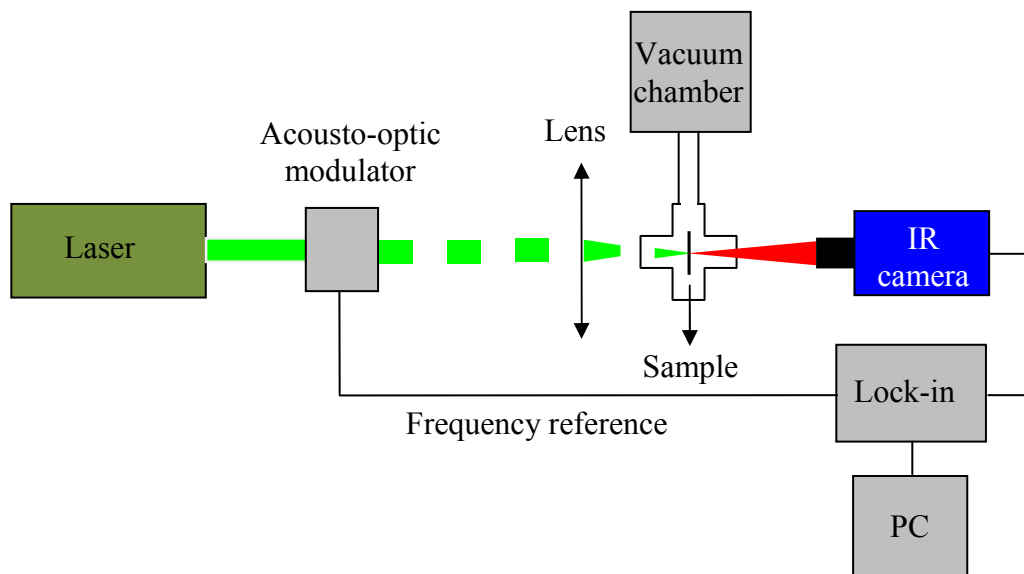


Figure 3.9: General scheme of the measuring set up.

In Figure 3.10 we can see a photo of the full set up in the laboratory, with all the components labelled and explained in detail below.

On the right, we find the heating source, a CW diode pumped doubled Nd:YAG laser COHERENT model Verdi 6 W (532 nm). The next element in the setup is the acousto-optic modulator (AOM), ISOMET 1201E-1. Vertically oriented to suit the polarization direction of the laser, it receives a square signal from a generator and a piezoelectric transducer transforms it into acoustic waves on the crystal inside, which diffract the laser beam and let us get a modulation at the frequency set on the generator. The first maximum in the diffraction pattern has been chosen to be the modulated heating source by means of a pinhole. Once the beam is modulated, the

laser is focused onto the sample, film or filament, by a spherical or cylindrical lens, here of 10 cm focal length.

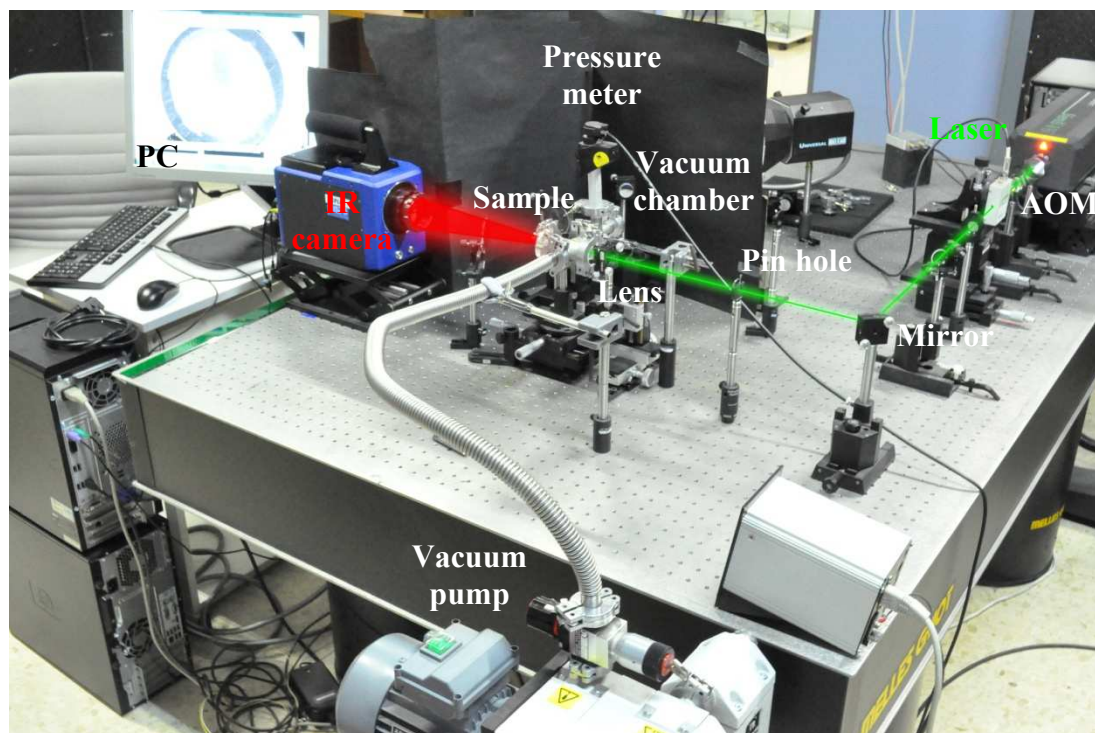


Figure 3.10: Photo of the set up in the laboratory.

Then, we find the vacuum chamber, where the samples are placed, connected to the vacuum pump LEYBOLD Trivac. The chamber is a product of our own design, simple and low cost, as we only need a medium vacuum room of a few centimeters. In Figure 3.11 (left) we may see a photo, where we observe it is a vacuum cross chamber, which consists of four 1 inch ports with a length between opposite ports of 3.5 inches. Two of the ports in one of the arms are dedicated to the pressure meter and the vacuum pump. The other two ports in the second arm are sealed with sapphire windows, transparent to both infrared and visible radiation. The laser beam enters the chamber through one of the windows and the infrared radiation coming from the sample crosses the second window before reaching the camera. The pressure in the vacuum chamber can be controlled between room pressure (10^3 mbar) and 10^{-3} mbar.

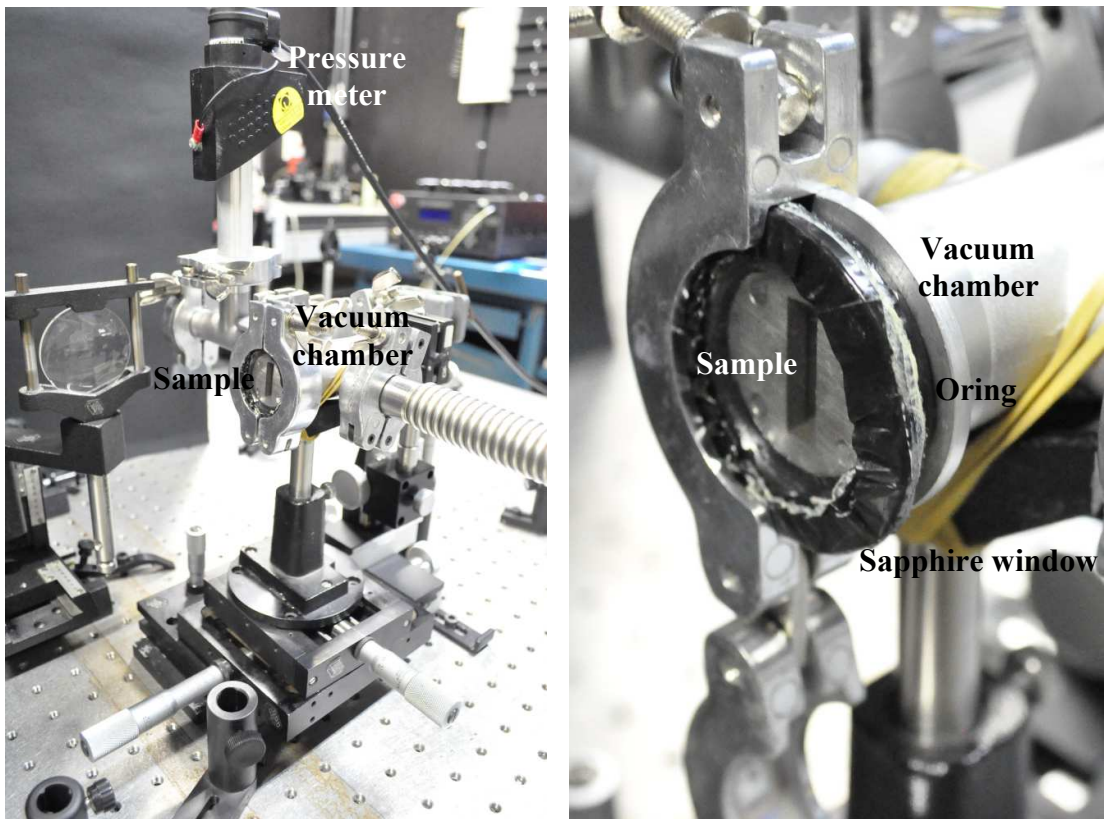


Figure 3.11: Photo of the whole vacuum chamber (left) and the place for the samples (right).

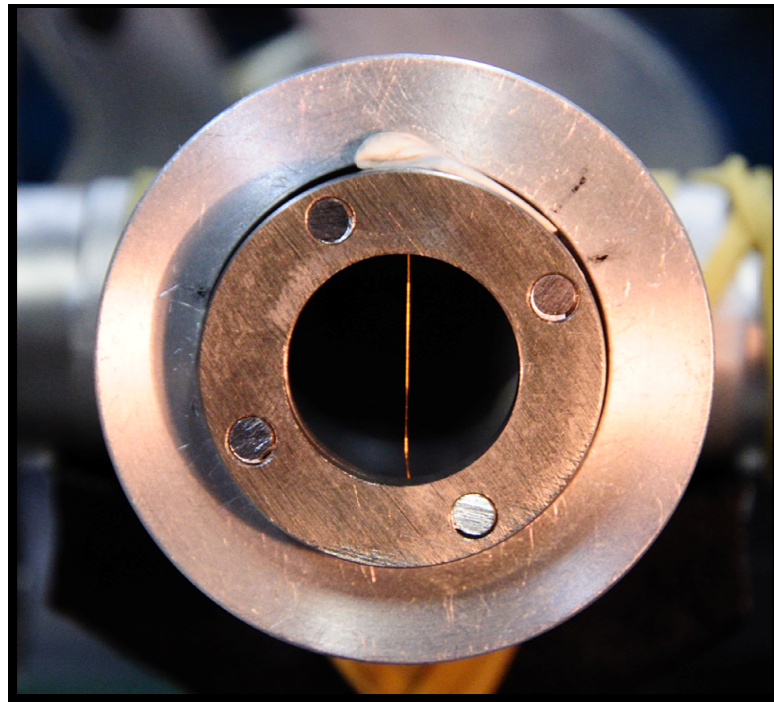


Figure 3.12: Photo of the exit with a sample holder and a Cu filament inside.

It is in the edge of the port, close to the exit window, where the samples are located, as shown in Figure 3.12, in order to collect the most of the infrared radiation. A sample holder was designed according to the requirements of the studied samples. Thus, our model consists of two steel pieces of the port size, which trap the samples in between by means of four screws in the border. The holder has a hole in the middle to place the samples, which was ordered with different shapes and sizes, to suit each sample, large or short films or filaments.

After heating the sample, it is still possible, mainly when working with filaments, that some part of the laser beam does not incise into the sample, so it continues straight to the camera. To prevent direct laser radiation from reaching and causing damage to the camera lens, a silicon (Si) window, opaque to our green laser but transparent to the infrared radiation, has been placed before the camera.

The next step is the infrared radiation collection, here from the rear surface of the samples. We have used an infrared camera, CEDIP Jade J550M, with a detector array of 320x256 pixels of 30 μm pitch. The sensor material is InSb, which provides a detection waveband from 3.6 to 5.0 μm , as we may see in Figure 3.13. It may seem a problem that the measurements temperature range is the same as the room temperature, so that the camera might collect both the samples surface temperature and the room infrared radiation reflected in the sample surface. Thus, it would cause an apparent temperature of the samples different from real, in a grade depending on the samples characteristics. Indeed, the camera does collect extra room radiation, but actually it is not a problem for the measurements, as there is no need to know absolute values of the temperature, but only the temperature oscillation. That is why the constant contribution of the infrared radiation from the ambient does not affect the modulated measurements. Even the sometimes problematic Narcissus effect is avoided when working with modulated thermography. This effect happens when infrared radiation is emitted by the own detector, although it is cooled, reflected in the sample and collected by itself as if it had been emitted by the sample. The same reason applies here: as it is not a modulated contribution, it will not affect the measurements.

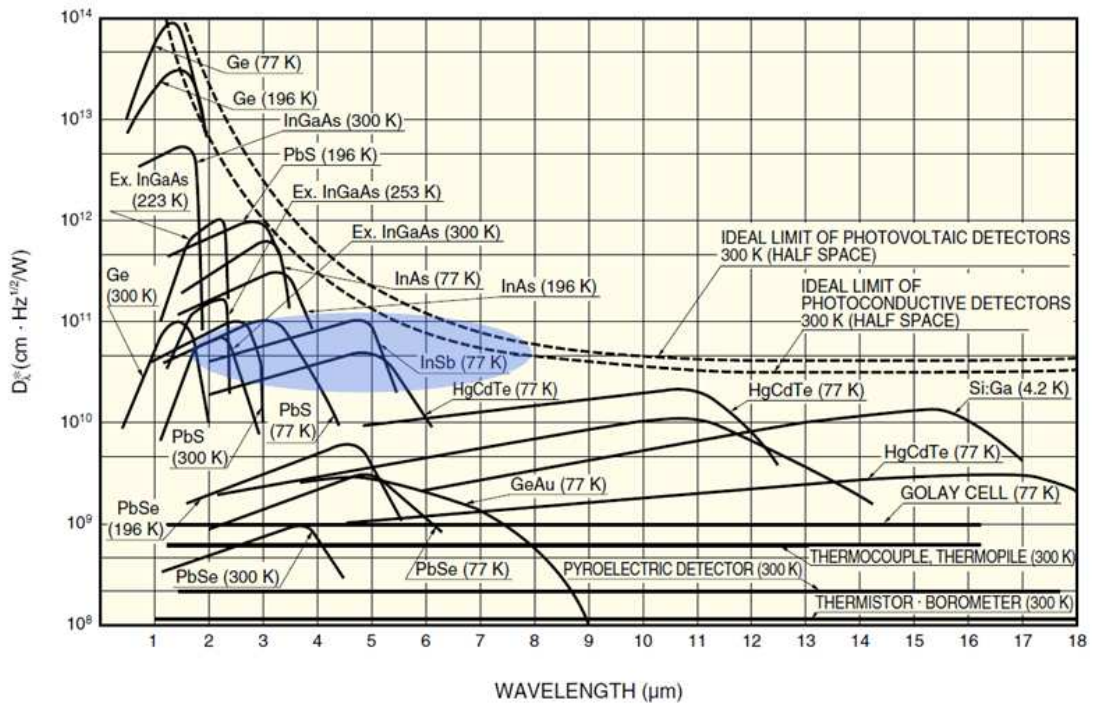


Figure 3.13: Spectral response of various infrared detectors. [Technical information from Hamamatsu]

In addition to the previous characteristics, the infrared camera is provided with a lens of 50 mm focal length. That means a minimum working distance of 23.5 cm, what results in a spatial resolution of 137 $\mu\text{m}/\text{pixel}$. In other words, each pixel measures the average temperature over a square of 137 μm in side.

Another important parameter, mainly when dealing with good thermal conductors, is the maximum frame rate, for this camera 170 Hz at full window. Nevertheless, it is possible to work under the *subwindowing mode*, which consists on reducing the picture size, so that the frame rate may be increased. This camera let us work with three different modes in addition to the full frame mode, which are the half frame (160x120), quarter frame (80x60) and custom size (64x8). This way, the frame rate increases up to a maximum of 4000 Hz.

The Noise Equivalent Temperature Difference (NETD), the temperature needed to produce an incident signal equal to the internal noise of the detector, that is a parameter to express the thermal resolution, is for this camera lower than 25 mK.

However, it is still possible to reduce the noise in the measurements by increasing the number of frames recorded to later extract the information, as [48, 49]:

$$Noise = \frac{2}{\sqrt{f_r \cdot t}} NETD \quad (3.24)$$

where f_r is the frame rate and t the integration time. Thus, by recording an average of 4000 images per measurement, we have gotten noise levels as low as 1 mK.

All the information recorded is directed to a lock-in module connected to a PC with a lock-in software provided with the camera. There, by means of a frequency reference from the AOM, the signal is demodulated into the amplitude and phase of the oscillating temperature of the sample surface. In Figure 3.14 images of the amplitude and phase of an anisotropic film are shown. As we may see, the software lets us select the information on amplitude and phase along the two principal directions of the material at the same time, so that we can easily apply the slopes method. Nevertheless, all possible profiles over the amplitude and phase maps are available.

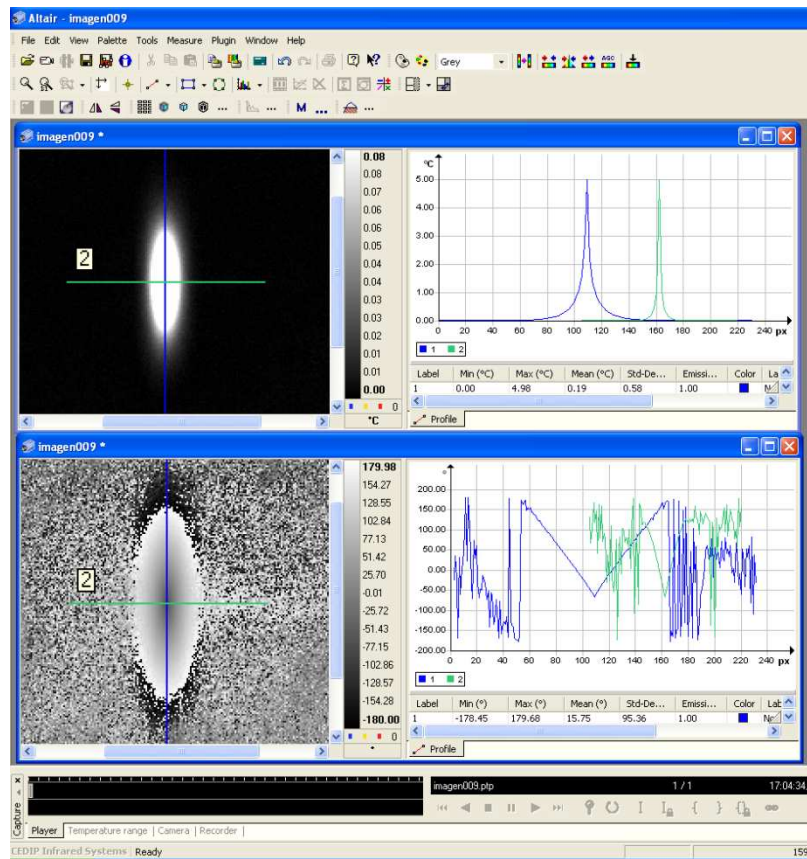


Figure 3.14: Amplitude and phase images of the rear surface temperature of an anisotropic film.

3.4. Results and discussion

As it was previously introduced, the thin films and filaments thermal diffusivity measurement at low frequencies requires that the model includes the contribution of heat losses, since they become significant at that range. As traditionally, the slopes method considers heat losses by convection and radiation, neglecting the contribution of heat conduction to the gas because of the low value of the gas thermal conductivity, and manages to retrieve the accurate value by means of the product of the slopes of the amplitude and phase representations as a function of the distance to the heating spot (2.46 or 3.22). Nevertheless, in spite of the good results for good thermal conductors [9-13] characterization, in the case of thin films and filaments of low thermal conductivity the method gives overestimated values of the thermal diffusivity, as found in literature [11, 12, 43] and measured experimentally, so it is clear that the method fails when dealing with such samples. As an approach to clarify the mechanism responsible for this overestimation, the influence of the traditionally neglected contribution of heat losses by conduction to the gas has been theoretically studied in section 3.2, showing a huge effect on the surface temperature results, such that the linearity of the temperature representations is lost and so the slopes method cannot apply.

We can see an example of this effect in Figure 3.15, where the experimental results for the surface temperature of a 34 μm diameter PEEK filament measured at $f=0.24$ Hz are shown. The measurements have been performed in air (solid symbols), where all possible heat losses contribute, and in vacuum (open symbols), where conduction to the gas and convection do not work. As the slopes method states, the phase and the natural logarithm of the amplitude must present a linear behaviour with the distance to the heating spot. However, we can see that only for the measurement in vacuum (open symbols) they exhibit the linear behaviour, even though they are not parallel, as heat losses by radiation remain. For the results in air, on the contrary, they show a loss of linearity, and therefore it is not possible to apply the slopes method to retrieve the correct diffusivity value.

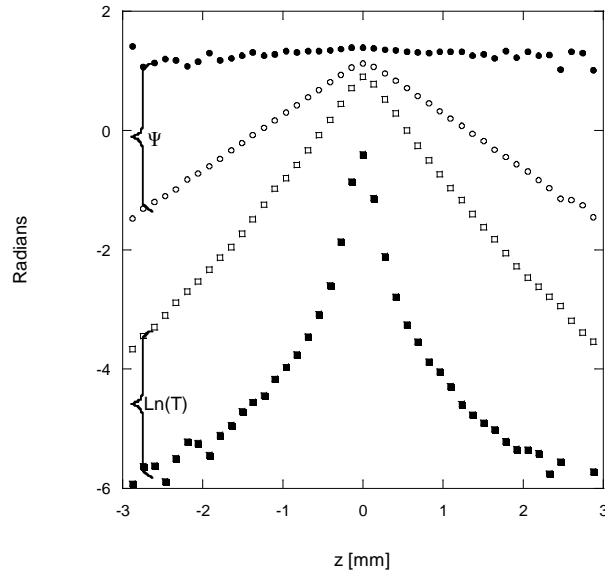


Figure 3.15: Amplitude (squares) and phase (circles) experimental results of the surface temperature of a 34 μm diameter PEEK filament measured at $f=0.24$ Hz in air (solid symbols) and in vacuum (open symbols).

In order to check experimentally that the neglected heat conduction to the gas is responsible for the overestimation in thermal diffusivity retrieval by the slopes method when working in air, we measure the thermal diffusivity of a 25 μm PEEK film at a frequency of 0.12 Hz inside a vacuum chamber as a function of the pressure, Figure 3.16. In solid symbols the experimental diffusivity values obtained by the slopes method are represented, once corrected the heat losses by convection and radiation by means of the equation (2.46). The red line represents the theoretical simulation of the diffusivity value considering heat losses only by convection and radiation, which are cancellable, so that the correct value, independent of the pressure, is obtained. The blue line, on the other hand, accounts for the contribution also of the heat losses by conduction to the gas, including the thermal conductivity of the gas dependence on the pressure [50]. Although we know this mechanism curves the expected straight lines, we have applied the slopes method, as it would have been done experimentally, to obtain a diffusivity value. As we may observe, the simulation perfectly fits the experimental results.

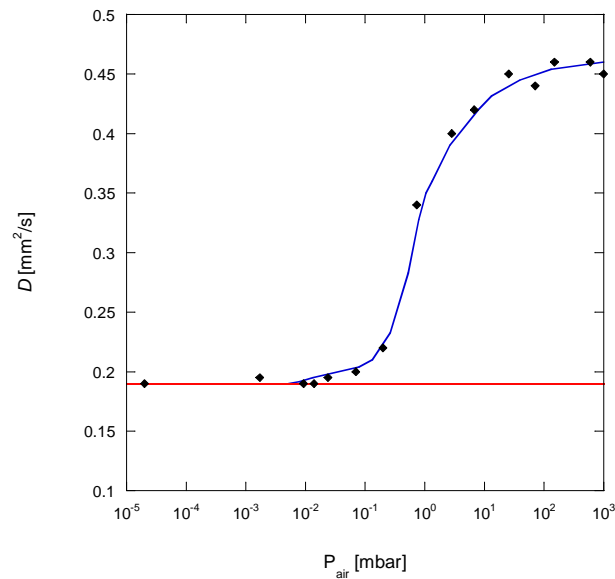


Figure 3.16: Thermal diffusivity of a 25 μm thick PEEK film as a function of the pressure. Solid symbols correspond to experimental results, measured at a frequency of 0.12 Hz, and lines are the theoretical simulations under the model considering only convection and radiation (red) and the model including conduction to the gas (blue).

Therefore, we can confirm it is the heat conduction to the gas the mechanism responsible for the overestimation in the thermal diffusivity value of thin films and filaments of low conductivity when measured in air, as the slopes method cannot be correctly applied for curved lines.

Even so, it is worth noting that the effect obtained, and so the retrieved value, is not only due to the conduction to the gas, but to all the three mechanisms together. Convection and radiation change the slopes value, but they do not curve the representations, it is the conduction to the gas who does it. However, the whole effect is a contribution of all of them, as we may see in Figure 3.17. Black lines represent the adiabatic simulation for the surface temperature of a 25 μm thick PEEK film at 0.12 Hz, parallel straight lines as expected. Green lines stand for the heat losses contribution of only the conduction to the gas, curved as shown before. Lastly, blue lines account for the model considering the three of the heat losses mechanisms, also curved but higher effect than only with the conduction to the gas contribution. We

can see that experimental results from measurements in air, symbols, fit the model including all contributions, not the one considering only the conduction to the gas.

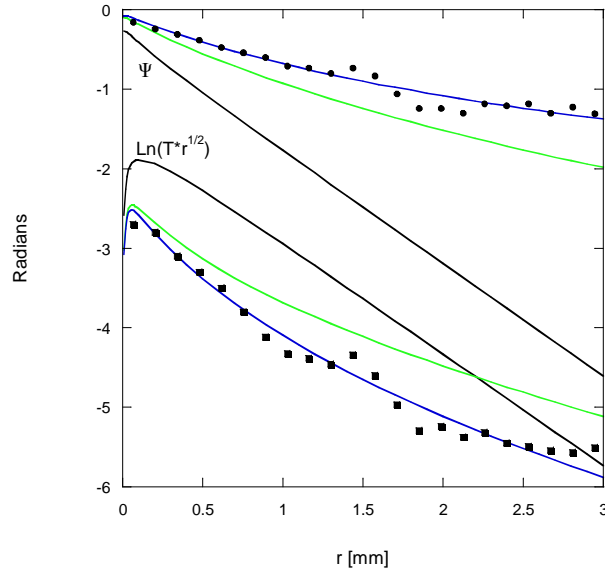


Figure 3.17: Surface temperature representations of a 25 μm thick PEEK film at frequency of 0.12 Hz. Solid symbols correspond to experimental results, measured in air. Lines stand for theoretical simulations: in black it is shown the theoretical adiabatic behaviour, green lines correspond to the heat losses model considering only conduction to the gas, and in blue, the model including all heat losses.

Hence, we have identified the problem and developed a model that fits the experimental results. Although the slopes method is not valid to retrieve diffusivity values for thermally thin films and filaments of low conductivity if measured in air, nonlinear methods could be applied to obtain them. Nevertheless, we prefer using linear methods, the slopes method, despite the drawback of performing the measurements in vacuum.

Below, Figure 3.18, some examples of experimental measurements of these kind of samples, in air and in vacuum, are shown together with the theoretical simulations by this model.

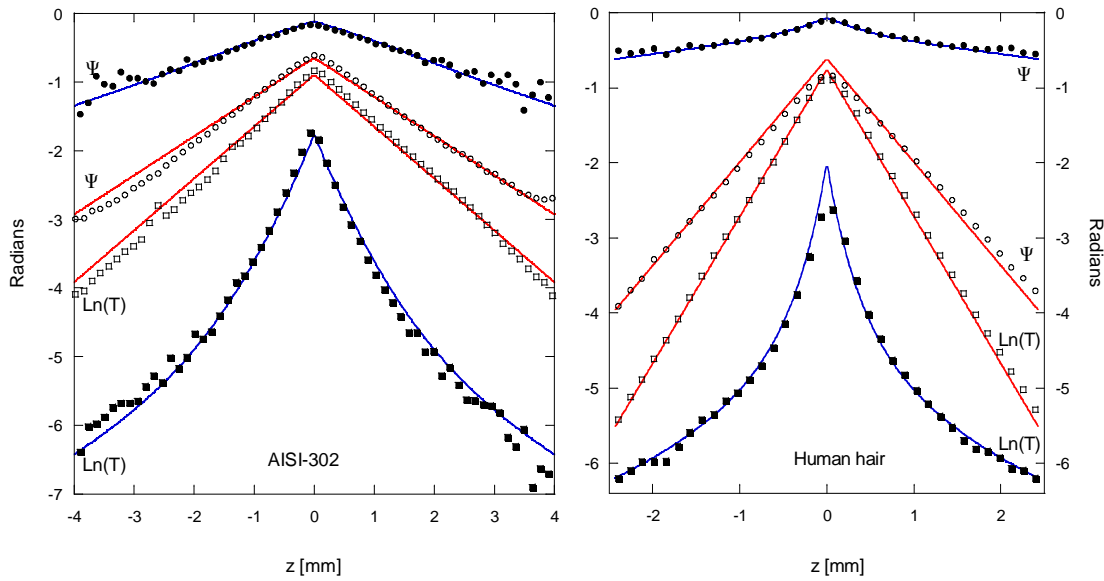


Figure 3.18: Surface temperature representations of a 25 μm diameter steel (AISI-302) filament at frequency $f=0.48$ Hz (left) and a 60 μm diameter human hair at frequency $f=0.12$ Hz (right). Lines represent the theoretical simulations according to the model in air (blue, $h=25$) and in vacuum (red, $h=6$) with $D_{\text{AISI-302}}=3.6 \text{ mm}^2/\text{s}$ and $D_{\text{hair}}=0.14 \text{ mm}^2/\text{s}$. Solid symbols correspond to experimental results in air while open symbols stand for measurements in vacuum.

As we may observe, these two cases of thin filaments of low conductivity are deeply affected by heat losses, but even so, the model fits the experimental results both in case of air and of vacuum. In air (solid symbols) the representations are curved, as expected by the model (blue lines). It is not possible to use the slopes method to obtain a diffusivity value, but the only option would be a nonlinear fit. In vacuum (open symbols), the results remain straight, although not parallel, as it is also considered in the model (red lines). The slopes method does apply now to compensate the heat losses by radiation that still remain in vacuum to retrieve a correct diffusivity value, resulting so $D_{\text{AISI-302}}=3.6 \text{ mm}^2/\text{s}$ and $D_{\text{hair}}=0.14 \text{ mm}^2/\text{s}$.

Thus, we can establish a reliable method to determine diffusivity values even for thermally thin samples of low conductivity. That consists of performing measurements in a vacuum environment of at least 10^{-3} mbar, and applying the slopes method to the results by means of the product of the amplitude and phase representations slopes to cancel the effect of radiation heat losses.

Additionally, we confirm experimentally, as it was proved theoretically, Figures 3.6 and 3.7, that the thickness and the conductivity show a high influence on the magnitude of the overestimation.

Table 3.1 summarizes a collection of experimental data on different shapes and thicknesses of the same material, PEEK, whose diffusivity literature value is $0.19 \text{ mm}^2/\text{s}$ [42]. Measurements have been performed in air, wrongly applying the slopes method, and in vacuum, doing it correctly. For the thickest film, there is scarce difference with the literature value. However, it is clearly shown that the thinner the sample the higher the overestimation when measured in air, for both films and filaments. In vacuum, on the contrary, the right value is found for all film cases. Regarding the filaments, the value obtained in vacuum is rather higher than the expected value. But the results become independent of the filament diameter, so that the problem cannot be related to heat losses. In fact, it has been demonstrated that crystalline polymers increase their thermal diffusivity after drawing process [51, 52], and these PEEK filaments, whose degree of crystallinity has been measured to be 45%, are obtained by extrusion. Thus, we attribute the high value of the measured diffusivity to the structural changes induced during the fabrication process of the filaments.

Shape	D [mm^2/s]	
	Air	Vacuum
Film $\ell = 250 \text{ }\mu\text{m}$	0.20	0.19
Film $\ell = 125 \text{ }\mu\text{m}$	0.26	0.19
Film $\ell = 75 \text{ }\mu\text{m}$	0.30	0.19
Film $\ell = 25 \text{ }\mu\text{m}$	0.45	0.19
Filament $2b = 150 \text{ }\mu\text{m}$	0.75	0.50
Filament $2b = 34 \text{ }\mu\text{m}$	1.2	0.50

Table 3.1: Thermal diffusivity of several PEEK samples measured in air and in vacuum. The uncertainty is 5%.

Last, a collection of the samples measured in order to obtain accurate diffusivity values is presented in Table 3.2. All of them have been measured in vacuum and the values have been retrieved by the slopes method.

Material	Shape	D [mm ² /s]	D [mm ² /s]
		This work	Literature
Cu	Film $\ell = 100 \mu\text{m}$	122	116
Ni	Film $\ell = 100 \mu\text{m}$	22	22
Ni	Film $\ell = 10 \mu\text{m}$	21	22
AISI-302	Film $\ell = 100 \mu\text{m}$	3.8	3.7-4.0
PEEK	Film $\ell = 250 \mu\text{m}$	0.19	0.19
PEEK	Film $\ell = 125 \mu\text{m}$	0.19	0.19
PEEK	Film $\ell = 75 \mu\text{m}$	0.19	0.19
PEEK	Film $\ell = 25 \mu\text{m}$	0.19	0.19
Cu	Filament $50 \mu\text{m}$	120	116
Ni	Filament $125 \mu\text{m}$	19	22
Ti	Filament $125 \mu\text{m}$	8.8	9.0
AISI-302	Filament $125 \mu\text{m}$	3.8	3.7-4.0
AISI-302	Filament $25 \mu\text{m}$	3.6	3.7-4.0
AISI-302	Filament $10 \mu\text{m}$	3.6	3.7-4.0
Carbon Fiber T650/35	Filament $7 \mu\text{m}$	6.4	8.8
Carbon Fiber P100	Filament $10 \mu\text{m}$	310	325
PEEK	Filament $150 \mu\text{m}$	0.52	0.19
PEEK	Filament $34 \mu\text{m}$	0.52	0.19
Human hair	Filament $60 \mu\text{m}$	0.14	-

Table 3.2: Thermal diffusivity for several thin films and filaments, measured in vacuum with an error of 5%, and values found in literature [42, 45, 53-55] .

As we may observe, the agreement with the literature values is very good for both good and poor thermal conductors. The only discrepancy appears for the PEEK filaments, but the difference has been already attributed to the degree of crystallinity of these samples. It is worth mentioning the result obtained for the human hair. Although no reliable thermal diffusivity is available in the literature, the very low value we have obtained is consistent with the combination of the low thermal diffusivity of the keratin (the material the hair is made of) and the complicated internal structure of hair, with many layers introducing thermal resistances, which reduce the thermal diffusivity [56].

Thus, after identifying the problem and establishing a method to perform reliable measurements, we have been able to determine diffusivity values for samples whose diffusivities range between 0.14 and 310 mm²/s and that are as thin as 7 μm . Therefore, we have been able to overcome the problem of overestimation when measuring thin samples of poor thermal conductors.

According to the theoretical results obtained in section 3.2.1.B, the slopes method can also be used to measure the thermal diffusivity of anisotropic films along the main axes contained in the surface. Hence, we have been able to characterize the thermal diffusivity tensor of various anisotropic materials: a 100 μm thick film of pyrolytic graphite (PG), a 30 μm thick film of pyrolytic boron nitride (PBN), and a 175 μm thick carbon fiber reinforced polymer composite (PEEK). Results are shown in Table 3.3.

Material	Shape	D [mm^2/s]	
		This work	Literature
PEEK composite	Film $\ell = 175 \mu\text{m}$	5.5	6
		0.55	0.4
Pyrolytic graphite (PG)	Film $\ell = 100 \mu\text{m}$	203	215
		1.6	1.5
Pyrolytic boron nitride (PBN)	Film $\ell = 30 \mu\text{m}$	65	-
		1.2	-

Table 3.3: Thermal diffusivity of various anisotropic samples measured in vacuum with an error of 5%, and values found in literature[45, 53, 54].

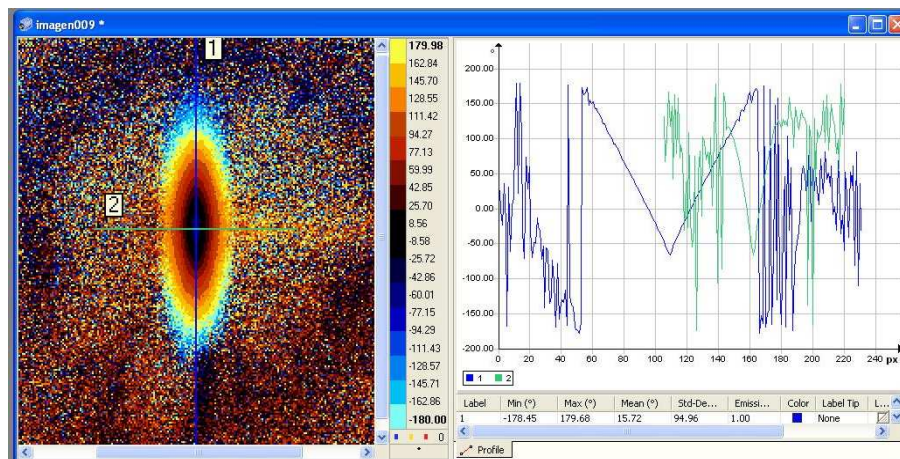


Figure 3.19: Surface phase thermogram of a PEEK composite sample, at a frequency $f = 0.48 \text{ Hz}$

As an example, Figure 3.19 shows the surface phase thermogram corresponding to the PEEK composite sample, at a modulation frequency of 0.48 Hz, where elliptical isophases, characteristic of anisotropic materials, can be clearly observed. Due to the very high thermal anisotropy ratio of these samples, different modulation frequencies must be used to measure the two principal thermal diffusivities accurately. That way, the lower (higher) thermal diffusivity was measured at modulation frequencies below (above) 1 Hz. The corresponding thermal diffusivity values obtained along the two principal directions were 5.5 and 0.55 mm²/s, which are in good agreement with the values of the diffusivity obtained for this sample using the mirage technique [57]. Similarly, for PG and PBN, frequencies ranging from 5 to 100 Hz are better suited for the highest thermal diffusivity measurements (203 mm²/s for PG and 65 mm²/s for PBN). Actually, using lower frequencies leads to boundary effects. On the contrary, for the lowest thermal diffusivity (1.6 mm²/s for PG and 1.2 mm²/s for PBN) frequencies below 3 Hz are used to avoid diffraction effects.

To verify also the ability of the slopes method to retrieve the effective thermal diffusivity of tubes and coated filaments, as demonstrated theoretically in section 3.2.2.2, we have used a commercial hypodermic needle with an outer diameter of 414 μm and an inner diameter of 256 μm. We have obtained a thermal diffusivity of 3.5 mm²/s, a typical value of stainless steel. Then, we have covered some needles with a layer of different thicknesses of a commercially available spray paint (matt black), in order to obtain increasing volume fractions of the coating layer: 0.14, 0.24, 0.46, 0.63 and 0.83. The results of the effective thermal diffusivity for the samples kept in vacuum are represented by solid symbols in Figure 3.20. The continuous line corresponds to the simulated value of the theoretical in-parallel thermal resistor model, using $D_{\text{needle}} = 3.5 \text{ mm}^2/\text{s}$, $K_{\text{needle}} = 15 \text{ W/mK}$, $D_{\text{paint}} = 0.2 \text{ mm}^2/\text{s}$ and $K_{\text{paint}} = 0.3 \text{ W/mK}$, which are the typical values of spray paint.

The agreement between the experimental values and the prediction confirms the ability of the slopes method to measure the effective thermal diffusivity of coated filaments.

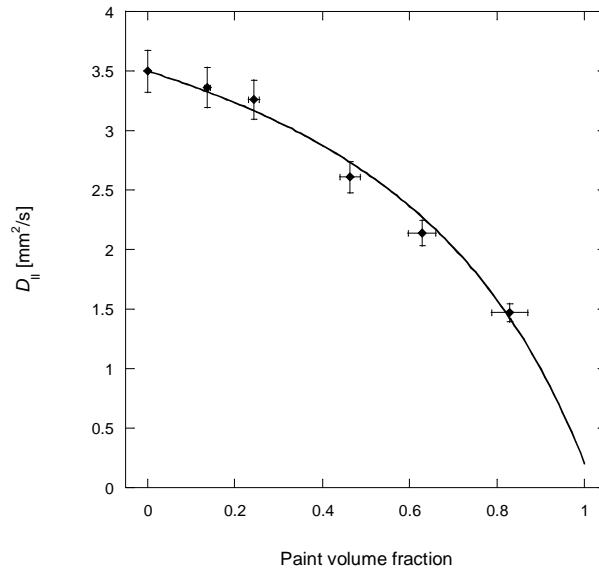


Figure 3.20: Effective thermal diffusivity of a painted hypodermic needle as a function of the paint volume fraction. Solid symbols are the experimental results and the continuous line corresponds to the simulated thermal diffusivity using the in-parallel thermal resistor model, using $D_{\text{needle}} = 3.5 \text{ mm}^2/\text{s}$, $K_{\text{needle}} = 15 \text{ W/mK}$, $D_{\text{paint}} = 0.2 \text{ mm}^2/\text{s}$, $K_{\text{paint}} = 0.3 \text{ W/mK}$.

As a further application of this, and concerning about the inability of lock-in thermography (as well as all transient experiments) to measure thermal conductivities unless a reference is used, we have measured the effective thermal diffusivity of a hypodermic needle filled with water in order to obtain the thermal conductivity of the needle. As a first step, the thermal diffusivity of the empty needle has been obtained. Then, the effective thermal diffusivity of the needle filled with water has been measured and the thermal conductivity of the needle retrieved. Two hypodermic needles of different outer and inner radii have been used, the first with $a_2 = 207 \text{ }\mu\text{m}$ and $a_1 = 105 \text{ }\mu\text{m}$, and the second with $a_2 = 157 \text{ }\mu\text{m}$ and $a_1 = 65 \text{ }\mu\text{m}$. The lateral scans of $\ln(T)$ and ψ for the thickest needle are shown in Figure 3.21. The thermal diffusivity of both empty needles is the same, $3.6 \text{ mm}^2/\text{s}$, while the effective thermal diffusivities of the needles filled with water have resulted $2.6 \text{ mm}^2/\text{s}$ and $2.8 \text{ mm}^2/\text{s}$, respectively. By using the expression of the effective thermal diffusivity of a coated cylinder and using the thermal properties of water ($D_{\text{water}} = 0.144 \text{ mm}^2/\text{s}$, $K_{\text{water}} = 0.60 \text{ W/mK}$), the thermal conductivity of the needle has been obtained:

$K_{\text{needle}} = 14 \text{ W/mK}$, with an uncertainty of 10%. This value is close to the typical value of the thermal conductivity of stainless steel. On the other hand, it is worth noting that the uncertainty depends on the thickness of the tube wall: the thinner the wall the more accurate the retrieved thermal conductivity is.

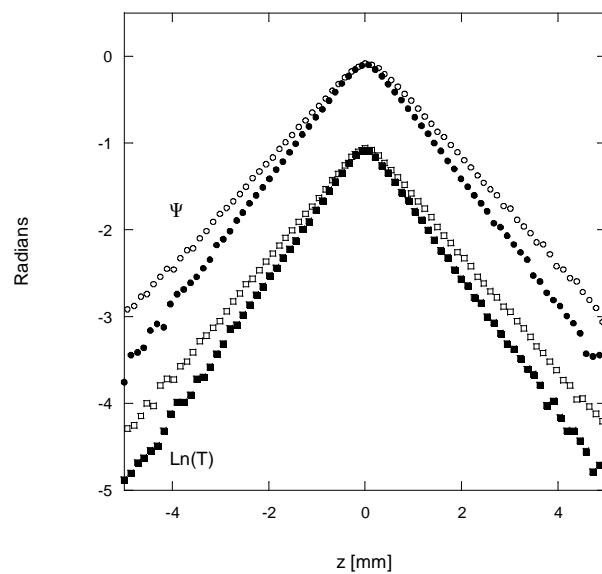


Figure 3.21: Lateral dependence of $\ln(T)$ and ψ for a hypodermic needle with an outer diameter of $414 \mu\text{m}$ and an inner diameter of $210 \mu\text{m}$. Measurements were performed for the empty needle (open symbols) and for the needle filled with water (solid symbols).

4. Semitransparent samples: thermal diffusivity and optical absorption coefficient simultaneous measurements

4.1. Introduction

In this chapter Photothermal radiometry (PTR) will be used. As there is no need to record the full image of the surface temperature, but only the temperature of a small area over the surface, a monolithic infrared (IR) detector is selected, since it presents a better signal to noise ratio than the detectors of the camera and results cheaper. Modulated PTR has been a technique widely used to measure the thermal diffusivity of a large variety of materials [9, 30, 34, 37, 61-63]. Besides, by selecting a focused or plane light beam, the in-plane or in-depth thermal properties of anisotropic materials may be obtained, respectively [54].

In addition to this, some photothermal techniques (photoacoustic spectroscopy or mirage effect) have proven to be very accurate in measuring the optical absorption coefficient of gases, liquids and solids, competing with success against optical techniques in the extreme cases of weakly or highly absorbing materials [14-16].

In this chapter, a systematic study of modulated plane PTR to retrieve simultaneously and accurately both the in-depth thermal diffusivity (D) and the optical absorption coefficient (α) of homogeneous samples is performed, as a first step, stating the limits of the technique.

Further in the study, multilayered samples are considered. Since the seminal work by Mandelis and co-workers [17] modulated PTR has been used for thermal conductivity depth profile reconstruction of heterogeneous samples such as surface hardened steels [18-24], functionally graded materials [25] and partially cured dental resins [26]. In the last years, two works dealing with the application of modulated PTR to the simultaneous reconstruction of the in-depth varying absorption coefficient and thermal diffusivity of semitransparent heterogeneous samples have been published [27, 28].

Here, it is studied the modulated PTR capability to obtain simultaneously α and D in multilayered materials by applying the thermal quadrupole method. The thermal quadrupole method, introduced in Chapter 2, has been applied in the framework of heat conductive transfer to calculate the surface temperature of opaque multilayered samples [29] and to calculate the combined radiative and conductive heat transfer in semitransparent bulk materials [30]. Now, the method is extended to calculate the surface temperature of multilayered semitransparent samples in a compact way.

For both homogenous and multilayered samples, the theoretical model for modulated plane PTR is studied first, including some disturbing effects modifying the samples surface temperature, such as heat losses, multiple reflexions of the incident light, transparency of the samples to the infrared and lateral heat diffusion. Then, the PTR measuring setup is shown. Last, a large collection of samples of all optical possibilities are measured to prove the validity of the models and establish the conditions and limits to perform simultaneous accurate α and D measurements by modulated PTR. Also, two applications on the multilayers are presented, one of them showing the effect of paint layers on the PTR measurements and the other allowing the characterization of thermal contact resistances between layers.

4.2. Theoretical model

In this section, the theoretical model of light absorption and heat propagation through semitransparent sheets is studied. First, an homogenous sample is considered, for which the temperatures at front and rear surfaces are calculated and thus, an optical classification and the possible parameters to be characterized according to it are established. Then, the thermal quadrupole method is introduced to study multilayer semitransparent samples, developing a model to express the temperatures at front and rear surfaces in a compact way. Last, some effects modifying the temperatures are studied, such as heat losses, multiple reflexions of the incident light, transparency of the samples to the infrared and lateral heat diffusion.

4.2.1. Homogeneous solids

Let us consider a semitransparent sheet of thickness ℓ , illuminated by a plane light beam of wavelength λ and intensity I_0 (W/m²) modulated at a frequency f ($\omega=2\pi f$). The geometry of the problem is shown in Figure 4.1.

According to the Beer-Lambert Law, the light intensity inside the sample is $I(z) = I_0(1-R)e^{-\alpha z}$, where R and α are the optical reflection and absorption coefficients of the sheet at the wavelength of the light beam, respectively. By resolving again the Helmholtz equation (2.11) with heat flux continuity at the front and rear surfaces in absence of heat losses, the oscillating component of the temperature results [64]

$$T(z) = \frac{I_0(1-R)\alpha^2}{2K\sigma(\sigma^2 - \alpha^2)} \left[\frac{(e^{-\alpha\ell} - e^{-\sigma\ell})e^{\sigma z} + (e^{-\alpha\ell} - e^{\sigma\ell})e^{-\sigma z} + \frac{\sigma}{\alpha}(e^{\sigma\ell} - e^{-\sigma\ell})e^{-\alpha z}}{e^{\sigma\ell} - e^{-\sigma\ell}} \right] \quad (4.1)$$

where $\sigma = \sqrt{i\omega/D}$ is the thermal wave vector and K and D are the thermal conductivity and thermal diffusivity of the sample, respectively.

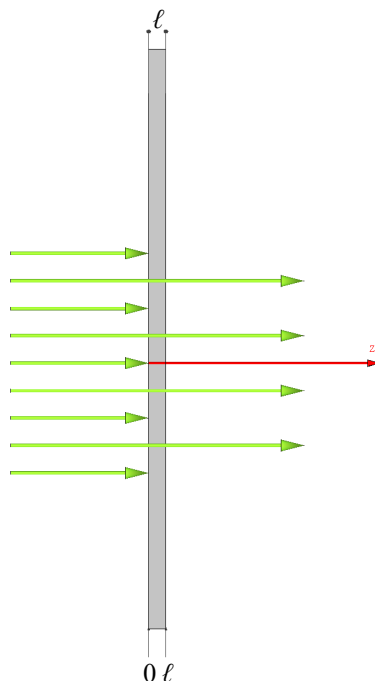


Figure 4.1: Semitransparent sheet of thickness ℓ illuminated by a plane light beam.

In modulated PTR, the voltage in the detector is recorded, and normalization procedures are needed in order to suppress the instrumental factor, i.e. the dependence of the detection electronics (IR detector, preamplifier and lock-in amplifier) on frequency. Several normalization procedures have been previously proposed: self-normalization, which consists of dividing the PTR signals recorded at the rear and front surfaces [65]; comparison with a reference material [66]; obtaining the instrumental factor by impinging the laser beam directly on the IR detector; and comparison of the PTR signal of the sample with and without a backing liquid [62]. After testing these normalization procedures the self-normalization method has been selected. Although it is not useful for semiinfinite (very thick) samples, the self-

normalization method provides the highest signal to noise ratio and amplitude and phase contrast, as well as some other advantages that will be shown below.

Hence, the ratio at the rear and front surfaces is:

$$T_n = \frac{T(\ell)}{T(0)} = \frac{(e^{-\alpha\ell} - e^{-\sigma\ell})e^{\sigma\ell} + (e^{-\alpha\ell} - e^{\sigma\ell})e^{-\sigma\ell} + \frac{\sigma}{\alpha}(e^{\sigma\ell} - e^{-\sigma\ell})e^{-\alpha\ell}}{2e^{-\alpha\ell} - e^{\sigma\ell} - e^{-\sigma\ell} + \frac{\sigma}{\alpha}(e^{\sigma\ell} - e^{-\sigma\ell})} \quad (4.2)$$

As can be seen, the self-normalized temperature depends on ℓ/\sqrt{D} and on $\alpha\ell$, but does not depend on K , and therefore, both α and D can be retrieved simultaneously. Three main cases can be distinguished:

(1) If the sheet is opaque ($\alpha\ell \rightarrow \infty$) and thermally thick ($\ell/\sqrt{D} \rightarrow \infty$) the self-normalized temperature (4.2) reduces to $T_n \approx 2e^{-\sigma\ell}$, indicating that both the natural logarithm of the self-normalized temperature amplitude, $\text{Ln}(T_n)$, and its phase, $\Psi(T_n)$, are parallel straight lines when plotted against \sqrt{f} , with the same slope $m = -\ell\sqrt{\pi/D}$. This equation provides a well-known method to measure the thermal diffusivity of opaque sheets [67].

(2) If the sample is transparent ($\alpha\ell \rightarrow 0$) equation (4.2) becomes $T_n \approx 1$, showing that both surfaces are at the same temperature.

(3) For semitransparent samples, experimental results of the self-normalized temperature T_n must be fitted to the equation (4.2).

The three cases are shown in Figure 4.2, where calculations have been performed for a sample of $D=0.5 \text{ mm}^2/\text{s}$ and $\ell=0.5 \text{ mm}$. Note that for the opaque case the linear behaviour only holds for $\sqrt{f} \geq 1.6$, i.e. when the material is thermally thick ($\mu \leq \ell/2$).

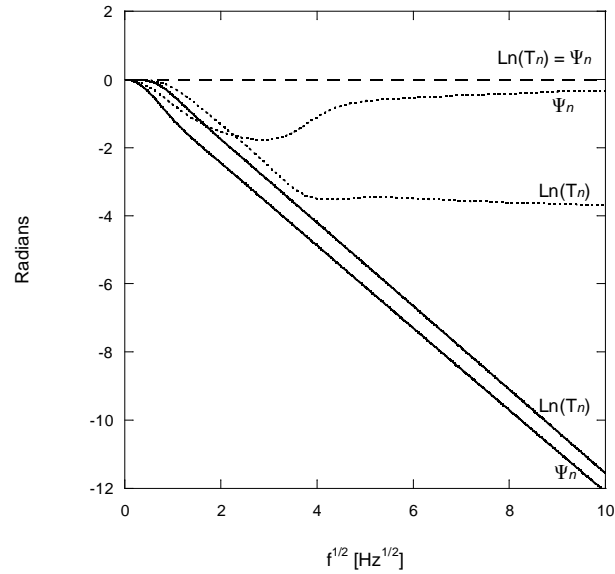


Figure 4.2: Simulations of the natural logarithm of the amplitude and phase of the self-normalized temperature as a function of the square root of the frequency for a 0.5 mm thick glass sheet ($D = 0.5 \text{ mm}^2/\text{s}$). Three absorption coefficients have been considered: an opaque material ($\alpha \rightarrow \infty$, continuous lines), a transparent material ($\alpha \rightarrow 0$, dashed lines) and a semitransparent material ($\alpha = 8 \text{ mm}^{-1}$, dotted lines).

Figure 4.3 serves as an optical classification of a sample depending on its α and ℓ values. For $\alpha\ell < 0.8$ the sample is said to be transparent, showing almost flat $\text{Ln}(T_n)$ and $\Psi(T_n)$. In this case, no information on the thermal and optical properties can be obtained from photothermal measurements. For $\alpha\ell > 10$ the sample behaves as opaque, but only for $\alpha\ell > 30$ both $\text{Ln}(T_n)$ and $\Psi(T_n)$ are completely parallel straight lines when plotted as a function of \sqrt{f} . In this case, only the thermal diffusivity of the sample can be obtained. For $0.8 < \alpha\ell < 10$ the sample is semitransparent, and both α and D can be retrieved when fitting $\text{Ln}(T_n)$ and $\Psi(T_n)$ to the equation (4.2).

It is worth mentioning that the transition between the three regions is not abrupt, the values $\alpha\ell = 0.8$ and $\alpha\ell = 10$ are indeed soft barriers. Note also that the same sheet can vary its classification depending on its thickness. In fact, a material can be classified as opaque, semitransparent or transparent by appropriately selecting its thickness. For instance, a copper film 1 nm thick is transparent, while a glass slab 1 km thick is opaque. However, concerning the application of photothermal techniques, this

thickness selection has severe restrictions. Actually, the thickness must range between 0.2 and 4 mm in order to have a good signal to noise ratio together with a high enough amplitude and phase contrast.

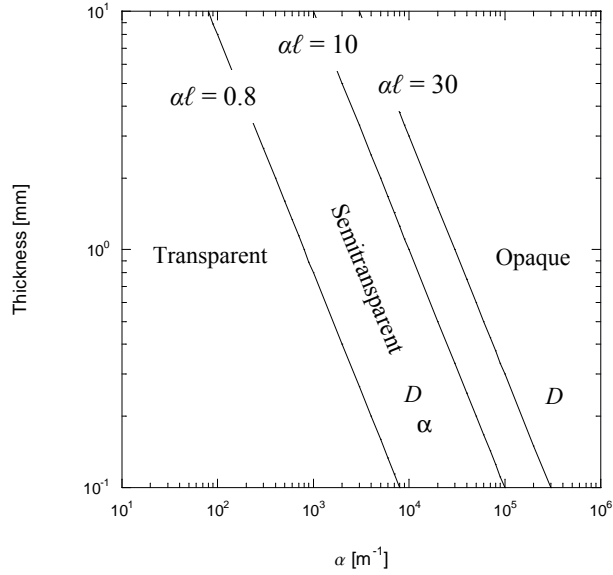


Figure 4.3: Optical classification of solids according to the pair (α, ℓ) .

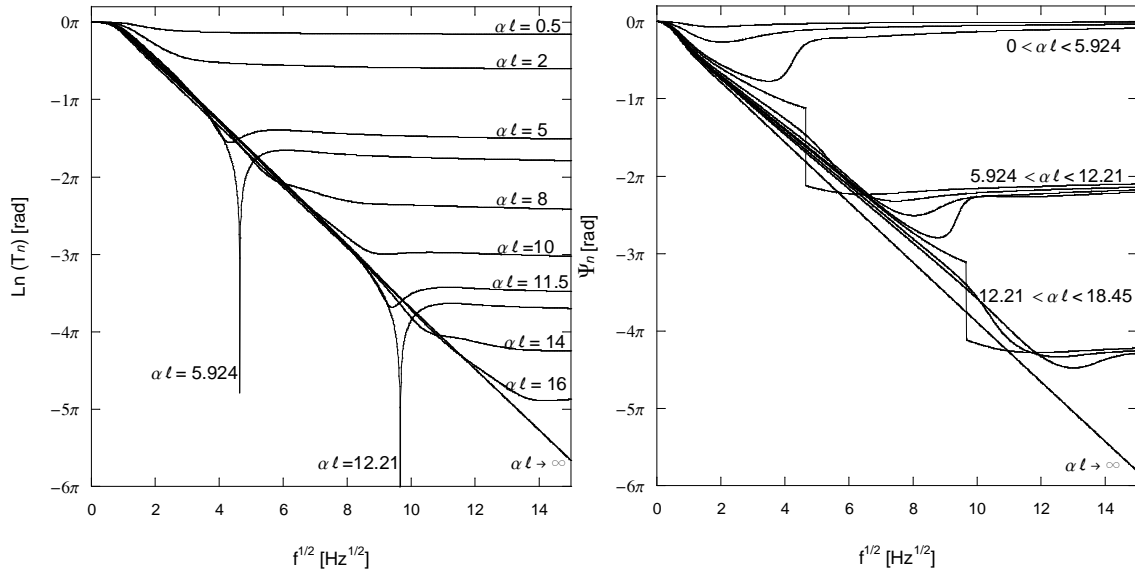


Figure 4.4: Behaviour of the natural logarithm of the amplitude (left) and phase (right) of the normalized temperature of semitransparent sheets as a function of the square root of the frequency. Simulations have been performed for $\ell / \sqrt{D} = 0.7 \text{ s}^{1/2}$, with increasing values of $\alpha \ell$.

The range $0.8 < \alpha\ell < 10$ may seem very restrictive, but we have to remember that the transmission is given by $\tau = e^{-\alpha\ell}$, so that this method allows us to measure the optical properties of samples with transmission coefficients ranging from 0.5 down to 4×10^{-5} .

Note also that for $10 < \alpha\ell < 30$, $\text{Ln}(T_n)$ and $\Psi(T_n)$ are almost straight lines (see, for instance, the behaviour for $\alpha\ell = 14$ and 16 in Figure 4.4), since the curved part appears at high frequencies, where the photothermal signal is so small that these frequencies are not usable. However, these straight lines are not parallel, and only the slope of $\text{Ln}(T_n)$ should be used to obtain the diffusivity value.

In Figure 4.4 it is studied in detail the evolution of $\text{Ln}(T_n)$ and $\Psi(T_n)$ as a function of \sqrt{f} for a sample with $\ell/\sqrt{D} = 0.7 \text{ s}^{1/2}$. Different values of $\alpha\ell$ are considered, from zero (transparent) to infinite (opaque). As we may observe, for $\alpha\ell = 5.9243, 12.211, 18.455\dots$, the amplitude of the normalized temperature goes to zero (the sharp dips in Figure 4.4 left). These $\alpha\ell$ values correspond to the solutions of the transcendent equation $\{\text{Re}(T_n) = 0, \text{Im}(T_n) = 0\}$, where Re is the real part and Im is the imaginary part. It is worth mentioning that these $\alpha\ell$ values are independent of the diffusivity. Those sharp dips are produced at frequencies satisfying $\alpha\mu = 1$, i.e. equal thermal diffusion length and optical penetration depth. Figure 4.4 right shows the behaviour of the normalized phase. As can be seen, at high frequencies it converges to different asymptotic values depending on the $\alpha\ell$ value: to zero for $\alpha\ell < 5.9243$, to -2π for $5.9243 < \alpha\ell < 12.211$, to -4π for $12.211 < \alpha\ell < 18.455$, etc.

4.2.2. Multilayered solids

Let us now consider a semitransparent multilayered sample, as it is depicted in Figure 4.5, illuminated by a plane light beam, modulated at a frequency f . Each layer is characterized by its thermal conductivity (K_i), thermal diffusivity (D_i), optical absorption coefficient (α_i) and thickness (ℓ_i).

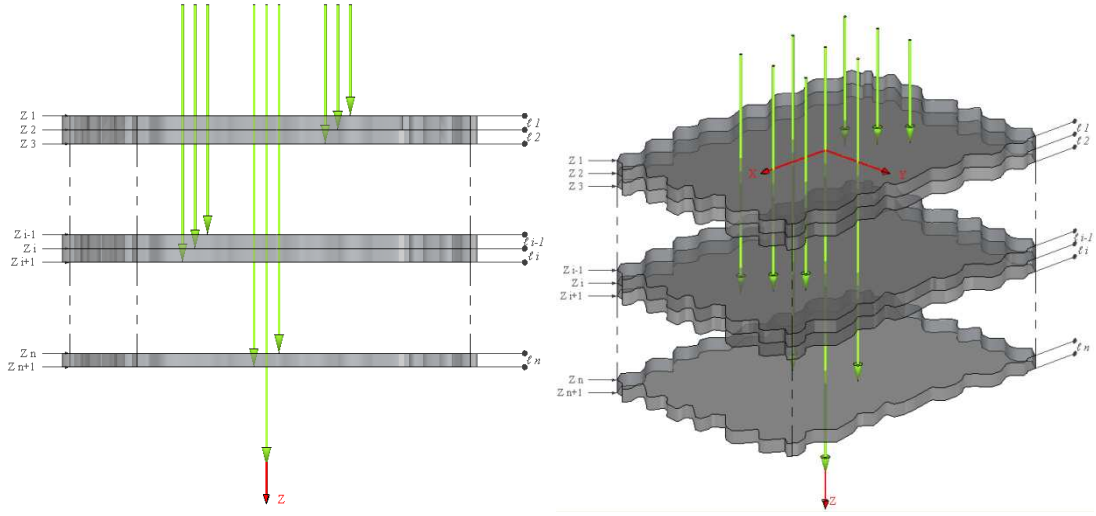


Figure 4.5: Diagram of a semitransparent multilayered sample.

The one-dimensional (1-D) heat diffusion equation for each layer writes

$$\frac{d^2 T_i}{dz^2} - \sigma_i^2 T_i = -\frac{Q_i}{K_i} \quad (4.3)$$

where $\sigma_i = \sqrt{i\omega / D_i}$ is the thermal wave vector, and $Q_i = \frac{I_i}{2} \alpha_i e^{-\alpha_i(z-z_i)}$ is the heat source, being I_i the incident light intensity reaching layer i , that in the absence of internal reflections is given by $I_i = I_o e^{-(\alpha_1 \ell_1 + \alpha_2 \ell_2 + \dots + \alpha_{i-1} \ell_{i-1})}$. The solution to the equation (4.3) is usually expressed in terms of exponential functions [64]

$$T_i(z) = A_i e^{\sigma_i(z-z_i)} + B_i e^{-\sigma_i(z-z_i)} + C_i e^{-\alpha_i(z-z_i)} \quad (4.4)$$

where A_i and B_i are constants obtained from the boundary conditions and

$$C_i = \frac{I_i \alpha_i}{2K_i (\sigma_i^2 - \alpha_i^2)} \quad (4.5)$$

However, let us work for this case of multilayer samples under the thermal quadrupole method, where it is more convenient to use hyperbolic functions:

$$T_i(z) = A_i \text{Sinh}[\sigma_i(z - z_i)] + B_i \text{Cosh}[\sigma_i(z - z_i)] + C_i e^{-\alpha_i(z - z_i)} \quad (4.6)$$

$$\phi_i(z) = -K_i \frac{dT_i}{dz} = -K_i \sigma_i \{A_i \text{Cosh}[\sigma_i(z - z_i)] + B_i \text{Sinh}[\sigma_i(z - z_i)]\} + K_i C_i \alpha_i e^{-\alpha_i(z - z_i)}$$

where ϕ is the heat flux.

By applying the equations (4.6) at the front (z_i) and rear (z_{i+1}) surfaces of layer i , a matrix relationship between temperature and heat flux at both surfaces is obtained:

$$\begin{pmatrix} T_i(z_i) \\ \phi_i(z_i) \end{pmatrix} = \begin{pmatrix} a_i & b_i \\ c_i & d_i \end{pmatrix} \begin{pmatrix} T_i(z_{i+1}) - X_i \\ \phi_i(z_{i+1}) - Y_i \end{pmatrix} \quad (4.7)$$

where $a_i = d_i = \text{Cosh}(\sigma_i \ell_i)$, $b_i = \frac{\text{Sinh}(\sigma_i \ell_i)}{K_i \sigma_i}$, $c_i = K_i \sigma_i \text{Sinh}(\sigma_i \ell_i)$,

$$X_i = C_i \left[\frac{\alpha_i}{\sigma_i} \text{Sinh}(\sigma_i \ell_i) - \text{Cosh}(\sigma_i \ell_i) + e^{-\alpha_i \ell_i} \right] \text{ and}$$

$$Y_i = C_i K_i \left[\sigma_i \text{Sinh}(\sigma_i \ell_i) - \alpha_i \text{Cosh}(\sigma_i \ell_i) + \alpha_i e^{-\alpha_i \ell_i} \right].$$

Note that if the sample is opaque, then $X_i = Y_i = 0$ and we obtain the model for a sheet that we got in section 2.5. According to the equation (4.7), the temperatures at the front and rear surfaces of layer i can be obtained provided the heat fluxes at its surfaces are known.

The same semitransparent multilayered sample above may be also illuminated by a modulated focused laser beam of Gaussian profile of radius a (at $1/e^2$ of the

intensity). For each layer the heat source writes $Q_i = \frac{2P_i e^{-(2r^2/a^2)}}{\pi a^2} \alpha_i e^{-\alpha_i(z - z_i)}$, where P_i

is the incident power reaching layer i , which in the absence of reflection is given by

$$P_i = P_0 e^{-(\alpha_1 \ell_1 + \alpha_2 \ell_2 + \dots + \alpha_{i-1} \ell_{i-1})}.$$

As it was checked in Chapter 2, by working in the Haenkel space for the focused illumination, where the temperature $T_i(r, z) = \int_0^\infty \delta J_o(\delta r) \bar{T}_i(\delta, z) d\delta$, it becomes easy to obtain the temperature for focused illumination out of the temperature for the plane case. Thus, with the changes summarized in Table 2.1, the Hankel transform of the temperature and the normal heat flux, provided the equations (4.6) result:

$$\bar{T}_i(\delta, z) = A'_i \text{Sinh}[\beta_i(z - z_i)] + B'_i \text{Cosh}[\beta_i(z - z_i)] + C'_i e^{-\alpha_i(z - z_i)} \quad (4.8)$$

$$\bar{\phi}_i(\delta, z) = -K_i \frac{d\bar{T}_i}{dz} = -K_i \beta_i \{ A'_i \text{Cosh}[\beta_i(z - z_i)] + B'_i \text{Sinh}[\beta_i(z - z_i)] \} + K_i C'_i \alpha_i e^{-\alpha_i(z - z_i)}$$

where $\beta_i^2 = \sigma_i^2 + \delta^2$.

Hence, a matrix relationship between the Hankel transforms of the temperature and heat flux at both front (z_i) and rear (z_{i+1}) surfaces of layer i is obtained:

$$\begin{pmatrix} \bar{T}_i(\delta, z_i) \\ \bar{\phi}_i(\delta, z_i) \end{pmatrix} = \begin{pmatrix} a'_i & b'_i \\ c'_i & d'_i \end{pmatrix} \begin{pmatrix} \bar{T}_i(\delta, z_{i+1}) - X'_i \\ \bar{\phi}_i(\delta, z_{i+1}) - Y'_i \end{pmatrix} \quad (4.9)$$

where $a'_i = d'_i = \text{Cosh}(\beta_i \ell_i)$, $b'_i = \frac{\text{Sinh}(\beta_i \ell_i)}{K_i \beta_i}$, $c'_i = K_i \beta_i \text{Sinh}(\beta_i \ell_i)$,

$$X'_i = C'_i \left[\frac{\alpha_i}{\beta_i} \text{Sinh}(\beta_i \ell_i) - \text{Cosh}(\beta_i \ell_i) + e^{-\alpha_i \ell_i} \right] \text{ and}$$

$$Y'_i = C'_i K_i \left[\beta_i \text{Sinh}(\beta_i \ell_i) - \alpha_i \text{Cosh}(\beta_i \ell_i) + \alpha_i e^{-\alpha_i \ell_i} \right].$$

The same way as for plane, if the sample is opaque $X'_i = Y'_i = 0$, the model in Section 2.5 is obtained. Also, according to the equation (4.9), the Hankel transform of the temperatures at the front and rear surfaces are obtained provided the Hankel transforms of the normal heat fluxes are known.

For an anisotropic sample, for which the heat propagation is three-dimensional, one can proceed in a similar way but using the Fourier transform instead of the Hankel transform, as in Section 3.2.1.B.

Focusing on the case of plane illumination, it may be simplified the equation (4.7) and expressed as

$$H_i = M_i (O_i - P_i) \quad (4.10)$$

where H_i is the input matrix, O_i is the output matrix, M_i is the thermal matrix and P_i is optical matrix.

To obtain a single matrix equation relating temperature and heat flux at the front ($z = z_1 = 0$) and rear ($z = z_{N+1} = \ell$) surfaces we need to know the relationship between temperature and heat flux at each intermediate boundary. Two possibilities are considered:

(1) If there is a perfect thermal contact between the layers, temperature and heat flux continuity can be applied: $T_i(z_{i+1}) = T_{i+1}(z_{i+1})$ and $\phi_i(z_{i+1}) = \phi_{i+1}(z_{i+1})$, and therefore $O_i = H_{i+1}$. By applying this equation to each layer we obtain

$$H_1 = \mathbb{Z}_N O_N - \sum_{p=1}^N \mathbb{Z}_p P_p \quad (4.11)$$

where $\mathbb{Z}_p = \prod_{i=1}^p M_i$, $H_1 = \begin{pmatrix} T_1(0) \\ \phi_1(0) \end{pmatrix}$ and $O_N = \begin{pmatrix} T_N(\ell) \\ \phi_N(\ell) \end{pmatrix}$.

If heat losses are negligible: $\phi_1(0) = \phi_N(\ell) = 0$

(2) A thermal resistance $R_{i,i+1}$ is introduced to account for the lack of adherence between the layers i and $i+1$. This means that the heat flux continuity still holds but there is a jump in temperature given by $T_i(z_{i+1}) = T_{i+1}(z_{i+1}) + R_{i,i+1} \phi_{i+1}(z_{i+1})$,

and therefore $O_i = \mathfrak{R}_{i,i+1} H_{i+1}$, where $\mathfrak{R}_{i,i+1} = \begin{pmatrix} 1 & R_{i,i+1} \\ 0 & 1 \end{pmatrix}$. This means that the matrix equation relating temperature and heat flux at the front ($z = 0$) and rear ($z = \ell$) surfaces is similar to the equation (4.11) but changing \mathbb{Z}_p , that is product of the thermal matrices, by $\mathbb{Z}'_p = M_1 \mathfrak{R}_{1,2} M_2 \mathfrak{R}_{2,3} M_3 \dots M_{p-1} \mathfrak{R}_{p-1,p} M_p$. Hence,

$$H_1 = \mathbb{Z}'_N O_N - \sum_{p=1}^N \mathbb{Z}'_p P_p \quad (4.12)$$

4.2.3. Effects to consider

It is worth studying some additional effects that modify the temperature distribution inside the sample and/or the signal recorded by the infrared detector in a modulated PTR experiment. Among them, let us pay special attention to heat losses, multiple reflexions of the incident light, transparency of the samples to the infrared and lateral heat diffusion.

A. Heat losses

As it was done in Section 2.5, it is easy to consider heat losses in terms of quadrupoles, as in equation (2.50). For the simple case of a semitransparent sheet of thickness ℓ illuminated by a modulated plane light beam of intensity I_o :

If the sample is adiabatically isolated from its surroundings, $\phi(0) = \phi(\ell) = 0$, the matrix expression relating the temperature at the sample surfaces writes

$$\begin{pmatrix} T(0) \\ 0 \end{pmatrix} = \begin{pmatrix} a & b \\ c & d \end{pmatrix} \begin{pmatrix} T(\ell) - X \\ 0 - Y \end{pmatrix} \quad (4.13)$$

If heat losses are present, the heat fluxes at the front and rear surfaces are respectively: $\phi(0) = -h_f T(0) - K_g \sigma_g T(0)$ and $\phi(\ell) = h_r T(\ell) + K_g \sigma_g T(\ell)$, where h_f

and h_r are the combined heat transfer coefficients by radiation and convection at the front and rear surfaces, respectively. The last term in each expression is the heat flux by conduction to the surrounding gas, which is proportional to the surface temperature since the gas is considered infinitely thick. According to the equation (4.7) the matrix expression relating the temperatures at the surfaces can be written as

$$\begin{pmatrix} T(0) \\ 0 \end{pmatrix} = \begin{pmatrix} 1 & 0 \\ h_f & 1 \end{pmatrix} \begin{pmatrix} 1 & 0 \\ K_g \sigma_g & 1 \end{pmatrix} \begin{pmatrix} a & b \\ c & d \end{pmatrix} \begin{pmatrix} 1 & 0 \\ K_g \sigma_g & 1 \end{pmatrix} \begin{pmatrix} 1 & 0 \\ h_r & 1 \end{pmatrix} \begin{pmatrix} T(\ell) \\ 0 \end{pmatrix} - \begin{pmatrix} 1 & 0 \\ h_f & 1 \end{pmatrix} \begin{pmatrix} 1 & 0 \\ K_g \sigma_g & 1 \end{pmatrix} \begin{pmatrix} a & b \\ c & d \end{pmatrix} \begin{pmatrix} X \\ Y \end{pmatrix} \quad (4.14)$$

where subscript g stands for the surrounding gas. As can be seen, the influence of conduction to the gas and convection and radiation are separated in independent matrices.

Figure 4.6 and 4.7 show the influence of heat losses on the surface temperature, for two different normalization procedures: the selected self-normalization and normalization with a reference. For all the simulations the following parameters have been used: $D_g = 22 \text{ mm}^2/\text{s}$, $K_g = 0.026 \text{ W/mK}$, and $h_f = h_r = 15 \text{ W/m}^2\text{K}$, which is a good upper estimation for room temperature measurements [68].

In the case of self-normalization the ratio of the front and rear surface temperatures is considered: $T_n = T(\ell)/T(0)$. This is a suitable method for thin sheets. In Figure 4.6 the natural logarithm of the self-normalized temperature amplitude, $\text{Ln}(T_n)$, and its phase, $\Psi(T_n)$, are plotted against \sqrt{f} . Simulations have been performed for a semitransparent sheet with the following parameters: $D = 0.5 \text{ mm}^2/\text{s}$, $K = 1.0 \text{ W/mK}$, $\ell = 0.5 \text{ mm}$, and $\alpha = 3 \text{ mm}^{-1}$. Blue lines correspond to the effect of heat losses. As it is well known, the effect of heat losses is stronger at low frequencies and for poor thermal conductors [69]. However, in self-normalization both $\text{Ln}(T_n)$ and $\Psi(T_n)$ converge to zero at low frequencies and, therefore, the effect of heat losses becomes almost negligible.

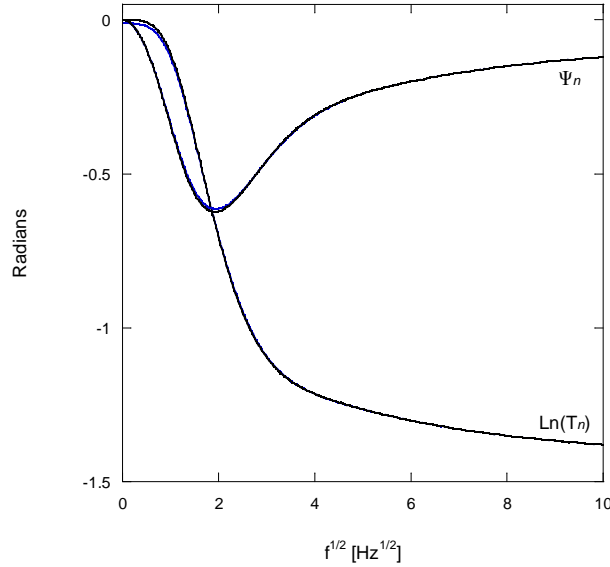


Figure 4.6: Simulations of the self-normalized temperature as a function of the square root of the frequency for a sheet with $D = 0.5 \text{ mm}^2/\text{s}$, $K = 1.0 \text{ W/mK}$, $\ell = 0.5 \text{ mm}$, and $\alpha = 3 \text{ mm}^{-1}$. Black lines correspond to the absence of heat losses. Blue lines stand for the effect of heat losses with $h_f = h_r = 15 \text{ W/m}^2\text{K}$.

The second normalization procedure consists on comparing the sample temperature at the front surface with that of a reference: $T'_n = T(0) / T_{ref}(0)$. In black lines in Figure 4.7, a very thick opaque sheet with $D = 1.0 \text{ mm}^2/\text{s}$, $K = 2.5 \text{ W/mK}$ is compared with a very thick and opaque reference sample of $D_{ref} = 0.5 \text{ mm}^2/\text{s}$ and $K_{ref} = 1.0 \text{ W/mK}$. The dotted lines correspond to the deviation due to heat losses. As can be seen, only at frequencies below 0.1 Hz must the influence of heat losses be taken into account. Note that in absence of heat losses the amplitude of T'_n is equal to $e_{ref}/e = 0.566$, where $e = K / \sqrt{D}$ is the thermal effusivity, and $\Psi(T'_n) = 0$. This means that, if the sample and the reference are thermally thick, only the thermal effusivity of the sample can be obtained.

In red lines of Figure 4.7, we show the same calculations as in black lines, but $\ell_{ref} = \ell = 1 \text{ mm}$. As before the dotted lines indicate the effect of heat losses, which are negligible above 0.1 Hz. Note that the amplitude of T'_n converges to $e_{ref}/e = 0.566$ at

high frequencies, and to $(\rho c \ell)_{ref} / (\rho c \ell) = 0.80$ at low frequencies, where $\rho c = K / D$ is the heat capacity. In its turn, $\Psi(T_n')$ converges to zero, both at low and high frequencies. From the shape of the normalized temperature at intermediate frequencies, both D and K can be retrieved.

Finally, in blue lines, we show the same calculations as in red, but for semitransparent sample and reference, with $\alpha_{ref} = \alpha = 3 \text{ mm}^{-1}$. As can be seen, the information on the optical properties appears at frequencies higher than 0.1 Hz, where the effect of heat losses is negligible.

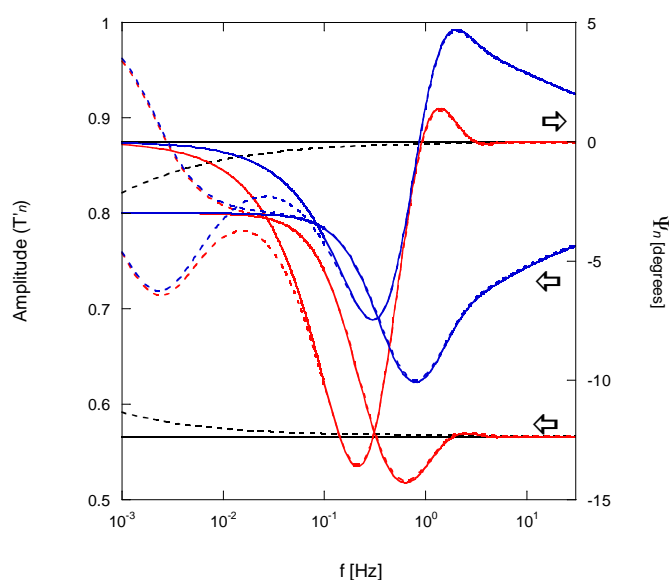


Figure 4.7: Simulations of the normalized temperature with a reference with the following data: $D_{ref} = 0.5 \text{ mm}^2/\text{s}$, $K_{ref} = 1.0 \text{ W/mK}$, $D = 1.0 \text{ mm}^2/\text{s}$, $K = 2.5 \text{ W/mK}$. In black, both are opaque and thick; in red, both are opaque and $\ell_{ref} = \ell = 1 \text{ mm}$; and in blue, both are semitransparent $\alpha_{ref} = \alpha = 3 \text{ mm}^{-1}$ and $\ell_{ref} = \ell = 1 \text{ mm}$. Solid lines correspond to the absence of heat losses, while dotted lines stand for the effect of heat losses with $h_f = h_r = 15 \text{ W/m}^2\text{K}$.

As the effect of heat losses is only significant below 0.1 Hz and most experimental measurements with modulated PTR are performed at frequencies above this limit, heat losses will not be considered in the remaining of the Chapter.

B. Multiple reflections of the incident light

If the light incident light crossing the sample reaches the rear surface before vanishing it will be reflected back and forth contributing to increase the sample temperature. Accounting for the multiple reflections of the light beam inside the sheet of thickness ℓ , the intensity distribution can be written as

$$I(z) = \frac{I_o(1-R)(e^{-\alpha z} + R e^{-2\alpha\ell} e^{\alpha z})}{1 - R^2 e^{-2\alpha\ell}} \quad (4.15)$$

Then, proceeding as in reference [64], the sample temperature is obtained

$$T(z) = \frac{I_o(1-R)\alpha^2}{2K\sigma(\sigma^2 - \alpha^2)} \left[\frac{(e^{-\alpha\ell} - e^{-\sigma\ell})e^{\sigma z} + (e^{-\alpha\ell} - e^{\sigma\ell})e^{-\sigma z} + \frac{\sigma}{\alpha}(e^{\sigma\ell} - e^{-\sigma\ell})e^{-\alpha z}}{e^{\sigma\ell} - e^{-\sigma\ell}} \right] - \frac{I_o(1-R)\alpha^2 R e^{-2\alpha\ell}}{2K\sigma(\sigma^2 - \alpha^2)} \left[\frac{(e^{-\sigma\ell} - e^{\alpha\ell})e^{\sigma z} + (e^{\sigma\ell} - e^{\alpha\ell})e^{-\sigma z} + \frac{\sigma}{\alpha}(e^{\sigma\ell} - e^{-\sigma\ell})e^{\alpha z}}{e^{\sigma\ell} - e^{-\sigma\ell}} \right] \quad (4.16)$$

where the second term is the correction with respect to the equation (4.1). Note that when $\ell \rightarrow \infty$ the equation (4.15) reduces to equation (4.1) since $e^{-2\alpha\ell} \rightarrow 0$. From the equation (4.16) the normalized temperature $T_n = T(\ell)/T(0)$ is obtained. In Figure 4.8 we show the effect of multiple reflections on the normalized temperature for the same glass sheet of Figure 4.2, with $R = 0.04$ (corresponding to normal incidence on a typical glass with a refraction index of 1.5) and $\alpha = 2 \text{ mm}^{-1}$, i.e. $\alpha\ell = 1$. Although the contribution of the multiple reflections is small, it should be taken into account in order to retrieve accurate α and D values. However, numerical simulations indicate that this effect is significant only for samples with $\alpha\ell < 2$.

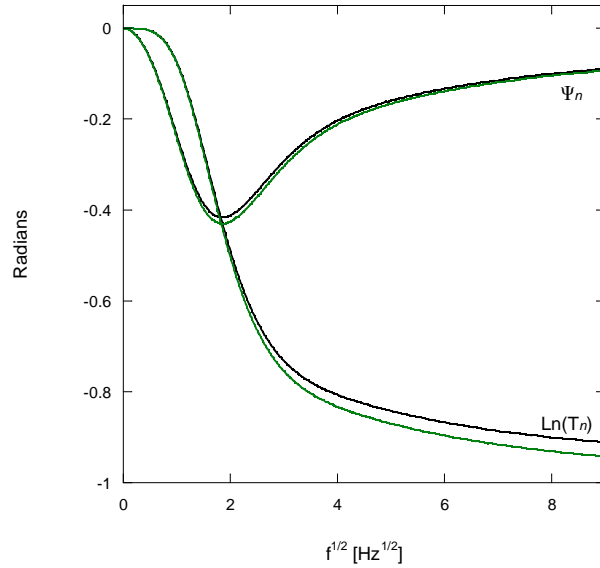


Figure 4.8: Simulations of $\text{Ln}(T_n)$ and $\Psi(T_n)$ as a function of \sqrt{f} for a glass sheet of $D = 0.5 \text{ mm}^2/\text{s}$, $\ell = 0.5 \text{ mm}$, $R = 0.04$ and $\alpha = 2 \text{ mm}^{-1}$. Black lines correspond to the simulations without multiple reflections and green lines to those with multiple reflections of the exciting light beam.

C. Transparency to the infrared radiation

The modulated voltage produced by the infrared detector is proportional to the oscillating surface temperature only if the sample is completely opaque to the infrared wavelengths (in the case of HgCdTe detectors from 2 to 12 μm). This condition is fulfilled for metals and alloys, but not for most glasses and polymers. Actually, the visual appearance is not a reference to predict the infrared behaviour. For instance, Ge is opaque for visible wavelengths, but completely transparent above 2 μm . Besides, some metallic oxides look black but they are translucent at infrared wavelengths. In consequence, it is necessary to evaluate the influence of the transparency to the infrared wavelengths on the measured voltage.

If the sample is semitransparent to the infrared spectrum the signal recorded by the infrared detector comes, not only from the sample surface, but from the whole sample thickness. If we define β_{IR} as the effective infrared absorption coefficient for the sample (averaging the sample behaviour from 2 to 12 μm) [70] the signal recorded by the detector placed in front of the illuminated surface is given by [71]

$$S(0) = C \int_0^\ell \beta_{IR} e^{-\beta_{IR} z} T(z) dz \quad (4.17)$$

where C is a constant including the emissivity of the sample, the sensor area and detectivity, and the temperature derivative of the Plank function at room temperature. $T(z)$ is the sheet temperature given by the equation (4.1). This means that we are assuming that heat losses associated to the infrared emission from the sample are so small that they do not affect the temperature field (note that this assumption holds for the oscillating temperature, but not for the dc temperature rise of the sheet, which is highly limited by heat losses [72]). Similarly, the signal recorded by the detector placed in front of the non-illuminated surface is given by

$$S(\ell) = C \int_0^\ell \beta_{IR} e^{\beta_{IR}(z-\ell)} T(z) dz \quad (4.18)$$

By substituting equation (4.1) into equations (4.17) and (4.18) and solving the integrals analytically, the normalized signal is obtained

$$S_n = \frac{S(\ell)}{S(0)} = \frac{A}{B} e^{-\beta_{IR} \ell} \quad (4.19)$$

where A and B are given by

$$A = \frac{e^{-\alpha \ell} - e^{-\sigma \ell}}{-(\sigma + \beta_{IR})} \left(1 - e^{(\sigma + \beta_{IR}) \ell}\right) + \frac{e^{-\alpha \ell} - e^{\sigma \ell}}{\sigma - \beta_{IR}} \left(1 - e^{(\beta_{IR} - \sigma) \ell}\right) + \frac{\sigma}{\alpha} \frac{e^{\sigma \ell} - e^{-\sigma \ell}}{\alpha - \beta_{IR}} \left(1 - e^{(\beta_{IR} - \alpha) \ell}\right)$$

$$B = \frac{e^{-\alpha \ell} - e^{-\sigma \ell}}{\beta_{IR} - \sigma} \left(1 - e^{(\sigma - \beta_{IR}) \ell}\right) + \frac{e^{-\alpha \ell} - e^{\sigma \ell}}{\sigma + \beta_{IR}} \left(1 - e^{-(\sigma + \beta_{IR}) \ell}\right) + \frac{\sigma}{\alpha} \frac{e^{\sigma \ell} - e^{-\sigma \ell}}{\alpha + \beta_{IR}} \left(1 - e^{-(\alpha + \beta_{IR}) \ell}\right)$$

In Figure 4.9 it is shown the effect of the infrared transparency on the normalized signal S_n for the same glass sheet of Figure 4.2, with $\alpha = 5 \text{ mm}^{-1}$ and different values of β_{IR} ranging from 0 to ∞ . Note that, even for an almost IR opaque material, with β_{IR} values around 30 mm^{-1} , its influence on S_n is not negligible, mainly at the high frequency tail, and therefore equation (4.19) must be used instead of equation (4.2).

It is interesting to point out that when exchanging the α and β_{IR} values the normalized signal S_n remains the same.

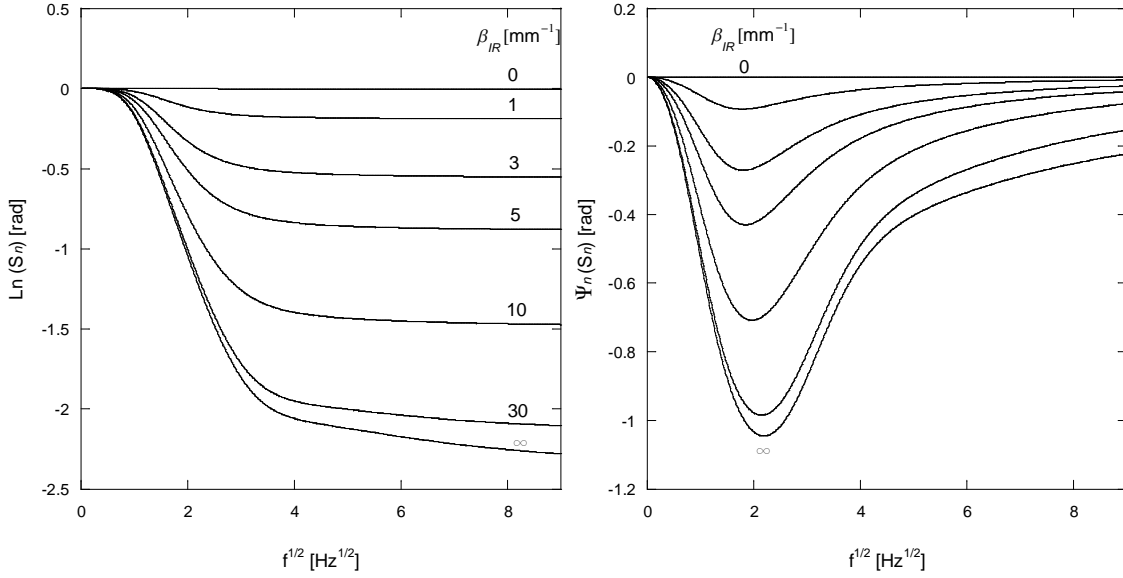


Figure 4.9: Simulations of $\text{Ln}(S_n)$ (left) and $\Psi(S_n)$ (right) as a function of \sqrt{f} for a glass sheet with $D = 0.5 \text{ mm}^2/\text{s}$, $\ell = 0.5 \text{ mm}$, $R = 0.04$ and $\alpha = 5 \text{ mm}^{-1}$, and different values of β_{IR} ranging from 0 (transparent to IR) to ∞ (opaque to IR).

So as to fit the experimental data a theoretical expression of the normalized PTR signal combining the multiple reflections of the incident light and the transparency to the IR radiation will be used

$$S_n = \frac{S(\ell)}{S(0)} = \frac{A + R e^{-2\alpha\ell}}{B + R e^{-2\alpha\ell}} \frac{A1}{B1} e^{-\beta_{IR}\ell} \quad (4.20)$$

where $A1$ and $B1$ are given by

$$A1 = \frac{e^{\alpha\ell} - e^{-\sigma\ell}}{-(\sigma + \beta_{IR})} (1 - e^{(\sigma + \beta_{IR})\ell}) + \frac{e^{\alpha\ell} - e^{\sigma\ell}}{\sigma - \beta_{IR}} (1 - e^{(\beta_{IR} - \sigma)\ell}) + \frac{\sigma}{\alpha} \frac{e^{\sigma\ell} - e^{-\sigma\ell}}{\alpha + \beta_{IR}} (1 - e^{(\alpha + \beta_{IR})\ell})$$

$$B1 = \frac{e^{\alpha\ell} - e^{-\sigma\ell}}{\beta_{IR} - \sigma} (1 - e^{(\sigma - \beta_{IR})\ell}) + \frac{e^{\alpha\ell} - e^{\sigma\ell}}{\sigma + \beta_{IR}} (1 - e^{-(\sigma + \beta_{IR})\ell}) + \frac{\sigma}{\alpha} \frac{e^{\sigma\ell} - e^{-\sigma\ell}}{\alpha - \beta_{IR}} (1 - e^{(\alpha - \beta_{IR})\ell})$$

D. Lateral heat diffusion

Experimentally speaking, it is usual to use a defocused Gaussian laser beam to simulate a plane beam. But to approve the approximation, it becomes important to quantify the effect of using a Gaussian laser beam instead of a completely flat light source, i.e. the disturbing effect of 2-D heat propagation. Simulations are performed for a stainless steel slab ($D = 4.0 \text{ mm}^2/\text{s}$, $K = 15.0 \text{ W/mK}$, $\ell = 1.0 \text{ mm}$), considering two cases: the self-normalization measurement, and normalization with a reference.

In Figure 4.10 left, it is shown the self-normalized amplitude and phase as a function of the square root of the frequency. Black lines correspond to a plane light beam and green lines to a Gaussian beam with $a = 5 \text{ mm}$. As can be seen, the influence of the lateral heat diffusion in the slopes, and therefore, in the thermal diffusivity of the steel sample is almost negligible.

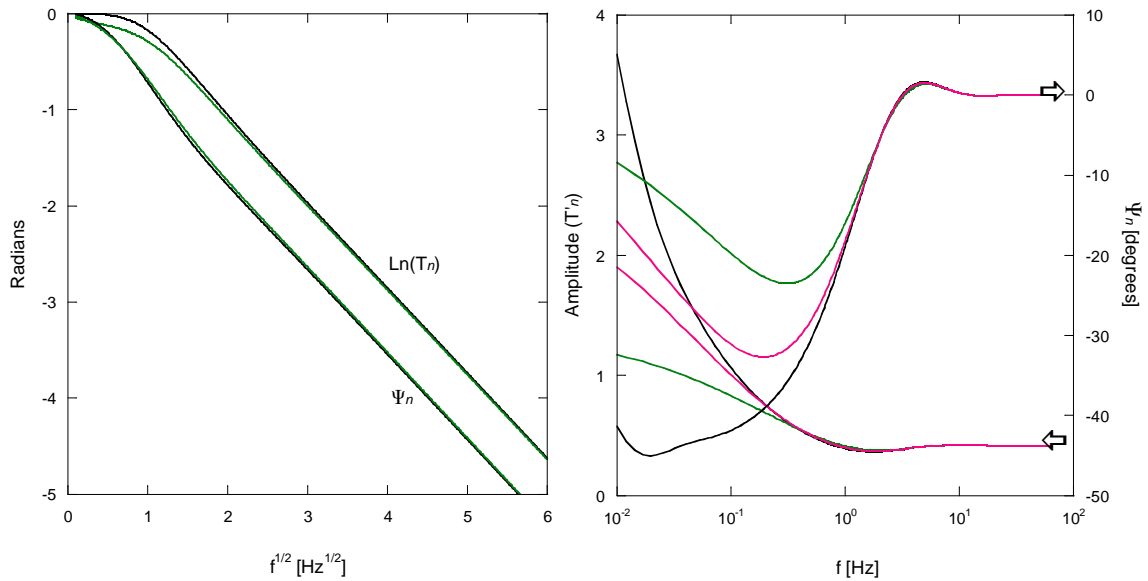


Figure 4.10: Influence of the laser spot size on the normalized temperature for a stainless steel slab ($D = 4.0 \text{ mm}^2/\text{s}$, $K = 15.0 \text{ W/mK}$, $\ell = 1.0 \text{ mm}$). On the left, self-normalized temperature and on the right, normalization with reference (vitreous carbon: $D = 6.0 \text{ mm}^2/\text{s}$, $K = 6.3 \text{ W/mK}$, $\ell = \infty$). The laser beam radius is $a = \infty$ (plane beam, black lines), $a = 10 \text{ mm}$ (pink lines), $a = 5 \text{ mm}$ (green lines).

In Figure 4.10 right, it is shown the result of the normalization of the steel sample with a reference made of vitreous carbon ($D = 6.0 \text{ mm}^2/\text{s}$, $K = 6.3 \text{ W/mK}$, $\ell = \infty$). Black lines stand for a plane light beam, pink lines for $a = 10 \text{ mm}$ and green lines for $a = 5 \text{ mm}$. Now, the influence of lateral heat diffusion is not negligible, and to retrieve the thermal properties of the steel sample accurately, the size of the laser spot must be included in the fitting procedure.

It is clear then, that selecting the self-normalization method is a good choice, not only for providing the highest signal to noise ratio and amplitude and phase contrast, but also for avoiding having to take into account the effect of heat losses and lateral heat diffusion on the PTR measurements.

4.3. Experimental setup

This chapter focuses on the thermal and optical characterization of semitransparent samples. By exciting them with a plane light beam, the in-depth properties can be studied. Thus, with the aim of measuring at the same time thermal diffusivity (D) and optical absorption coefficient (α), a photothermal radiometry (PTR) set up is used.

It is shown in Figure 4.11 a general scheme. The sample is excited by means of a modulated laser beam defocused to reproduce a plane source. Then, the light is absorbed either at the surface or inside of the sample and a thermal wave is generated. That thermal wave is propagated through the material and, at the end, infrared radiation is emitted from the surface. The infrared radiation is collected by a system of mirrors and focused into a single detector, as it is photothermal radiometry. Then, the signal is preamplified and the information fed into a lock-in amplifier, which demodulates it to provide the amplitude and phase data of the sample surface temperature. As can be observed, two possible excitations are considered, corresponding to front and rear surfaces. For normalization purposes, self-normalization, both must be performed.

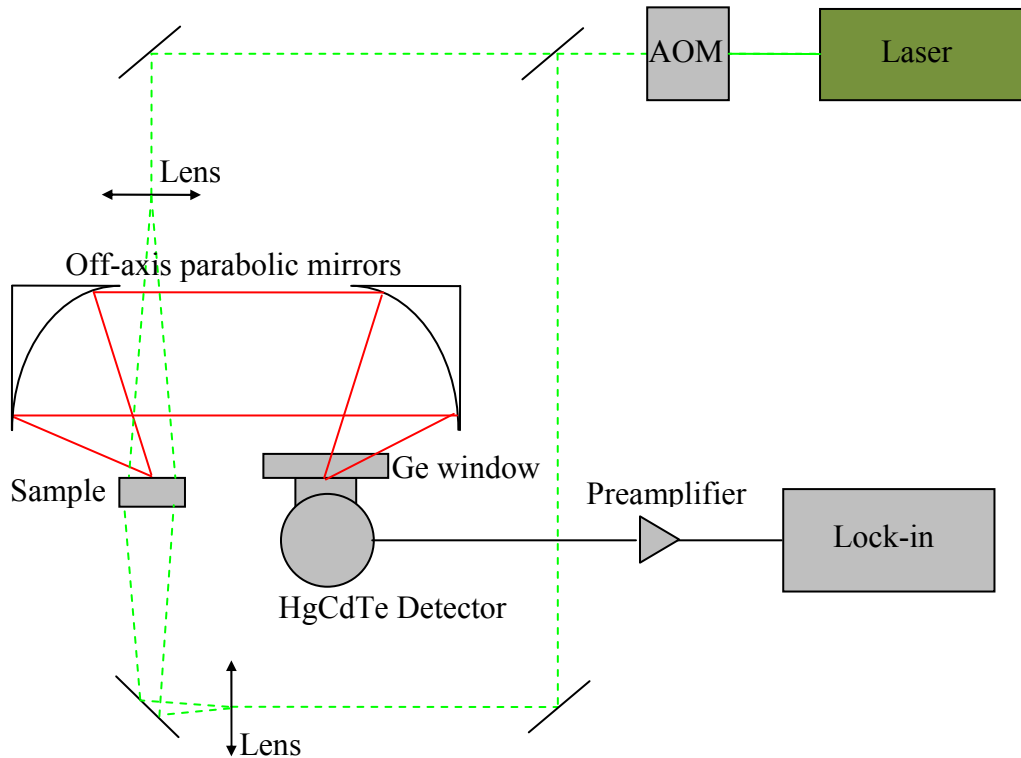


Figure 4.11: General scheme of the experimental setup.

In Figure 4.12 we may see a photo of the experimental PTR setup in the laboratory, with the components labelled and explained below.

The heating source is the same as the one used in photothermal thermography for thin films and filaments in Chapter 3, a 532 nm frequency doubled Nd:YAG laser modulated by an acousto-optic modulator. The sample is excited, either the front or the rear surface, by a plane beam. For that, the laser beam is expanded by a spherical lens to a diameter of at least 1 cm, to guarantee 1D heat propagation.

The infrared radiation emitted from the sample is collected with the system shown in Figure 4.13. A 60° gold coated off-axis parabolic mirror collects the infrared radiation emitted from a point in the surface of the sample, the focal point of the mirror, and directs the radiation through the other mirror to a cooled HgCdTe sensor, located at the focal point the mirror. The sensor provides a detection waveband from

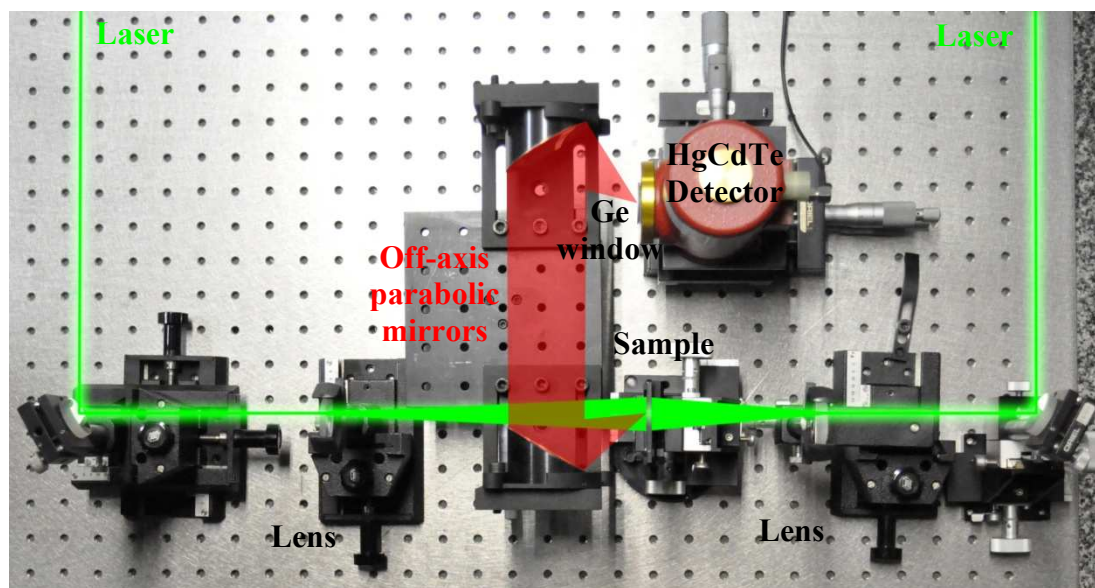


Figure 4.12: Photo of the set up in the laboratory.

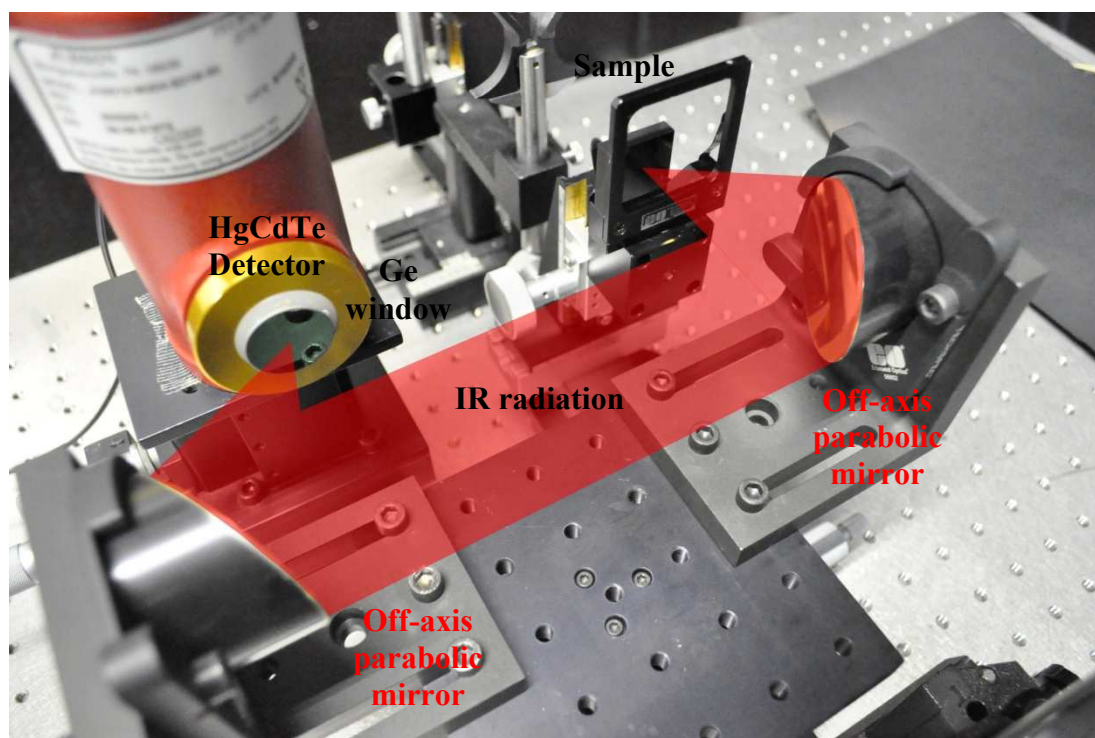


Figure 4.13: Zoom on the radiation collecting system.

2 to 12 μm . An active area of 1 mm^2 has been chosen since it has the highest product detectivity \times area. A Ge window, which is opaque to visible wavelengths but

transparent from 2 to 12 μm is usually placed in front of the detector to prevent the green light of the laser from reaching the IR sensor, but here, a Ge based spectral filter has been used to reduce the transmission region of the detector to the waveband 5 to 12 μm , as some studied filter samples are semitransparent between 2 and 5 μm . Next, the voltage produced by the detector is preamplified and fed into a digital lock-in amplifier connected to a PC. Representations of the amplitude and phase of the signal as a function of the modulation frequency let us retrieve thermal and optical properties of the samples.

In PTR, where the signal is recorded as a function of the frequency, it becomes necessary to normalize the measurements in order to suppress the instrumental factor, i.e., the dependence of the detection electronics on the frequency. As it was introduced before, self-normalization is selected for our purposes, as it provides the highest signal to noise ratio and amplitude and phase contrast.

On the other hand, several authors have pointed out that the measured PTR voltage is affected by coherent noise generated by stray-light heating the IR optics and cut off filter [73-75]. However, they experimentally showed that this effect is only significant for modulation frequencies exceeding 1 kHz. As all the measurements in this work have been performed at frequencies far below this value, this coherent noise has not been considered.

4.4. Results and discussion

With the aim of testing the ability of PTR to retrieve simultaneously and accurately both optical absorption coefficient α and thermal diffusivity D of semitransparent samples, a large collection of measurements have been performed on samples of all optical possibilities: opaque to visible and IR wavelengths, opaque to visible but semitransparent to IR, semitransparent to visible but opaque to IR and semitransparent to visible and IR. The results establish the conditions and limits to perform simultaneous accurate α and D measurements by modulated PTR.

Furthermore, semitransparent multilayer samples are also considered, and measurements on two applications are presented. One of them shows the effect of paint layers on the PTR measurements and the other presents the possibility to characterize thermal contact resistances between layers.

All of the measurements have been performed under the self-normalization procedure, since as well as providing the highest signal to noise ratio and amplitude and phase contrast, it makes negligible the effect of heat losses and lateral heat diffusion on the PTR measurements.

4.4.1. Homogeneous solids

In order to verify the ability of modulated PTR to characterize the thermal diffusivity and the optical absorption coefficient of homogenous solids we have performed measurements on a wide set of samples, which are summarized in Figure 4.14 according to their optical properties and so, to the parameters available from PTR measurements.

	IR Opaque	IR Semitransparent	IR Transparent
Visible Opaque	Ni Porous SiC Vitreous carbon AISI-304 CFR composite PLLA composite	LaMnO ₃ NiO Cr ₂ O ₃ CoO Si	Ge ZnSe
	D	D β_{IR}	No contrast
Visible Semitransparent	ND filters Paper	Coloured filters PEEK polymer	PLLA polymer
	D α	D α β_{IR}	No contrast
Visible Transparent	BK7 glass	MgF ₂ Sapphire	CaF ₂
	No signal	No signal	No signal

Figure 4.14: Optical classification of the materials measured in this work.

Multiple reflections of the incident light and transparency to the infrared radiation are by no means negligible, so all the measurements have been performed taking them into consideration.

Figure 4.15 presents the experimental results for all the cases. In Figure 4.15 the upper left graph, results for two samples are shown, vitreous carbon and carbon fiber reinforced (CFR) composite, both opaque to visible and IR wavelengths. As can be seen, both $\text{Ln}(S_n)$ (solid squares) and $\Psi(S_n)$ (open squares) are parallel straight lines as a function of \sqrt{f} , except at low frequencies where the material is thermally thin.

In Table 4.1 we may see the thermal diffusivity values obtained from the slopes using the expression $m = -\ell\sqrt{\pi/D}$ for Ni, SiC (38% porosity), vitreous carbon, AISI-304 stainless steel, CFR composite and PLLA composite. They are in good agreement with literature values. In this case, there are three reliability criteria when applying this method to retrieve the diffusivity value:

- (1) The parallelism of both straight lines.
- (2) The fit of the phase converging to 0 radians at $f = 0$ Hz.
- (3) The large range of linear behaviour (about 5-6 radians) before noise appears.

The thermal diffusivity underestimation for Ni and AISI-304 is due to the painting layers used to increase both the absorption of the laser light and the IR emission. The effect of these layers will be discussed later under the thermal quadrupoles method.

The experimental result of a Ge slab 3 mm thick is also shown in this graph. As this material is completely transparent at IR wavelengths, $\Psi(S_n)$ is zero for all frequencies. However, $\text{Ln}(S_n)$ is not zero, as it should be according to the theoretical model, but a constant value due to the different light intensity absorbed at both surfaces. No information on the thermal and optical properties of this material can be obtained.

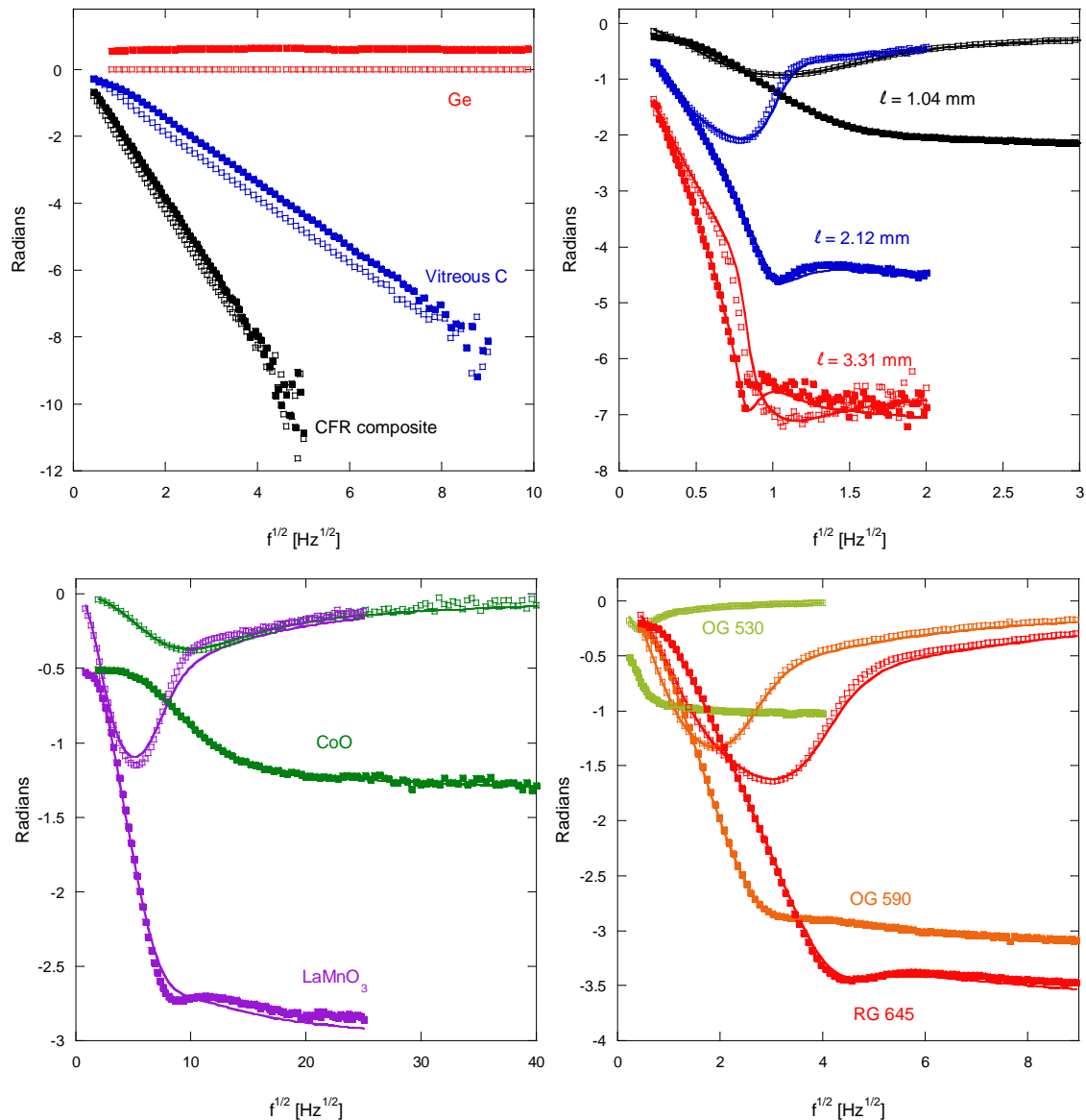


Figure 4.15: Experimental values of $\text{Ln}(S_n)$ (solid squares) and $\Psi(S_n)$ (open squares) for materials with different optical properties. Up on the left, visible and IR opaque samples, together with Ge that is transparent to IR. Up on the right, a neutral density filter, opaque to IR, with three different thicknesses. Down on the left, LaMnO_3 and CoO , which are opaque to visible but semitransparent to IR. Down on the right, coloured filters, which are semitransparent to visible and IR wavelengths. Continuous lines are the fittings to the equation (4.20).

In Figure 4.15 the upper right graph, experimental results are presented for a neutral density filter of $\alpha = 2.33 \text{ mm}^{-1}$ at 532 nm (Cary spectrometer) which is opaque to IR wavelengths above $5 \mu\text{m}$. Three sheets of different thicknesses have been measured to test the reliability of the results. Continuous lines are the fittings to the equation

(4.20). The same D and α values for the three samples are obtained (see Table 4.1) inside the experimental uncertainty (5% and 10% respectively). The data in this graph indicate that if the sample is quite thick, the phase contrast is high but the signal to noise ratio is poor (noisy data), since the PTR voltage from the rear illumination measurements is very small (a few tens of μV). On the contrary, if the sample is too thin, the signal to noise ratio is high (noise free data), but the phase contrast is small (less than 1 rad in phase). In consequence, whenever the thickness of the sample under study can be selected, an intermediate thickness providing a good enough signal to noise ratio together with a quite high phase contrast (about 2 radians) is the best choice.

The graph down on the left refers to the experimental results for two metallic oxides, LaMnO_3 and CoO , which are completely black, i.e. opaque to visible wavelengths. However, the shape of $\text{Ln}(S_n)$ (solid squares) and $\Psi(S_n)$ (open squares) indicates that these materials are semitransparent to IR wavelengths. The results of the fittings are shown in Table 4.1. The retrieved D values agree with the measurements performed using a photopyroelectric setup [76, 77].

Finally, measurements on six coloured filters with increasingly optical absorption coefficient at 532 nm have been also performed. The main difference with respect to the neutral density filters is that they are not completely opaque to IR wavelengths, so the experimental data must be fitted to the equation (4.20) with three unknowns: D , α and β_{IR} . The results of the fittings are shown in Table 4.1, while the experimental results for three of them are plotted in Figure 4.15 down on the right. Note that for OG530, which is very transparent at 532 nm, it is used a quite thick sheet (2.20 mm) in order to increase the phase contrast as much as possible while keeping a good enough signal to noise ratio. Anyway, this sample is placed in the lowest limit of this method ($\alpha\ell \approx 0.8$). This is why the retrieved α value is the least accurate. However, it is worth noting that the D value is the same as for the other filters of the family, indicating that thermal diffusivity is obtained with higher accuracy than the optical absorption coefficient.

Figure 4.16 left presents the experimental PTR data for a composite material whose matrix is poly-L-lactide (PLLA) and the fillers are carbon nanotubes (0.75%). As can be seen, both $\text{Ln}(S_n)$ (solid squares) and $\Psi(S_n)$ (open squares) become flat at high frequencies, indicating that the sample is not completely opaque (i.e. it falls in the region $10 < \alpha l < 30$). However, a good fitting to the equation (4.20) cannot be obtained since the high frequency data are too noisy. According to the theory only the slope of $\text{Ln}(S_n)$ has been used to retrieve D , whose value is given in Table 4.1.

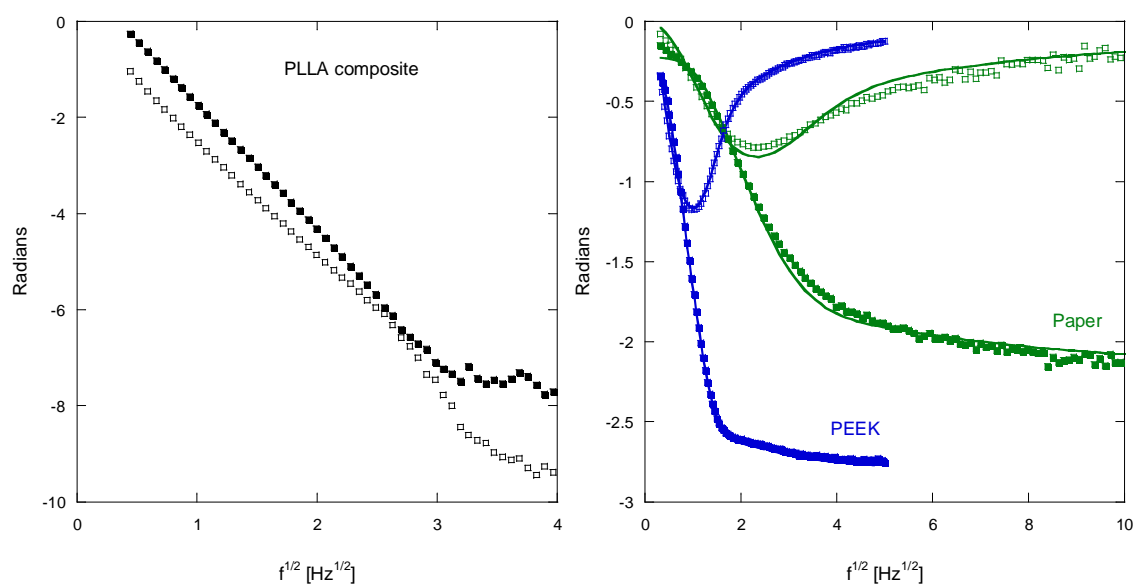


Figure 4.16: Experimental values of $\text{Ln}(S_n)$ (solid squares) and $\Psi(S_n)$ (open squares) for: Left, PLLA composite with 0.75% of carbon nanotubes, and Right, white paper and PEEK polymer.

In materials like paper or polyether-ether-ketone (PEEK) there is not only light absorption, but light scattering as well. Accordingly, the Beer-Lambert law does not hold. This means that light propagation in turbid media must be used as the source term in the heat diffusion equation, instead of the equation (4.15) [78, 79]. It has been measured some white paper and PEEK sheets and then fitted the amplitude and phase data to the equation (4.20). The results are shown in Figure 4.16 right. In this case, the retrieved α is an effective value, combining both absorption and scattering

processes inside the material. Although a more complete model should be used, the obtained D value is in good agreement with literature values (see Table 4.1).

Material	ℓ [mm]	D [mm ² /s] This work	D [mm ² /s] Literature*	α [mm ⁻¹] This work	α [mm ⁻¹] Cary	β_{IR} [mm ⁻¹]
Ni	1.03	18	22	-	∞	∞
Porous SiC	1.63	7.2	8.0	-	∞	∞
Vitreous C	1.34	6.0	6.0	-	∞	∞
AISI-304	0.94	3.4	4.0	-	∞	∞
CFR composite	0.85	0.51	0.50	-	∞	∞
ND filter	3.31	0.59	0.5-0.6	2.05	2.33	∞
ND filter	2.12	0.57	0.5-0.6	2.10	2.33	∞
ND filter	1.04	0.54	0.5-0.6	2.10	2.33	∞
Schott NG 1	0.478	0.48	0.5-0.6	10.5	11.1	∞
Schott OG 530	2.20	0.51	0.5-0.6	0.27	0.38	19.0
Schott OG 550	1.75	0.55	0.5-0.6	1.70	1.62	13.0
Schott OG 570	0.538	0.50	0.5-0.6	4.80	4.82	32.0
Schott OG 590	0.645	0.51	0.5-0.6	5.00	5.31	49.0
Schott RG 610	0.611	0.50	0.5-0.6	5.85	6.18	27.0
Schott RG 630	0.400	0.39	0.5-0.6	9.60	9.97	50.0
LaMnO ₃	0.313	1.07	1.15	∞	∞	8.50
CoO	0.204	2.4	2.2	∞	∞	4.50
PLLA composite	0.460	0.10	-	-	-	-
Paper	0.247	0.16	0.144	8.10	-	∞
Paper	0.370	0.14	0.144	6.77	-	∞
PEEK	0.688	0.18	0.19	4.32	-	19.8
Ge	3.0	-	35	-	∞	-

Table 4.1: Thermal diffusivity (D), optical absorption coefficient (α) and IR absorption coefficient (β_{IR}) of the measured materials. Uncertainty in D is 5% and α is 10%. *References [35, 42, 55, 62, 76, 77, 80, 81].

As a final remark, it is worth making some considerations about the accuracy of the retrieved D and α values. In the case of opaque materials (both to visible and IR wavelengths), the parallelism of the straight lines of $\text{Ln}(S_n)$ and $\Psi(S_n)$ provides a good test of the reliability of the obtained value of D . Moreover, the thickness of the sample should be selected in such a way that the straight lines produce changes of more than 4 rads before the noise appears. If both conditions are fulfilled, the main source of error comes from the uncertainty in ℓ (surface roughness, lack of parallelism,...). Accordingly, for opaque materials, the uncertainty in thermal diffusivity is estimated to be $\Delta D \leq 3\%$. For not completely opaque samples ($10 < \alpha \ell < 30$), only the slope of $\text{Ln}(S_n)$ can be used to retrieve the thermal diffusivity of the

sample. This means that the test of parallelism cannot be used, so that the estimation for the uncertainty in thermal diffusivity raises up to $\Delta D \leq 5\%$. In the case of semitransparent samples ($0.8 < \alpha\ell < 10$), both D and α can be obtained, but the accuracy is not the same all along that range. At low $\alpha\ell$ values ($0.8 < \alpha\ell < 2$), the contrast in both $\text{Ln}(S_n)$ and $\Psi(S_n)$ is small (see Figure 4.4), reducing the accuracy of the retrieved D and α values. On the contrary, at high $\alpha\ell$ values ($7 < \alpha\ell < 10$), the contrast is high, but the signal is small, reducing the signal to noise ratio and, therefore, the accuracy of the obtained D and α values. The most accurate results are obtained for intermediate $\alpha\ell$ values ($4 < \alpha\ell < 6$), which produce a contrast between 2 to 4 rads, while keeping a good enough signal to noise ratio. Note that, in most cases, it is possible to work within this intermediate range by selecting the sample thickness appropriately. In this intermediate range, the errors in thermal diffusivity and optical absorption coefficient are estimated to be $\Delta D \leq 5\%$ and $\Delta\alpha \leq 10\%$. The main sources of error are the uncertainty in ℓ , the effect of scattered light inside the sample, and, above all, that the model only takes into account an effective β_{IR} value and not the complete IR spectrum from 5 to 12 μm . The reason for the uncertainty of α being higher than that of D is related to the fact that α is sensitive to the whole frequency scan of $\text{Ln}(S_n)$ and $\Psi(S_n)$, while D is mainly sensitive to low frequencies, where the IR signal is higher.

4.4.2. Multilayered solids

So as to obtain simultaneously thermal diffusivity D and optical absorption coefficient α in semitransparent multilayer samples by modulated plane PTR, a simple compact method has been developed theoretically in Section 4.2.2: the thermal quadrupole method. Now, two experimental applications are presented. One of them shows the effect of paint layers on the PTR measurements and the other one presents the possibility to characterize thermal contact resistances between layers.

The first application of this matrix method attempts to quantify the effect of the usual practice of coating the sample surfaces with paint layers in order to increase the light

absorption and the IR emissivity. Equation (4.11) for a system of multiple layers with perfect thermal contact is used to represent the sample with paint layers at both sides. Figure 4.17 shows the effect of the presence of paint layers ($D_{paint} = 0.20 \text{ mm}^2/\text{s}$ and $K_{paint} = 0.40 \text{ W/mK}$) of different thicknesses in the self-normalized temperature of a Ni slab 1.03 mm thick ($D_{Ni} = 22 \text{ mm}^2/\text{s}$ and $K_{Ni} = 80 \text{ W/mK}$) using plane illumination. In absence of paint layers (black lines), $\text{Ln}(T_n)$ and $\Psi(T_n)$ are parallel straight lines from whose slope (m) the thermal diffusivity can be obtained: $m = -\ell\sqrt{\pi/D}$. The presence of two 1 μm thick paint layers (green lines), produces an increase of the slope, leading to an underestimation of the thermal diffusivity of the material if the equation above is directly applied, i.e., using $\ell = \ell_{sample} + \ell_{paint}$. For 10 μm thick paint layers (purple lines), even the parallelism of $\text{Ln}(T_n)$ and $\Psi(T_n)$ is lost. This is the reason why smaller values of the thermal diffusivity of Ni and AISI-304 stainless steel than those found in literature were obtained (see Table 4.1).

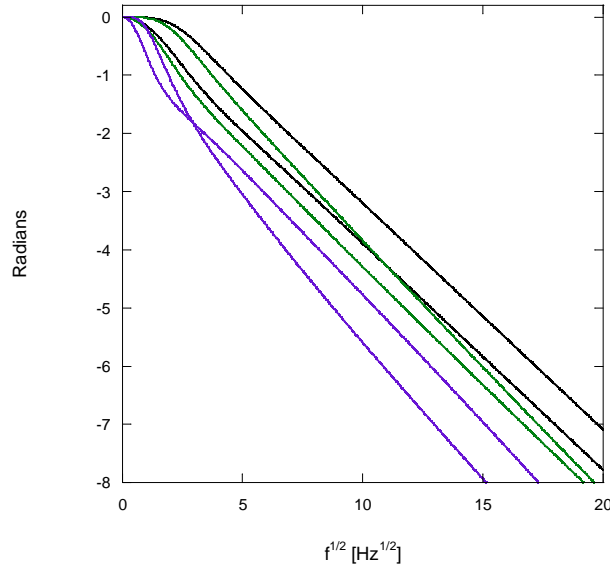


Figure 4.17: Simulations of the self-normalized temperature as a function of \sqrt{f} for a Ni slab 1.03 mm thick with paint layers in each surface using plane illumination. Black lines $\ell_{paint} = 0$, green lines $\ell_{paint} = 1 \mu\text{m}$ and purple lines $\ell_{paint} = 10 \mu\text{m}$. Upper and lower curves of each colour correspond to $\text{Ln}(T_n)$ and $\Psi(T_n)$, respectively.

In Figure 4.18 left the error in the thermal diffusivity of opaque slabs due to the presence of thin paint layers at both surfaces as a function of the diffusivity of the sample is quantified. As before, the slope $m = -\ell\sqrt{\pi/D}$ is used to calculate the thermal diffusivity, where ℓ is the sum of the thickness of the sample and the thickness of the two paint layers. Simulations have been performed for various thicknesses of the paint layers whose thermal properties are: $D_{\text{paint}} = 0.20 \text{ mm}^2/\text{s}$ and $K_{\text{paint}} = 0.40 \text{ W/mK}$. In all the simulations the ratio $\ell/\sqrt{D} = 0.5 \text{ s}^{1/2}$ is kept constant. As can be seen, the further the thermal diffusivities of paint and sample, the higher the error on the obtained thermal diffusivity of the sample. It is worth noting that even a $1 \mu\text{m}$ thick paint layer can produce a significant error on thermal diffusivity measurements. Moreover, these simulations show that using a coating of higher/lower thermal diffusivity than that of the sample introduces an overestimation/underestimation on the retrieved sample diffusivity. In particular, paint layers must be avoided for accurate modulated PTR thermal diffusivity measurements of good thermal conductors.

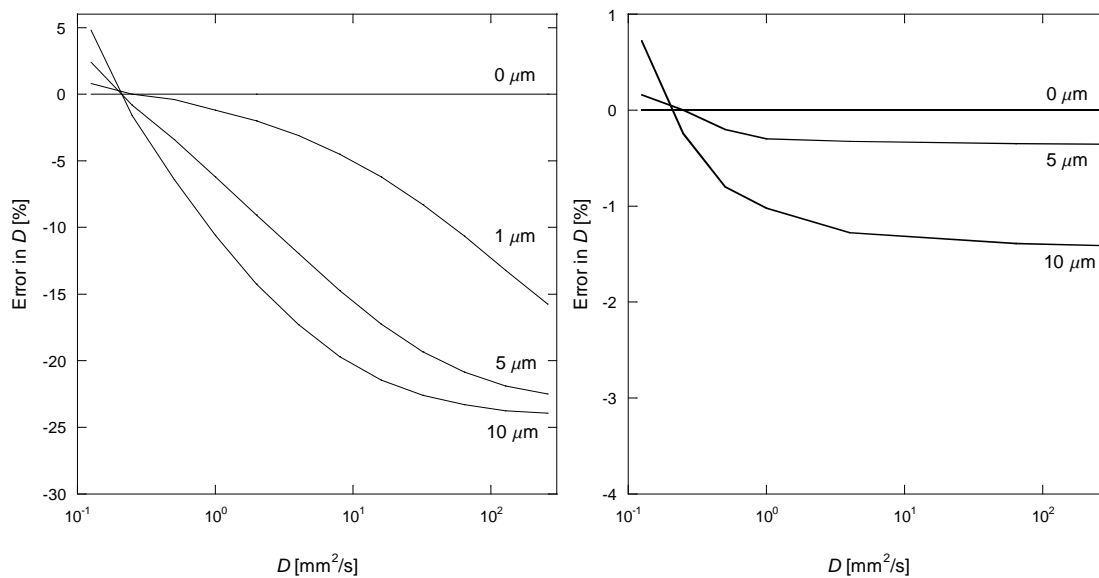


Figure 4.18: Simulations of the error in the thermal diffusivity of opaque sheets due to the presence of a thin paint layer as a function of the thermal diffusivity using modulated PTR (left) or the flash method (right). Results for paint layers of $1 \mu\text{m}$, $5 \mu\text{m}$ and $10 \mu\text{m}$ are shown.

Anyway, it is surprising that in the laser flash method, where the front surface of an opaque sheet is illuminated by a brief light pulse and the temperature at the rear surface is recorded, the influence of the paint layers is almost negligible (see Figure 4.18 right).

The second application is the characterization of the thermal contact resistance between layers. Figure 4.19 shows in symbols the self-normalized PTR signal corresponding to a two-layer sample made of two neutral density filters (Edmund Optics, optical density 1.0) of the same thickness, $\ell = 1.04$ mm, whose properties were measured and shown in Table 4.1 ($D = 0.54$ mm²/s, $\alpha = 2.10$ mm⁻¹ and $\beta_{IR} = \infty$). In order to vary the thermal contact resistance, a plastic layer with a centred hole of 2 cm of diameter was placed between the two glass sheets. Plastic films of the following thicknesses were used: 0 (no plastic film, plotted in black), 25 μ m (in blue), 50 μ m (in green) and 75 μ m (in red). The glass sheets with the plastic films were pressed using two clips.

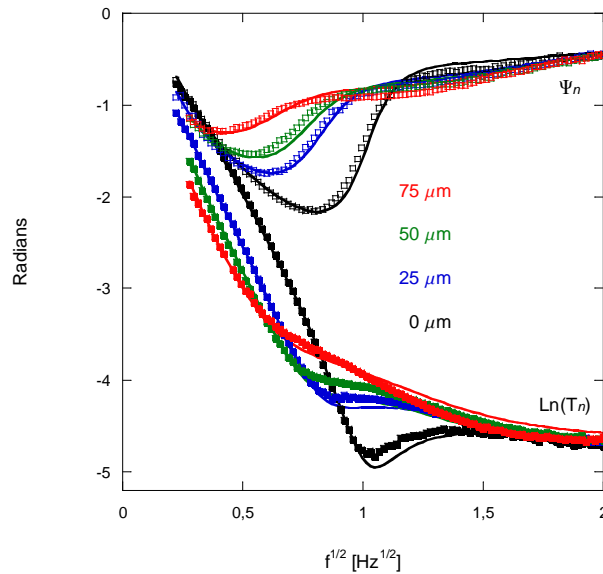


Figure 4.19: Modulated plane PTR measurements of the self-normalized temperature as a function of \sqrt{f} for a filter stack made of two equal neutral density filters ($\ell = 1.04$ mm) with a holed plastic film as a barrier. The thickness of the plastic film is varied: 0 (no plastic, black), 25 μ m (blue), 50 μ m (green) and 75 μ m (red). Continuous lines are the fittings to the equation (4.12).

Continuous lines in Figure 4.19 correspond to the simultaneous fitting of $\text{Ln}(T_n)$ and $\Psi(T_n)$ to the equation (4.12) with the thermal resistance R as the fitting parameter. As can be seen, the quality of the fitting is good and the retrieved thermal resistances are 1.05×10^{-4} , 7.6×10^{-4} , 1.6×10^{-3} and 2.3×10^{-3} $\text{m}^2\text{K}/\text{W}$. According to the expression $R = \ell/K_{air}$, where $K_{air} = 0.026$ W/mK , these thermal resistances correspond to air layers of thicknesses 2.7 μm (no plastic film), 20 μm , 41 μm and 60 μm , which are close to, but a bit below, the geometrical values. This underestimation could be attributed to a real reduction of the air layer, since the clamping could decrease the plastic film thickness.

5. Conclusions

The most important conclusions of the work developed and presented in this thesis are summarized below.

Concerning research on free standing thin films and filaments:

- A complete theoretical model including heat losses by the three mechanisms, convection, radiation and conduction, has been developed.
- Heat conduction to the gas has been identified as the mechanism responsible for the loss of linearity of the expected straight lines obtained when applying the slopes method, leading to overestimation in thermal diffusivity.
- Working in vacuum environment of at least 10^{-3} mbar has been proposed to avoid the disturbing effect of heat losses by conduction to the gas, avoiding at the same time heat losses by convection. The remaining heat losses by radiation can be cancelled by means of the product of the slopes corresponding to the amplitude and phase representations, allowing so the retrieval of the correct diffusivity value.
- Experimental measurements have been performed in a large variety of samples, isotropic and anisotropic, obtaining reliable results for materials whose diffusivities range between 0.10 and 300 mm²/s and that are as thin as 7 μm.

Regarding the thermal diffusivity and optical absorption coefficient simultaneous retrieval for semitransparent homogenous samples:

- A complete theoretical model has been studied considering the effect of multiple reflexions of the exciting light beam and the transparency of the samples to the infrared radiation.
- Self-normalization has been selected in order to suppress the dependence of the detection electronics on frequency.
- Simultaneous measurements on thermal diffusivity, D , and optical absorption coefficient, α , have been performed for samples in the range $0.8 < \alpha l < 10$, what means achieving the retrieval of transmission coefficients from 0.5 to $4 \cdot 10^{-5}$.
- Experimental results for a vast array of coloured filters of different thicknesses have been obtained, providing accurate D values and α results verified by means of optical methods.

Relating to the D and α simultaneous measurement for semitransparent multilayer samples:

- The Thermal Quadrupole Method has been extended to account for multilayer semitransparent samples, providing a compact method to calculate the surface temperatures of such samples.
- The effect of paint coating the samples has been evaluated, quantifying the error on the retrieved sample diffusivity.
- Thermal contact resistances between layers have been characterized for filter stacks.

These conclusions lay the grounds for future research. Interests now focus on inverse methods development for reconstruction of continuously varying thermal diffusivity, $D(z)$, and optical absorption coefficient, $\alpha(z)$, on multilayer semitransparent samples, such as functionally graded materials or partially cured resins.

In addition, thermal properties, diffusivity and conductivity, of thin magnetic microwires, made of a metallic core with a glass coating, of diameters ranging from 10 to 30 μm are now under study.

List of publications

Research for this thesis has resulted in the publications below:

- Arantza Mendioroz, Raquel Fuente-Dacal, Estibaliz Apiñaniz and Agustín Salazar, *Thermal diffusivity measurements of thin plates and filaments using lock-in thermography*, Review of Scientific Instruments 80, 074904 (2009)
- Agustín Salazar, Arantza Mendioroz and Raquel Fuente, *The strong influence of heat losses on the accurate measurement of thermal diffusivity using lock-in thermography*, Applied Physics Letters 95, 121905 (2009)
- Agustín Salazar, Arantza Mendioroz, Raquel Fuente and Ricardo Celorrio, *Accurate measurements of the thermal diffusivity of thin filaments by lock-in thermography*, Journal of Applied Physics 107, 043508 (2010)
- Agustín Salazar, Raquel Fuente, Estibaliz Apiñaniz, and Arantza Mendioroz, *Thermal diffusivity of nonflat plates using the flash method*, Review of Scientific Instruments 82, 014902 (2011)
- Raquel Fuente, Estibaliz Apiñaniz, Arantza Mendioroz and Agustín Salazar, *Simultaneous measurement of thermal diffusivity and optical absorption*

coefficient using photothermal radiometry. I. Homogeneous solids, Journal of Applied Physics 110, 033515 (2011)

- Agustín Salazar, Raquel Fuente, Estibaliz Apiñaniz, Arantza Mendioroz and Ricardo Celorrio, *Simultaneous measurement of thermal diffusivity and optical absorption coefficient using photothermal radiometry. II Multilayered solids*, Journal of Applied Physics 110, 033516 (2011)
- Raquel Fuente, Arantza Mendioroz, Estibaliz Apiñaniz and Agustín Salazar, *Simultaneous measurement of thermal diffusivity and optical absorption coefficient of solids using PTR and PPE: A comparison*, International Journal of Thermophysics (submitted)
- Agustín Salazar, Raquel Fuente, Arantza Mendioroz, Estibaliz Apiñaniz and Ricardo Celorrio, *Application of the Thermal Quadrupoles Method to semitransparent solids*, International Journal of Thermophysics (submitted)

In addition, the work has been presented in the following conferences:

- Agustín Salazar, Arantza Mendioroz, Raquel Fuente and Ricardo Celorrio, *Accurate measurements of the thermal diffusivity of thin films and thin filaments using lock-in thermography*, 10th Conference on quantitative infrared thermography, Quebec (Canada), 2010 (International Conference) Oral
- Raquel Fuente, Estibaliz Apiñaniz, Arantza Mendioroz and Agustín Salazar, *Simultaneous measurements of thermal diffusivity and optical absorption coefficient of homogeneous solids using photothermal radiometry*, 19th European Conference on Thermophysical Properties, Thessaloniki (Greece), 2011, (International Conference) Oral

- Raquel Fuente, Estibaliz Apiñaniz, Arantza Mendioroz, Ricardo Celorrio and Agustín Salazar, *Thermal and optical characterization of multilayered solids using photothermal radiometry*, 19th European Conference on Thermophysical Properties, Thessaloniki (Greece), 2011, (International Conference) Oral
- Agustín Salazar, Raquel Fuente, Estibaliz Apiñaniz and Arantza Mendioroz, *Thermal diffusivity of non-flat plates using the flash method*, 19th European Conference on Thermophysical Properties, Thessaloniki (Greece), 2011, (International Conference) Oral
- Raquel Fuente, Estibaliz Apiñaniz, Arantza Mendioroz and Agustín Salazar, *Simultaneous measurements of thermal diffusivity and optical absorption coefficient of homogeneous solids using photothermal radiometry*, 16th International Conference on Photoacoustic and Photothermal Phenomena, Merida (Mexico), 2011, (International Conference). Oral Invited
- Agustín Salazar, Raquel Fuente, Estibaliz Apiñaniz, Arantza Mendioroz and Ricardo Celorrio, *Thermal and optical characterization of multilayered solids using photothermal radiometry*, 16th International Conference on Photoacoustic and Photothermal Phenomena, Merida (Mexico), 2011, (International Conference). Oral
- Agustín Salazar, Raquel Fuente, Arantza Mendioroz and Estibaliz Apiñaniz, *Flash method for non-flat plates*, 16th International Conference on Photoacoustic and Photothermal Phenomena, Merida (Mexico), 2011 (International Conference) Oral
- Bert Verstraeten, Chandra Shekhar Pati Tripathi, Christ Glorieux, Raquel Fuente and Jan Fizez, *Determination of the thermal diffusivity of substrates from a spatially and temporally periodic temperature field*, 16th International

Conference on Photoacoustic and Photothermal Phenomena, Merida (Mexico), 2011 (International Conference) Poster

- Raquel Fuente, Agustín Salazar, Arantza Mendioroz, Arcady Zhukov and Valentina Zhukova, *Thermal conductivity and diffusivity measurements of glass coated magnetic microwires using lock-in thermography*, 2nd Mediterranean International Workshop on Photoacoustic and Photothermal Phenomena, Erice (Italy), 2012 (International Workshop) Poster

- Estibaliz Apiñaniz, Ricardo Celorrio, Raquel Fuente, Arantza Mendioroz, Agustín Salazar, Alberto Oleaga, *Termografia infragorria: Difusibitate termikoaren neurketa*, Materialen Zientzia eta Teknologiaren I. Kongresua, Arrasate, (Spain), 2012, Oral and Poster

Resumen

Esta tesis recoge el trabajo desarrollado de caracterización tanto térmica como óptica de materiales heterogéneos mediante Termografía Infrarroja Lock-in.

La Termografía Infrarroja Lock-in o modulada es una técnica sin contacto que permite, tras una previa excitación de la muestra de estudio, obtener las propiedades tanto térmicas como ópticas de la muestra y los defectos subsuperficiales que pudiera presentar, solamente con la imagen térmica de la temperatura superficial de la muestra.

Perteneciente a la familia de las conocidas como Técnicas Fototérmicas, su fundamento se basa en el efecto fototérmico, que consiste en que un material absorbe un haz de luz de intensidad variable, y en consecuencia, se genera una onda térmica, que se propaga tanto por el material como por sus alrededores produciendo diversos efectos. Como la propagación depende de las propiedades y estructura interna del material, la detección de los efectos producidos por la onda térmica revelará dicha información.

Esta técnica comenzó su andadura como Radiometría Fototérmica (PTR), donde un detector infrarrojo monolítico recoge la lectura de la oscilación de temperatura sobre un pequeño área de la superficie. En caso de ser necesario un mapa de la temperatura superficial de la muestra, hay que realizar un escaneo de la superficie punto por

punto, lo que se traduce en que ésta técnica requiere largos tiempos de medida, y por tanto queda relegada a los casos estrictamente necesarios. Cuando más adelante se desarrollaron las cámaras de vídeo infrarrojas de alta frecuencia y resolución espacial, la Termografía Infrarroja resurgió como herramienta para la rápida caracterización de materiales.

Desde entonces, la Termografía Infrarroja ha sido ampliamente utilizada para medir propiedades térmicas de muestras con superficies planas y paralelas, en concreto difusividad térmica. El método tradicional de medida de difusividad en este tipo de materiales es el llamado “método de las fase”, que contempla dos opciones en función del tipo de iluminación modulada que se emplee.

Por una parte, se pueden caracterizar muestras de espesor conocido mediante iluminación plana. En este caso, el campo de temperatura en la superficie no iluminada se mide en función de la frecuencia de modulación, y tanto la fase como el logaritmo neperiano de la amplitud de la temperatura oscilante se representan en función de la raíz de la frecuencia, mostrando ambas un comportamiento lineal de cuyas pendientes se puede extraer el valor de la difusividad perpendicular de la muestra.

Por otra parte, también se puede utilizar iluminación focalizada, donde lo que se recoge es un mapa de la temperatura superficial de la muestra a una frecuencia de modulación fija. Esta vez, las representaciones de amplitud y fase en función de la distancia al punto de excitación también son lineales y permiten extraer de sus pendientes el valor de la difusividad térmica paralela del material.

El reciente interés por la caracterización de propiedades térmicas de muestras de aplicación industrial ha conducido al estudio de muestras con geometrías más complejas, como varillas, cilindros, esferas, filamentos o láminas delgadas.

En los dos últimos casos, se ha observado una sobreestimación de los valores de difusividad obtenidos al aplicar el método de las pendientes en muestras delgadas y de baja difusividad. En consecuencia, esta tesis se fija como primer objetivo el

esclarecimiento de las causas de la sobreestimación, y el desarrollo de un modelo teórico y un sistema experimental que permita la medida correcta de la difusividad en este tipo de muestras.

Así pues, la investigación en este aspecto ha resultado en el desarrollo de un modelo teórico que incluye pérdidas de calor por los tres mecanismos: radiación, convección y conducción al gas. La contribución de las pérdidas de calor por conducción al gas, tradicionalmente despreciada por la baja conductividad del aire, ha sido identificada como el mecanismo responsable de la pérdida de linealidad de las esperadas rectas representaciones de la amplitud y fase de la temperatura superficial, conduciendo a una sobreestimación en el valor obtenido de la difusividad al aplicar el método de las pendientes.

Para solventar el problema, se ha propuesto realizar las medidas experimentales en un ambiente de vacío de al menos 10^{-3} mbar, necesario para evitar el efecto de las pérdidas por conducción al gas y poder aplicar el método de las pendientes. Junto con la conducción al gas, el vacío también elimina la convección, pero no así la radiación, que persiste. Sin embargo, el método de las pendientes es capaz de cancelar el efecto de las pérdidas por radiación mediante el producto de las pendientes de las representaciones de amplitud y fase, dando lugar, por tanto, a la obtención de valores correctos de difusividad.

Experimentalmente, se han realizado medidas en un amplio espectro de muestras de filamentos y láminas, tanto isótropas como anisótropas, permitiendo caracterizar materiales con difusividades entre 0.10 y 300 mm²/s de muestras tan delgadas como 7 μm.

Además de esto, algunas técnicas fototérmicas han probado su valía para medir correctamente el coeficiente de absorción óptica de gases, líquidos y sólidos, rivalizando con técnicas ópticas en los casos extremos de materiales poco o muy absorbentes. El segundo objetivo de esta tesis consiste, entonces, en realizar un estudio sistemático de la técnica PTR modulada plana para obtener simultáneamente y correctamente ambas, difusividad en profundidad y coeficiente de absorción

óptica, de muestras semitransparentes homogéneas, desde un punto de vista tanto teórico como experimental, estableciendo las condiciones y límites para la aplicación de la técnica.

Así, se ha estudiado un modelo teórico completo, considerando el efecto de las múltiples reflexiones del haz excitador y la transparencia de las muestras a la radiación infrarroja. Se ha seleccionado el método de autonormalización para suprimir la dependencia del sistema electrónico con la frecuencia, y se han realizado medidas simultáneas de difusividad (D) y coeficiente de absorción óptica (α) para muestras en el rango $0.8 < \alpha \ell < 10$, que corresponde a determinar coeficientes de transmisión óptica de 0.5 a $4 \cdot 10^{-5}$. Además, se ha medido un amplio número de filtros coloreados de diferentes espesores, obteniendo resultados precisos de difusividades y coeficientes de absorción óptica comprobados mediante métodos ópticos.

Por último, se han considerado muestras multicapa. Tras los trabajos iniciales de Mandelis y colaboradores, la técnica PRT modulada ha sido empleada para la reconstrucción del perfil de conductividad en profundidad de muestras heterogéneas como aceros endurecidos, materiales funcionalmente graduados y resinas dentales. Además, se han publicado en los últimos años dos trabajos de investigación relativos a la aplicación del PTR modulado a la reconstrucción simultánea de coeficiente de absorción y difusividad variables en profundidad en muestras heterogéneas semitransparentes.

En esta tesis, se estudia la posibilidad de obtener con PTR modulado ambas α y D simultáneamente en materiales multicapa semitransparentes mediante el Método de los Cuadrupolos Térmicos. Este método había sido aplicado en el marco de la conducción al cálculo de la temperatura superficial de materiales opacos multicapa y al cálculo de la combinación de radiación y conducción en materiales gruesos semitransparentes.

Así pues, aquí el Método de los Cuadrupolos Térmicos se ha extendido a las muestras semitransparentes multicapa, proporcionando un método compacto para el

cálculo de la temperatura superficial. Además, se ha evaluado el efecto de las capas de pintura depositadas en ocasiones sobre ciertas muestras para aumentar tanto su absorción como emisión infrarroja, cuantificando el error cometido al determinar la difusividad del material. Asimismo, se han caracterizado las resistencias térmicas entre capas para apilamientos de filtros.

La investigación realizada a lo largo de esta tesis continúa ahora con el desarrollo de métodos inversos de reconstrucción de perfiles de variación continua en profundidad de $D(z)$ y $\alpha(z)$ en materiales multicapa semitransparentes, como los materiales funcionalmente graduados o las resinas dentales.

Igualmente, se encuentran ahora en estudio las propiedades térmicas, difusividad y conductividad, de microhilos magnéticos compuestos por un núcleo metálico y un recubrimiento de vidrio, resultando diámetros de entre 10 y 30 μm .

References

- [1] X. P. V. Maldague, *Nondestructive Evaluation of Materials by Infrared Thermography*. London: Springer-Verlag, 1993.
- [2] X. P. V. Maldague. *Theory and Practice of Infrared Technology for Nondestructive Testing* 2001.
- [3] C. Wang, A. Mandelis and Y. Liu. Photothermal radiometry with solid cylindrical samples. *J. Appl. Phys.* 96(7), pp. 3756-3762. 2004.
- [4] C. Wang, A. Mandelis and Y. Liu. Thermal-wave nondestructive evaluation of cylindrical composite structures using frequency-domain photothermal radiometry. *J. Appl. Phys.* 97(1), pp. 014911. 2005.
- [5] A. Salazar and R. Celorrio. Application of the thermal quadrupole method to the propagation of thermal waves in multilayered cylinders. *J. Appl. Phys.* 100(11), pp. 113535. 2006.
- [6] A. Salazar, F. Garrido and R. Celorrio. Thermal diffusivity of rods, tubes, and spheres by the flash method. *J. Appl. Phys.* 99(6), pp. 066116. 2006.
- [7] C. Wang, Y. Liu, A. Mandelis and J. Shen. Frequency domain photothermal radiometry with spherical solids. *J. Appl. Phys.* 101(8), pp. 083503. 2007.

-
- [8] N. Madariaga and A. Salazar. Propagation of thermal waves in multilayered spheres. *J. Appl. Phys.* 101(10), pp. 103534. 2007.
- [9] C. Pradere, J. Goyheneche, J. Batsale, S. Dilhaire and R. Pailler. Thermal diffusivity measurements on a single fiber with microscale diameter at very high temperature. *Int. J. Therm. Sci.* 45(5), pp. 443-451. 2006.
- [10] M. Oksanen, R. Scholz and L. Fabbri. On the longitudinal thermal diffusivity of SiC-based fibres. *J. Mater. Sci. Lett.* 16(13), pp. 1092-1094. 1997.
- [11] B. Zhang and R. Imhof. Theoretical analysis of the surface thermal wave technique for measuring the thermal diffusivity of thin slabs. *Appl. Phys. A-Mater. Sci. Process.* 62(4), pp. 323-334. 1996.
- [12] A. Wolf, P. Pohl and R. Brendel. Thermophysical analysis of thin films by lock-in thermography. *J. Appl. Phys.* 96(11), pp. 6306-6312. 2004.
- [13] A. Muscio, P. Bison, S. Marinetti and E. Grinzato. Thermal diffusivity measurement in slabs using harmonic and one-dimensional propagation of thermal waves. *International Journal of Thermal Sciences* 43(5), pp. 453-463. 2004.
- [14] G. Wetsel and F. McDonald. Photoacoustic determination of absolute optical-absorption coefficient. *Appl. Phys. Lett.* 30(5), pp. 252-254. 1977.
- [15] Y. Teng and B. Royce. Absolute optical-absorption coefficient measurements using photoacoustic-spectroscopy amplitude and phase information. *J. Opt. Soc. Am.* 70(5), pp. 557-560. 1980.
- [16] A. Mandelis. Absolute optical-absorption coefficient measurements using transverse photothermal deflection spectroscopy. *J. Appl. Phys.* 54(6), pp. 3404-3409. 1983.
- [17] M. Munidasa, M. Tianchi, A. Mandelis, S. Brown and L. Mannik. Nondestructive depth profiling of laser-processed zr-2.5nb alloy by ir photothermal radiometry. *Mater. Sci. Eng. A-Struct. Mater. Prop. Microstruct. Process.* 159(1), pp. 111-118. 1992.

-
- [18] T. Lan, U. Seidel, H. Walther, G. Goch and B. Schmitz. Experimental results of photothermal microstructural depth profiling. *J. Appl. Phys.* 78(6), pp. 4108-4111. 1995.
- [19] L. Nicolaidis, A. Mandelis and C. Beingessner. Physical mechanisms of thermal-diffusivity depth-profile generation in a hardened low-alloy mn, si, cr, mo steel reconstructed by photothermal radiometry. *J. Appl. Phys.* 89(12), pp. 7879-7884. 2001.
- [20] H. Walther, D. Fournier, J. Krapez, M. Luukkala, B. Schmitz, C. Sibilis, H. Stamm and J. Thoen. Photothermal steel hardness measurements - results and perspectives. *Anal. Sci.* 17pp. S165-S168. 2001.
- [21] S. Paoloni, P. Mayr, C. Glorieux, R. Li Voti, H. Bentefour and J. Thoen. Photothermal depth profiling in the presence of lateral heat flow effects. *Anal. Sci.* 17pp. S406-S409. 2001.
- [22] C. Wang and A. Mandelis. Characterization of hardened cylindrical C1018 steel rods (0.14%-0.2% C, 0.6%-0.9% mn) using photothermal radiometry. *Rev. Sci. Instrum.* 78(5), pp. 054902. 2007.
- [23] C. Wang, A. Mandelis, H. Qu and Z. Chen. Influence of laser beam size on measurement sensitivity of thermophysical property gradients in layered structures using thermal-wave techniques. *J. Appl. Phys.* 103(4), pp. 043510. 2008.
- [24] H. Qu, C. Wang, X. Guo and A. Mandelis. Reconstruction of depth profiles of thermal conductivity of case hardened steels using a three-dimensional photothermal technique. *J. Appl. Phys.* 104(11), pp. 113518. 2008.
- [25] Y. Nagasaka, T. Sato and T. Ushiku. Non-destructive evaluation of thermal diffusivity distributions of functionally graded materials by photothermal radiometry. *Meas Sci Technol* 12(12), pp. 2081-2088. 2001.
- [26] P. Martinez-Torres, A. Mandelis and J. J. Alvarado-Gil. Photothermal determination of thermal diffusivity and polymerization depth profiles of polymerized dental resins. *J. Appl. Phys.* 106(11), pp. 114906. 2009.
-

-
- [27] J. Ravi, Y. Lu, S. Longuemart, S. Paoloni, H. Pfeiffer, J. Thoen and C. Glorieux. Optothermal depth profiling by neural network infrared radiometry signal recognition. *J. Appl. Phys.* 97(1), pp. 014701. 2005.
- [28] P. Martinez-Torres, A. Mandelis and J. J. Alvarado-Gil. Optical and thermal depth profile reconstructions of inhomogeneous photopolymerization in dental resins using photothermal waves. *J. Appl. Phys.* 108(5), pp. 054902. 2010.
- [29] D. Maillet, S. Andre, J. C. Batsale, A. Degiovanni and C. Moyne, *Thermal Quadrupoles*. New York: Wiley, 2000.
- [30] S. Andre, B. Remy, D. Maillet, A. Degiovanni and J. Serra. Modulated photothermal radiometry applied to semitransparent samples: Models and experiments. *J. Appl. Phys.* 96(5), pp. 2566-2575. 2004.
- [31] H. S. Carslaw and J. C. (. Jaeger. *Conduction of Heat in Solids* (2 ed.) 1959.
- [32] R. N. Bracewell, *The Fourier Transform and its Applications*. Singapore: McGraw-Hill, 1986.
- [33] M. Abramowitz and I. A. Stegun, *Handbook of Mathematical Functions*. New York: Dover, 1965.
- [34] L. Fabbri and P. Fenici. 3-dimensional photothermal radiometry for the determination of the thermal-diffusivity of solids. *Rev. Sci. Instrum.* 66(6), pp. 3593-3600. 1995.
- [35] Y. A. Cengel, *Heat Transfer: A Practical Approach*. Boston: McGraw-Hill, 2003.
- [36] S. Kanstad and P. Nordal. Experimental aspects of photothermal radiometry. *Can. J. Phys.* 64(9), pp. 1155-1164. 1986.
- [37] J. Bisson and D. Fournier. Influence of diffraction on low thermal diffusivity measurements with infrared photothermal microscopy. *J. Appl. Phys.* 83(2), pp. 1036-1042. 1998.

-
- [38] J. Bisson and D. Fournier. The coupled influence of sample heating and diffraction on thermal diffusivity estimate with infrared photothermal microscopy. *J. Appl. Phys.* 84(1), pp. 38-43. 1998.
- [39] H. Walther and T. Kitzing. Systematic errors of locally resolved photothermal radiometric measurements. *J. Appl. Phys.* 84(3), pp. 1163-1167. 1998.
- [40] S. Paoloni and D. Fournier. Spectral dependence of signal distortions in spatially resolved photothermal radiometry. *J. Appl. Phys.* 92(10), pp. 5950-5954. 2002.
- [41] S. Paoloni and D. Fournier. Semi-empirical approach for the analysis of infrared photothermal microscopy. *J. Appl. Phys.* 92(10), pp. 5955-5958. 2002.
- [42] Goodfellow Corporation, .
- [43] J. Hou, X. Wang and J. Guo. Thermal characterization of micro/nanoscale conductive and non-conductive wires based on optical heating and electrical thermal sensing. *J. Phys. D-Appl. Phys.* 39(15), pp. 3362-3370. 2006.
- [44] X. Quelin, B. Perrin, G. Louis and P. Peretti. 3-dimensional thermal-conductivity-tensor measurement of a polymer crystal by photothermal probe-beam deflection. *Phys. Rev. B* 48(6), pp. 3677-3682. 1993.
- [45] A. Salazar, A. SanchezLavega, A. Ocariz, J. Guitonny, G. Pandey, D. Fournier and A. Boccara. Thermal diffusivity of anisotropic materials by photothermal methods. *J. Appl. Phys.* 79(8), pp. 3984-3993. 1996.
- [46] J. Barkyoub and D. Land. Thermal-diffusivity measurement of thin wires using photothermal deflection. *J. Appl. Phys.* 78(2), pp. 905-912. 1995.
- [47] J. E. Parrot and A. D. Stukes, *Thermal Conductivity in Solids*. London: Pion, 1975.
- [48] O. Breitenstein and M. Langenkamp, *Lock-in Thermography*. Berlin: Springer, 2003.

-
- [49] O. Breitenstein, W. Warta and M. Langenkamp. *Lock-in Thermography: Basics and use for Evaluating Electronic Devices and Materials* (2nd ed.) 201010.
- [50] K. M. Welch, *Capture Pumping Technology*. Amsterdam: North-Holland, 2001.
- [51] C. Choy, G. Yang and Y. Wong. Thermal diffusivity of polymer films by pulsed photothermal radiometry. *J. Polym. Sci. Pt. B-Polym. Phys.* 35(10), pp. 1621-1631. 1997.
- [52] C. Choy, Y. Wong, G. Yang and T. Kanamoto. Elastic modulus and thermal conductivity of ultradrawn polyethylene. *J. Polym. Sci. Pt. B-Polym. Phys.* 37(23), pp. 3359-3367. 1999.
- [53] H. Kato, T. Baba and M. Okaji. Anisotropic thermal-diffusivity measurements by a new laser-spot-heating technique RID F-1506-2011. *Meas Sci Technol* 12(12), pp. 2074-2080. 2001.
- [54] A. Salazar, A. Sanchez-Lavega, A. Ocariz, J. Guitonny, J. Pandey, D. Fournier and A. Boccara. Novel results on thermal-diffusivity measurements on anisotropic materials using photothermal methods. *Appl. Phys. Lett.* 67(5), pp. 626-628. 1995.
- [55] L. R. Touloukian, R. W. Powell, C. Y. Ho and M. C. Nicolasu, *Thermal Diffusivity*. New York: IFI/Plenum, 1973.
- [56] S. Nagase, M. Ohshika, S. Ueda, N. Satoh and K. Tsujii. A universal structural model for human hair to understand the physical properties 1 RID B-8153-2009. *Bull. Chem. Soc. Jpn.* 73(9), pp. 2161-2167. 2000.
- [57] A. Salazar and A. Sanchez-Lavega. Measurements of the thermal diffusivity tensor of polymer-carbon fiber composites by photothermal methods. *Int. J. Thermophys.* 19(2), pp. 625-636. 1998.
- [58] P. Nordal and S. Kanstad. Photothermal radiometry. *Phys. Scripta* 20(5-6), pp. 659-662. 1979.
- [59] R. Santos and L. Miranda. Theory of the photothermal radiometry with solids. *J. Appl. Phys.* 52(6), pp. 4194-4198. 1981.

- [60] R. Tom, E. Ohara and D. Benin. A generalized-model of photothermal radiometry. *J. Appl. Phys.* 53(8), pp. 5392-5400. 1982.
- [61] M. Broussely, A. Levick and G. Edwards. A novel comparative photothermal method for measuring thermal diffusivity. *Int. J. Thermophys.* 26(1), pp. 221-232. 2005.
- [62] M. Depriester, P. Hus, S. Delenclos and A. Sahraoui. New methodology for thermal parameter measurements in solids using photothermal radiometry. *Rev. Sci. Instrum.* 76(7), pp. 074902. 2005.
- [63] S. Trujillo, P. Martinez-Torres, P. Quintana and J. Jose Alvarado-Gil. Photothermal radiometry and diffuse reflectance analysis of thermally treated bones. *Int. J. Thermophys.* 31(4-5), pp. 805-815. 2010.
- [64] A. Rosencwaig and A. Gersho. Theory of photoacoustic effect with solids. *J. Appl. Phys.* 47(1), pp. 64-69. 1976.
- [65] J. Balderas-Lopez and A. Mandelis. Self-normalized photothermal technique for accurate thermal diffusivity measurements in thin metal layers. *Rev. Sci. Instrum.* 74(12), pp. 5219-5225. 2003.
- [66] M. Munidasa, F. Funak and A. Mandelis. Application of a generalized methodology for quantitative thermal diffusivity depth profile reconstruction in manufactured inhomogeneous steel-based materials. *J. Appl. Phys.* 83(7), pp. 3495-3498. 1998.
- [67] M. Chirtoc, *Thermal Wave Physics and Related Photothermal Techniques: Basic Principles and Recent Developments*. Trivandrum: Transworld Research Network, 2009.
- [68] A. Salazar, A. Mendioroz and R. Fuente. The strong influence of heat losses on the accurate measurement of thermal diffusivity using lock-in thermography. *Appl. Phys. Lett.* 95(12), pp. 121905. 2009.

-
- [69] G. Rousset, F. Charbonnier and F. Lepoutre. Influence of radiative and convective transfers in a photothermal experiment. *J. Appl. Phys.* 56(7), pp. 2093-2096. 1984.
- [70] B. Majaron and M. Milanic. Effective infrared absorption coefficient for photothermal radiometric measurements in biological tissues RID A-1025-2008. *Phys. Med. Biol.* 53(1), pp. 255-268. 2008.
- [71] H. Walther, U. Seidel, W. Karpen and G. Busse. Application of modulated photothermal radiometry to infrared transparent samples. *Rev. Sci. Instrum.* 63(11), pp. 5479-5480. 1992.
- [72] A. Salazar, E. Apinaniz, A. Mendioroz and A. Oleaga. A thermal paradox: Which gets warmer? *Eur. J. Phys.* 31(5), pp. 1053-1059. 2010.
- [73] S. Paoloni and H. Walther. Photothermal radiometry of infrared translucent materials. *J. Appl. Phys.* 82(1), pp. 101-106. 1997.
- [74] S. Krueger, R. Kordecki, J. Pelzl and B. Bein. Stray-light correction in photoacoustic measurements of solid samples. *J. Appl. Phys.* 62(1), pp. 55-61. 1987.
- [75] J. Bolte, J. H. Gu and B. K. Bein, "Background fluctuation limit of infrared detection of thermal waves at high temperatures," *High Temperatures High Pressures*, vol. 29, pp. 567, 1997.
- [76] A. Salazar, A. Oleaga and D. Prabhakaran. Thermal diffusivity of $\text{La}_{1-x}\text{Sr}_x\text{MnO}_3$ ($x < 0.3$). *Int. J. Thermophys.* 25(4), pp. 1269-1279. 2004.
- [77] M. Massot, A. Oleaga, A. Salazar, D. Prabhakaran, M. Martin, P. Berthet and G. Dhalenne. Critical behavior of CoO and NiO from specific heat, thermal conductivity, and thermal diffusivity measurements. *Phys. Rev. B* 77(13), pp. 134438. 2008.
- [78] S. Pahl, I. Vitkin, U. Breuggemann, B. Wilson and R. Anderson. Determination of optical-properties of turbid media using pulsed photothermal radiometry. *Phys. Med. Biol.* 37(6), pp. 1203-1217. 1992.

- [79] A. Matvienko, A. Mandelis, R. J. Jeon and S. H. Abrams. Theoretical analysis of coupled diffuse-photon-density and thermal-wave field depth profiles photothermally generated in layered turbid dental structures. *J. Appl. Phys.* 105(10), pp. 102022. 2009.
- [80] D. P. Almond and P. M. Patel, *Photothermal Science and Techniques*. London: Chapman and Hall, 1996.
- [81] A. SanchezLavega, A. Salazar, A. Ocariz, L. Pottier, E. Gomez, L. Villar and E. Macho. Thermal diffusivity measurements in porous ceramics by photothermal methods. *Appl. Phys. A-Mater. Sci. Process.* 65(1), pp. 15-22. 1997.

